EXPERIMENTAL IDENTIFICATION OF STRUCTURAL FORCE

COEFFICIENTS IN A BUMP-TYPE FOIL BEARING

A Thesis

by

ANTHONY WAYNE BREEDLOVE

Submitted to the Office of Graduate Studies of
Texas A&M University
in partial fulfillment of the requirements for the degree of

MASTER OF SCIENCE

August 2007

Major Subject: Mechanical Engineering

EXPERIMENTAL IDENTIFICATION OF STRUCTURAL FORCE

COEFFICIENTS IN A BUMP-TYPE FOIL BEARING

A Thesis

by

ANTHONY WAYNE BREEDLOVE

Submitted to the Office of Graduate Studies of
Texas A&M University
in partial fulfillment of the requirements for the degree of

MASTER OF SCIENCE

Approved by:

Chair of Committee, Luis San Andrés
Committee Members, John Vance
                   César Malavé
Head of Department, Dennis L. O'Neal

August 2007

Major Subject: Mechanical Engineering

ABSTRACT

Experimental Identification of Structural Force Coefficients in a Bump-Type Foil
Bearing. (August 2007)

Anthony Wayne Breedlove, B.A., University of Saint Thomas;

B.S., Texas A&M University

Chair of Advisory Committee: Dr. Luis San Andrés

This thesis presents further experimentation and modeling for bump-type gas foil bearings used in oil-free turbomachinery. The effect of shaft temperature on the measured structural force response of foil bearings is of importance for reliable high temperature applications. During actual operation with shaft rotation, the bearing structural parameters are coupled to the effects of a hydrodynamic gas film layer, thus determining the overall bearing load performance.

A 38.17 mm inner diameter foil bearing, Generation II, is mounted on an affixed non-rotating hollow shaft with an outer diameter of 38.125 mm. A cartridge heater inserted into the shaft provides a controllable heat source. The clearance between the shaft and the foil bearing increases with increasing shaft temperatures (up to 188°C). A static load (ranging from 0 N to 133 N) is applied to the bearing housing, while measuring the resulting bearing displacement, which represents the compliant structure deflection. Static load versus displacement tests render the bearing static structural stiffness. As the shaft temperature increases, the static test results indicate that the bearing structural stiffness decreases by as much as 70% depending on the bearing orientation. A dynamic load test setup includes a rigid shaft support structure and a suspended electromagnetic shaker. Dynamic load (from 13 N to 31 N) test results show that the test foil bearing stiffness increases by as much as 50% with amplitude of dynamic load above a lightly loaded region, nearly doubles with frequency up to 200 Hz, and decreases by a third as shaft temperature increases. A stick slip phenomenon

increases the bearing stiffness at higher frequencies for all the amplitudes of dynamic load tested. The test derived equivalent viscous damping is inversely proportional to amplitude of dynamic load, excitation frequency, and shaft temperature. Further, the estimated bearing dry friction coefficient decreases from 0.52 to 0.36 with amplitude of dynamic load and stays nearly constant as shaft temperature increases.

Test results identify static and dynamic bearing parameters for increasing shaft temperature. These experimental results provide a benchmark for predictions from analytical models in current development and are essential to establish sound design practices of the compliant bearing structure.

DEDICATION

To my mom and dad,

      for the love, guidance, and support I have needed to make it through life; I could

      not even begin to write a book about everything I have learned from you

To my grandparents,

      who could not see this day

To my brother,

      for the bravery and courage he has shown to face this world on his own

To my close friends,

      for making me realize that real life does not begin only after school ends

ACKNOWLEDGEMENTS

I thank my committee chair, Dr. Luis San Andrés, for providing the opportunity to research at the Texas A&M Turbomachinery Laboratory with the Tribology Group. His continued technical advice, mentorship, and financial support are gratefully appreciated.

I thank all my colleagues and friends at the Turbomachinery Lab, especially Adolfo Delgado, Dario Rubio, Tae Ho Kim, Ahmed Gamal, Arun Suryanarayanan, and Sang Hyun Park. I also thank Mr. Eddie Denk and his undergraduate technicians for their time and efforts.

Through my years at Texas A&M University, I have obtained many relationships that have helped me achieve my goals. I would like to recognize the Engineering Academic Programs Office staff, especially Jeanne Rierson, Marilyn Green, and Teresa Wright. I would also like to recognize the Mechanical Engineering Department faculty and staff, especially Kim Moses and Dr. N. K. Anand. I thank my other committee members, Dr. John Vance, Dr. Illya Hicks, and Dr. César Malavé. I also thank Dr. Dave Louis, Dr. Shannon Henderson, and Dr. Damali Moore for the models that they have established for other young students to follow.

I thank Dr. Dellacorte of NASA for his input and guidance through various means of correspondence. His leadership and drive in the field of oil-free turbomachinery technology fuels the motivation behind research and advancement.

I give special thanks to my sponsors: the United States Air Force (US-AF), the Turbomachinery Research Consortium (TRC), the National Science Foundation (NSF) under Grant No. 0322925, the National Consortium for Graduate Degrees for Minorities in Engineering and Science, Inc. (GEM) and my GEM company sponsor Schlumberger, and the Turbomachinery Laboratory at Texas A&M University.

NOMENCLATURE

A Curve fit coefficients, Equations (14) through (17)

C_{act} Actual foil bearing radial clearance [mm]

C_g Calculated foil bearing radial clearance [mm]

C_{nom} Nominal radial clearance between bearing and shaft from manufacturer [mm]

D Foil bearing inner diameter (to the top foil) [mm]

D_O Foil bearing outer diameter [mm]

D_S Test shaft outer diameter [mm]

E Young Modulus of elasticity [GPa]

F Force [N]

$F_{X,Y}$ Predicted sums of reaction forces in the X and Y directions [N]

F_δ Overall predicted foil bearing reaction force along direction of applied load [N]

$F_{\zeta i}$ Predicted reaction force of each bump in the prediction model [N]

H_i Actual bump height as a result of the bump deflection [mm]

h Bump height, measured to mid-span [mm]

I, J Parameters used in stiffness prediction Equations (18) and (19)

K Foil bearing stiffness [MN/m]

K_B Prediction model stiffness of an unspecified bump [MN/m]

K_F Prediction model stiffness of bump with two free ends [MN/m]

K_W Prediction model stiffness of bump with one welded and one free end [MN/m]

k_B Thermal conductivity of FB housing material [W/mK]

k_f Thermal conductivity of foil layer [W/mK]

k_S Thermal conductivity of test shaft material [W/mK]

L Bearing axial length [mm]

L_b Axial length of a single bump [mm]

L_h Length of cartridge heater [mm]

l_o Bump half-length [mm]

M_B Foil bearing mass [kg]

N_B Number of bumps around the inner circumference of the foil bearing

Q Foil layer height [mm]

q_r Cartridge heater radial power [W]

q_r'' Cartridge heater radial flux [W/m^2]

R Foil bearing housing outer radius [mm]

R_B Foil bearing housing inner radius [mm]

R_I Foil bearing inner radius [mm]

R_S Shaft outer radius [mm]

$R_{S,i}$ Test shaft inner radius [mm]

r_1 Inner radius in the general heat transfer Equations (7) and (8) [mm]

r_2 Outer radius in the general heat transfer Equations (7) and (8) [mm]

r_h Cartridge heater outer radius [mm]

s Bump pitch [mm]

t Bump and top foil thickness [mm]

$T_{B,i}$ Temperature at FB housing inner radius [°C]

$T_{B,o}$ Temperature at FB housing outer radius [°C]

$T_{S,i}$ Temperature at test shaft inner radius [°C]

$T_{S,o}$ Temperature at test shaft outer radius [°C]

T_1 Temperature at inner surface in general heat transfer Equations (7) and (8) [°C]

T_2 Temperature at outer surface in general heat transfer Equations (7) and (8) [°C]

W_B Foil bearing housing wall thickness [mm]

X,Y Foil bearing deflection coordinates for for prediction model [mm]

x Foil bearing experimental deflection [μm]

x_a Negative (pull) foil bearing deflection [μm]

x_{adj} Adjusted foil bearing deflection used for prediction model [μm], $x_{adj} = x-x_o$

x_b Positive (push) foil bearing deflection [μm]

x_o Foil bearing deflection offset used for prediction model [μm]

α Bump arc length [radians]

α_B Foil bearing housing Coefficient of Thermal Expansion (CTE) [μm/(m°C)]

α_f Bump and top foil CTE [μm/(m°C)]

α_S Test shaft CTE [μm/(m°C)]

β Stiffness prediction model load direction [degrees]

Δ Variation of temperature [°C]

δ Foil bearing deflection in stiffness prediction model [mm]

δC Radial clearance differential, C_{nom} - C_{act} [mm]

δ_{max} Maximum FB deflections in prediction model (push direction) [mm]

δ_{min} Minimum FB deflections in prediction model (pull direction) [mm]

ζ_i, η_i Normal and transverse deflections of single bump in prediction model [mm]

θ Foil bearing load orientation [degrees]

μ_f Dry friction coefficient

v Poisson's ratio

φ Bump foil weld location [degrees]

Subscript

B Bearing

b Bump

I Initial condition

f Foil

S Shaft

Superscript

$'$ Denotes new radial dimension after thermal expansion

Acronyms

ACM   Air Cycle Machine

APU   Auxiliary Power Units

CTE   Coefficient of Thermal Expansion

ECS   Eddy Current Sensor

FEA   Finite Element Analysis

GFB   Gas Foil Bearing

TABLE OF CONTENTS

LIST OF FIGURES

LIST OF TABLES

I INTRODUCTION

Gas foil bearings (GFBs) provide rotordynamic support for many oil-free high speed micro-turbomachinery applications. Generally, the FB structural support is made up of one or more compliant surfaces of corrugated metal and a top foil surface. The GFB, see Figure 1, under investigation is a Generation II bump-type FB.
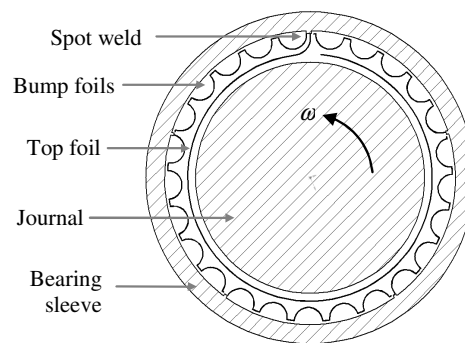
Figure 1 Schematic representation of a bump-type gas foil bearing.

The rotor is supported on the bearing elastic foil foundation, which complies easily with rotor misalignment and excursions. These bearings are hydrodynamic in nature due to the air film wedge developed between the rotor and bearing support during high speed rotation. As the air film becomes fully developed, the rotor "lifts off" from its elastic support. Important to the dynamic performance of the rotor-bearing system is the prediction of FB structural stiffness and damping force coefficients. The FB elastic foundation, a single top foil supported by a series of corrugated bump strip layers, provides non-linear structural stiffness as a function of applied load. Also, a Coulomb-type (dry friction) mechanism results from relative motions between the top foil and bumps and bumps and bearing housing, and which can be modeled as an equivalent viscous damping coefficient.

This thesis follows the style of ASME Journal of Tribology.

Recent technological developments in GFB load capacity, high temperature solid lubricant coatings, and rotordynamic and mechanical modeling and analysis enable the opportunity to overcome limitations of oil-lubricated bearings and yield improvements in weight, efficiency, performance in life cycle cost for military applications [1]. GFB performance start-stop trials of more than 100,000 cycles at 1200°F produce a maintenance-free bearing system for the life of the engine in certain applications. GFB designers and researchers seek to replace conventional oil-lubricated systems with oil-free technology. This process has proven successful during the implementation of oil-free technology into a turbocharger for a heavy-duty truck diesel engine [1]. Other proposed applications in the near future include usages in fuel cell compressors, single-use turbojet engines for missiles, reusable target drones and unmanned vehicles. The weight savings from removing oil-lubricant systems improves vehicle performance. New design freedoms such as reduced weight and maintenance costs by eliminating the oil-lubrication system, faster rotor speeds and hotter operation temperatures make GFBs attractive for a number of military vehicle systems.

The main objective of this work is to identify the structural stiffness, equivalent viscous damping and/or dry friction coefficients of a FB while varying the excitation frequency and amplitude of dynamic load, and for increasing shaft temperatures. The identification of the bearing structural characteristics provides the basis of GFB performance during operation with rotor spinning.

II LITERATURE REVIEW

A chronological and critical review of archival papers in gas foil bearings published within the past 15 years follows. The methods of analysis, the landmark findings, and the effects of these findings on the gas foil bearing industry are presented. The current work involves parameter identification for gas foil bearings (GFBs) using a stationary journal and an electromagnetic shaker. The shaker excites the foil bearing at a single frequency and fixed load amplitude at two different angular orientations of the bearing. Testing using a high-temperature (maximum 200ºC) test rig aims to determine effects of temperature on the FB dynamic structural stiffness and equivalent viscous damping.

The first section reviews the papers that consider industrial applications and advantages involved in GFB performance as it pertains to temperature tolerance, load capacity and journal operation. The following section details the search for a comprehensive model that accurately predicts structural stiffness and damping coefficients of the FB structure and its interaction with the hydrodynamic film. The third section details the FB structural characteristics, stiffness and damping, and their identification via experiments and prediction using analytical models. The final section focuses on investigations of high-speed and high-temperature GFB reliability and durability.

GFB Advantages and Industrial Applications

Heshmat and Ku [2] note that a GFB adapts to shaft misalignments, variations due to manufacturing and assembly tolerance build-ups, centrifugal shaft growth, and differential thermal expansion. The authors foresee the potential for long life, higher load capacity, lower power losses, and superior rotordynamic characteristics of compliant surface bearings compared to conventional oil-lubricated bearings.

Agrawal [3] in 1997 reviews developments of foil gas bearings over the previous 25 years. The publication notes GFB higher reliability, no scheduled maintenance, soft failure, environmental durability, high speed operation, low and high temperature capabilities, and process fluid operations as the advantages of GFBs over conventional oil lubricated bearings. The environmental control system in aircraft regulates cooling, heating, and cabin pressurization in commercial and military aircraft. Successful FB applications in air cycle machines (ACM), vital components of the environmental control system, are noted for aircraft such as DC-10 and Boeing 767/757 environmental control system. The author predicts that FBs will increase efficiency and reduce the cost of various high speed turbomachines including high temperature applications.

Valco and Dellacorte [1] claim that recent technological developments in GFB load capacity, high temperature solid lubricant coatings, and rotordynamic and mechanical modeling and analysis enable the opportunity to overcome limitations of oil-lubricated bearings and yield improvements in weight, efficiency, performance in life cycle cost for military applications. The authors note that start-stop FB trials of more than 100,000 cycles at 1200°F give a maintenance-free bearing system for the life of the engine in certain applications. The authors include a four-step process for the transition from oil-lubricated systems to oil-free technology. This process proved successful in a turbocharger for a heavy-duty truck diesel engine. The next trial for the process was a small gas turbine engine sized for general aviation and business jet aircraft. Reference [1] suggests other FB applications including fuel cell compressors, single-use turbojet engines for missiles, reusable target drones and unmanned vehicles. The weight savings from removing oil-lubricant systems improves vehicle performance. System simplification and efficiency make the FB attractive due to new design freedoms of vehicle systems. Reduced parts (no oil system), virtually no maintenance, and improved durability make systems cheaper.

Fields [4] in 2004 predicts that by the end of the decade (2010) GFBs will be used in commercial turbojet engines. Aircraft engines soon will be lighter, require less maintenance and produce fewer harmful emissions. Recent work on air foil bearings

may lead to more efficient and less polluting aircraft as well as other innovative applications. NASA has done 100,000 start-stops at high temperature without wearing out the bearings, as shown in [1]. This is equivalent to 60 years of life in a jet engine, which is longer than the required life of an engine. The aforementioned technological advancements [1,4] evidence GFB usage exceeds the expectations of simple ACMs, auxiliary power units (APUs) and turbochargers.

GFB Theoretical Modeling and Predictions

Investigators have advanced models to predict the dynamic forced performance of GFBs. Each successive model considers an aspect of GFB performance not covered by a previous model. Peng and Carpino [5] improve on a 1983 method developed by Heshmat et al. [6], which neglected any damping effects in the bearing foil structure. The novel approach determines simultaneously the stiffness and damping coefficients using a finite difference formulation that couples the gas flow and structural system equations of motion. The model puts the hydrodynamic and structural support forces in series, which makes the GFB force coefficients frequency dependent. That is, at low rotor speeds, the fluid film is soft compared to the stiffness of the elastic foundation so the GFB compliance depends on the lubricant film. Conversely, at high rotor speeds the fluid film stiffness is higher than the elastic foundation stiffness, and the GFB compliance depends on the elastic foundation. The analytical results show that, generally, the GFB stiffness and damping decrease with bearing compliance, and the direct stiffness increases with rotor speed. A significant limitation of this model is that it neglects Coulomb friction, and the resulting damping, of the top foil/elastic foundation mechanism.

Around the same time as in [5], Ku and Heshmat [7] present a theoretical model to predict the structural characteristics of bump foil strips under various load distributions. The model also includes the effects of friction forces between the bump foils and bearing housing and top foil, local interaction forces between bumps, and various bump strip configurations. This work is the first step in understanding the

complex friction and interactive forces of the structural member, but more importantly the effects of the friction and interactive forces on local and overall stiffness and damping characteristics of FBs. Predictions show the stiffness in bumps near a fixed end is up to three times greater than in those bumps near a free end. This is due to the accumulation of the friction forces from the free end towards the fixed end, which can cause some of the bumps to become fixed (pinned-end condition). Therefore, the load location and its distribution along the bump strip influence the overall stiffness of the bump strip. Bumps with a pinned-end like condition have very high stiffness but provide no frictional damping. The results also indicate that increasing the friction between the bumps and the top foil is the best means of achieving the most damping.

Ku and Heshmat [8] conduct experiments to verify the model in [7]. The investigation evaluates the effects of bump geometry, load profile, surface coating, and lubrication type on the structural characteristics of bump foil strips. A microscopic video tracking system records bump deflections caused by a hydraulic MTS machine. A pivot system detailed in [8] allowed the variation of the load profile onto the bump strip. As the MTS machine applied a compressive load, vertical deflections of the bumps determined stiffness and horizontal motion of the bumps indicated damping. Interestingly, a six-bump strip replaced the original 13-bump strip because the original strip would not deflect under the applied load range. The six-bump strip evidenced visible deflection and measurements were possible. This agrees with the finding in [7] that the friction forces are cumulative from the free end towards the fixed end of the top foil. Bump strips of varying geometry (thickness and bump pitch) were used for testing, and results show that bump pitch is the most important influence on stiffness. Results also show that load distribution greatly influenced the bump foil overall stiffness. The investigators varied the surface coatings on the foils to determine the influence of friction coefficients on stiffness. Obviously, the coatings with higher friction coefficients increased the overall stiffness. Testing also included the addition of lubricating oil to the foil interface, and, interestingly, the result from the oil-lubricated

case compared to the "dry" case evidenced no effect on the overall stiffness of the bump strip.

Peng and Carpino realized the shortcomings in [5] that assumed no damping in the foil/elastic foundation structure. Peng and Carpino [9] develop a new model for stiffness and damping calculations as a function of Coulomb friction values. Similar to [7], Peng and Carpino calculate the Coulomb friction in a bump as the accumulation of the friction from the bumps at a free end towards a fixed end. Therefore, the damping of a bump foil structure varies spatially and decreases as a bump is further away from a welded end. The concept of equivalent viscous damping is finally introduced. The equivalent viscous damping coefficient is calculated by equating the energies dissipated by frictional damping and viscous damping (proportional to velocity), respectively, for a cycle of excitation. The authors find that the stiffness and damping coefficients generally increase as the Coulomb friction increases.

Ku and Heshmat [10] then introduce an enhanced model of their previous work in [7] that treats Coulomb friction as a dissipative force. The equations presented in the work determine reaction forces (radial and circumferential), bump deflections, bump displacements, and equivalent friction coefficients. Bearing stiffness is calculated based on the perturbation of the journal center with respect to its static equilibrium position. The equivalent viscous damping coefficient is determined from the area of a closed hysteresis loop of the journal center motion. The authors present two sets of equations for calculating damping coefficients. One set is strictly friction-based and the other set is based on the applied load, or displacements. Comparison of the results show the solutions for the two sets are close; therefore, the authors conclude the equivalent viscous damping coefficients are mostly contributed by Coulomb damping. This corrugated strip model is the most comprehensive to date, since it considers nearly every aspect of bump interaction and frictional mechanisms.

Swanson and Heshmat [11] published a two-part paper concerning how the structural elastic sub-layer and hydrodynamic gas film layer can best be modeled to obtain the GFB stiffness and damping coefficients. The structural elastic layer consists

of the bump foils, and the hydrodynamic film layer of the fluid film between the rotor and top foil that results from high speed rotor operation. The elastic structural layer offers frictional (Coulomb) damping due to relative movement between the bumps and top foil and stationary housing. This investigation shows how the predictions from a 2-DOF structural model differ from those from a conventional linear 1-DOF model. The 1-DOF model has the spring stiffness and the hydrodynamic film stiffness in series with a dashpot. The dashpot in this model is considered a combination, i.e., no distinction, of the viscous damping of the fluid film and Coulomb damping. The 2-DOF model considers the motion of the shaft and the motion of the top foil (the top foil mass is negligible in relation to that of the rotor). Each distinct layer provides its own stiffness and damping, as evidenced by a phase lag in the response of the top foil to rotor deflection during experiments.

GFB Structural Characteristics: Performance and Influence of Parameters

The enhanced model and computer program presented in [10] allow Ku and Heshmat to perform a parametric analysis [12]. Four parameters are varied including load angle (pad angle), static load (eccentricity), dynamic load (perturbation magnitude), and friction coefficients to evaluate their effects on the theoretical performance of the bump foil strips. The authors use the results from the parametric study to develop more effective methods of optimizing structural stiffness and introducing Coulomb damping in a given FB design. Recall that [10] includes the effects of the housing curvature and bump movement either to the left, to the right, or pinned. Then the stiffness and equivalent viscous damping are determined with respect to this location. The results of the load angle study show that stiffness and damping are at their maximum values as the applied load is directed at the center of the bump foil strip. Conversely, stiffness and damping are at their minimum values when the load angle is directed between bump foil strips. Results show that stiffness and damping increase nearly linearly with static displacement (eccentricity). The dynamic load studies show that an increase in this parameter causes both direct stiffness and damping to increase. A friction coefficient

value of zero (0) produces no damping. Damping increases up to an optimum value of friction coefficient after which the damping decreases. Increasing the friction coefficient increases the bump stiffness, which again leads to decreased damping above the optimum value. The friction coefficient study indicates that the friction between the bump foil and top foil and between the bump foil and curved bearing housing contribute about the same amount to the damping coefficient. Evidently, this indicates the importance of the curvature effect considered by this model. Recall in their previous model presented in [7], Ku and Heshmat find that increasing the friction coefficient between the bumps and the top foil is the best means of achieving the most Coulomb damping. This landmark paper describes for FB designers methods for optimizing dynamic structural stiffness and damping. Designers may use any combination of the following methods: 1) use a coating with a high friction coefficient, 2) increase the bearing static load, 3) decrease bearing dynamic force, or 4) apply the bearing static load to the center of a bump foil strip.

Heshmat and Ku [2,13,14] published three papers discussing experimental investigations on the structural force coefficients of bump foil strips used in foil bearings. A test facility with a non-rotating journal supported by a foil bearing was built. The journal was driven by two orthogonal shakers, which simulated dynamic forces acting on the bump foil strips of the bearing. The dynamic structural stiffness and equivalent viscous damping coefficients are calculated using two data reduction schemes, namely force equilibrium on the journal and on the bearing housing. The results are compared to analytical predictions obtained from their model developed in [10,12]; good agreement is evident. In [2] the tests determine the effect of dynamic displacement amplitude, or dynamic load amplitude, on the dynamic force coefficients. Theoretical and experimental results show that increasing dynamic amplitude decreases both stiffness and damping, despite energy dissipation increasing. In [13] they determine the effect of static load on the dynamic structural properties of the bump foil strips. Results show that damping increases almost linearly with increasing bearing static load since friction forces and energy dissipation also depend on static load.

Results also show that stiffness increases in the direction of increasing static load. In [14] the investigation determines the effect of frequency on the dynamic force coefficients. The theoretical model is quasi-static, and thus, the predicted force coefficients are frequency independent. However, dynamic excitation is shown to decrease the influence of the stick-slip phenomenon (due to friction between contacting surfaces) during static loading and unloading. Thus, experimental results show that increasing excitation frequency increases the stiffness of the bearing in the static load direction, while decreasing the damping since it reduces the influence of friction. Discrepancies between predictions and experimental damping values are, perhaps, due to the energy dissipated from the sliding contact between the journal and the top foil, which is not considered in the model.

Dellacorte and Valco [15] introduce a simple "Rule of Thumb" (ROT) to estimate the load capacity of gas FBs. The authors claim the load capacity is a linear function of bearing surface velocity and bearing projected area. They introduce the empirically based load capacity coefficient, D, relating the maximum load, bearing geometry, and speed. Third generation foil bearings have load capacity coefficients up to 1.4, which is an improvement from first generation foil bearings with $D = 0.4$. The rule of thumb offers a simplified method to estimate load capacity of GFBs for certain applications.

Radil et al. [16] conduct tests to determine the effect of radial clearance on bearing load capacity. The authors compare results of two generation III bump-type FBs with different initial clearances. A clearance does not exist between the top foil and the shaft as with rigid surface bearings. The clearance refers to the amount of shaft displacement from the bearing's geometrical center until the compliant surface begins to resist displacement. A solid lubricant coating covers the shaft outer diameter. The investigators grind down this surface to decrease the shaft diameter, i.e. increase the radial clearance, for subsequent tests. A vertical loader applies loads incrementally until the hydrodynamic gas film breaks down and rubbing of rotor and top foil occurs. The load at which rubbing contact occurs between the shaft and bearing denotes the bearing

ultimate load capacity. This maximum load leads to the ROT formula of bearing load coefficient given in [15]. The bearing with tighter initial clearance has a lower load capacity than the bearing with larger clearance. Each bearing has an optimum clearance which evidences maximum load capacity. Decreasing the clearance heavily preloads the shaft, which may lead to rotor-bearing system failure due to shaft thermal expansion and seizure. When the bearing clearance is greater than optimal, the bearing load capacity decreases by less than 20% with no failure due to thermal effects.

Radil et al. do not consider the effect of radial clearance on bearing stiffness and damping in [16]. Rubio and San Andrés [17] investigate the effect of a mechanical interference between the shaft and bearing on foil bearing structural stiffness. Experimental results compare three test shafts of different diameter, i.e. varying degrees of preload, while applying static loads at various angular orientations. The static deflections versus load characteristics depend on the orientation of the applied static load relative to the position of the spot weld that connects the top foil to the bearing housing. Measurements show nonlinear foil bearing deflections. The bearing structural stiffness results from the derivative with respect to displacement of the third order polynomial fit of the load versus displacement curves. The investigators use a model that assembles the linear stiffness of the individual bumps and predicts FB structural stiffness as a function of bump geometry and material parameters, dry-friction coefficient, load orientation, radial clearance, and initial preload. Predictions show that the stiffness of a single bump is most sensitive to the dry-friction coefficient, the bump pitch, and the bump-ends conditions, i.e. welded or free to move. The predicted stiffness agrees with the experimentally derived structural stiffness. In all cases, increasing preload causes a higher structural stiffness.

Salehi et al. [18] present experiments to identify the dynamic structural stiffness and damping characteristics of a large 21.6 cm (8.5 in.) diameter compliant surface foil journal bearing. This study aims to achieve high levels of GFB damping for oil-free applications, while maintaining a nearly constant dynamic stiffness over a range of frequencies (up to 400 Hz) and amplitudes of motion (25.4 μm to 102 μm). The results

of this study show that damping values increase with static load up to a threshold, after which increasing the static load decreases the damping coefficient. As the excitation frequency increases, equivalent viscous damping values decrease, while dynamic stiffness varies only slightly. The results show that the bump foil is capable of providing stiffness and damping levels consistent with oil squeeze film dampers (SFDs) for the range of frequencies tested. At higher excitation frequencies these results may not hold since the equivalent viscous damping for GFBs decreases with frequency [2]. The authors state that additional investigations into the effects of preload, as in [16,17], and bearing materials are warranted.

Rubio and San Andrés [19] investigate the structural stiffness and equivalent viscous damping characteristics of a FB using dynamic loads of single frequency. They use the energy dissipation for one cycle method and the mechanical impedance identification method to identify bearing structural parameters. The test system evidences a resonance around 260 Hz. At this frequency system viscous damping is nullified, and displacements become large with small dynamic loads. Note that in a SDOF linear mechanical system the viscous damping coefficient should be constant regardless of dynamic load amplitude, which is not true in the tests. The equivalent viscous damping is inversely proportional to motion amplitude and excitation frequency, as also indicated in [18]. However, the tests show equivalent viscous damping coefficient increasing with increasing load. The stiffness (K) may also be estimated from the real part of the impedance, $\mathrm{Re}(F/X) = K - M\omega^2$, for excitation frequencies (ω) nearly equal to zero. Test results show that bearing stiffness decreases with an increasing amplitude of dynamic load. The dry friction coefficient increases as the load amplitude increases, ranging from 0.05 to 0.2. Stick-slip effects of dry friction increase the bearing stiffness at small amplitude dynamic loads. The investigators heat the shaft, but the temperature range considered (25°C to 75°C) is too small to produce significant changes in assembly preload that would affect the dynamic forced characteristics of the test bearing.

GFB High Temperature/High Speed Performance

Researchers at NASA have advanced relevant information regarding high speed/high temperature GFB performance with the development of solid lubricant coatings and test rigs to determine the feasibility of GFB use in a broader range of applications. Dellacorte [20] discusses a new test facility capable of providing measurements of load capacity, torque during start-up and shut-down and bearing durability for operating conditions up to 700°C and 70,000 rpm. The bearing load, speed and temperature are varied while measuring bearing friction (torque) during start/stop as well as while airborne. A torque rod attached to the bearing dead weight housing connects to a force transducer to measure bearing torque. A pneumatic loader can apply an additional 500 N to assess bearing power loss and load capacity. Experimental results show bearing torque is highest at low speeds due to the thin gas film and increases with applied load. The authors claim that load capacity decreases with temperature because the bearing support structure stiffness decreases as the temperature increases. Durability assessments consist of automatic start/stop cycling up to 40,000 rpm over a 20 second period and lasts up to 20,000 cycles. Friction levels peak just before lift-off (approximately 5,000 rpm), decrease while the fluid film is developed, and the reverse occurs during shut-down. At elevated temperatures, results show reduced torque peak values, and the author states this is because thermal expansion reduces bearing preload.

Dellacorte et al. [21] present results of durability and performance tests of high temperature 35-mm foil bearings. The authors evaluate system wear under a wide range of loads and temperatures from 25°C to 650°C. The bearings are made from uncoated nickel-based super alloy foils, and the investigators apply the solid lubricant PS304™ to the shaft to reduce friction and wear. The automatic durability test procedure and facility are described in [20]. Durability testing continues for 30,000 start/stop cycles, and micrometers measure the minimum foil thickness and the decrease in journal diameter to assess wear as a function of load and temperature. Bearing torque decreases with increasing temperature for the static load tested. The results show no clear relationship between wear and temperature. Tests, while varying the static load, show

foil and journal wear increasing linearly with applied load. The investigators also perform endurance tests to evaluate bearing life during 100,000 start/stop cycles. At room temperature testing is discontinued after 48,372 cycles due to excessive foil wear because the solid coating is much more abrasive at 25°C than at elevated temperatures. At elevated temperatures (up to 650°C), testing continued without failure through 100,000 cycles. Generally, the preload level between a bearing and its shaft is unknown. The authors, however, develop a method to estimate the preload by performing start/stop tests while varying the deadweight load. These data provide the relationship of bearing friction versus external applied load. The slope of the straight line fit of the data points gives the sliding friction coefficient for the bearing/coating tribopair. Further, by extrapolating the fitted line until it intersects the ordinate, one obtains the estimate of the friction force at zero deadweight load. Finally, dividing this friction force at zero applied load by the friction coefficient yields the amount of preload force produced between a shaft and bearing. Test results show preload force increasing by a factor of two between 204°C and 650°C and the authors give thermal expansion as the reason.

Note the apparent inconsistency regarding bearing preload as a function of temperature as stated in [20] and [21]. In [20], Dellacorte states the bearing torque is reduced due to thermal expansion, which leads to a reduction in preload as temperature increases. In [21] Dellacorte et al. state that bearing preload increases as a function of temperature. Dellacorte provides clarification via a personal communication [22] in which the author states the latter case is correct. In the former case, two factors most likely caused the decrease in bearing torque, namely, the PS304™ coating wear (decreased interference) and lower friction coefficients at higher temperatures. Neither of these two factors were measured at the time of [20], thus, the incorrect conclusion. The method described in [21] allows measurement of bearing preload force and, with the exception of the 25°C case, shows the currently accepted understanding.

Howard et al. [23] conduct experiments to determine GFB stiffness and damping characteristics as shaft speed, static load, and temperature vary. Results are obtained over a range of modified Sommerfeld Numbers, $S = 1.5 \times 10^6$ to 1.5×10^7. S is a function

of load, temperature-dependent viscosity, and rotor speeds up to 30,000 rpm. Loads varied from 11 N to 90 N and temperatures from 25°C to 538°C. The results are given for 34.9 mm (1.375 in.) diameter bearings. The investigators use a 2-DOF model to describe the behavior of the bearing as in [12]. The authors fit the bearing dynamic displacement test data to an exponential decay curve and a linear decay curve. If the exponential fit is better, the bearing damping is of viscous type. However, if the linear fit is better, then the bearing damping is of dry friction type. Otherwise, if neither fit is substantially better than the other, then the bearing behaves with a combination of both types of dissipation mechanisms. This method distinguishes in which operating region the gas film dominates the bearing performance versus the region of operation where the foil sub-structure dominates. The authors provide general guidelines for GFB behavior with varying load, temperature, and speed. For example, if a bearing operates at low load and high temperature conditions, then viscous damping of the fluid film dominates bearing behavior. Thus, adding high-friction coatings to the foils will not help bearing damping in this operating domain. However, increasing the mechanical preload on the bearing activates the bump motion more with the low load condition, and this increases the frictional damping contribution. Bearing designers can use these guidelines to tailor bearing properties for the operating domain of a particular application.

To conclude this brief review of the analytical and experimental work on bump-type GFB characterization, it must be upheld that predictions of ideal interactions between a FB and shaft may not sufficiently describe actual conditions. Properly characterizing the FB structural behavior provides the basis for FB performance once the hydrodynamic film is introduced during rotational operation.

III DESCRIPTION OF TEST FOIL BEARING AND EXPERIMENTAL FACILITIES

This section describes the test FB, a test shaft, and the experimental facilities used for static and dynamic load tests. A detailed overview of the main dimensions and material properties of the test FB and test shaft is provided. The clearance between the shaft outer diameter and the FB inner diameter is defined. Also, geometric dimensions and material properties of the FB components allow prediction of the behavior of the clearance as the shaft temperature increases. Recent changes to the dynamic shaker test rig and the motivation for the changes are detailed. A cartridge heater and the control circuit allow static and dynamic experiments up to 188°C, which is the temperature limit of the protective coating on the FB.

Description of the Test Foil Bearing and Test Shaft

Figure 2 shows a cross-section of the foil bearing installed on a static journal. The FB has three major structural components: 1) bearing housing, 2) bump foils, and 3) top foil. The bearing housing is made of AISI 304 stainless steel, and the bump foils and top foils are made of Cr-Mb steel. An Emralon 33 spray-on coating applied to a thickness of 25.4 μm [17] to the top foil acts to protect from wear damage.
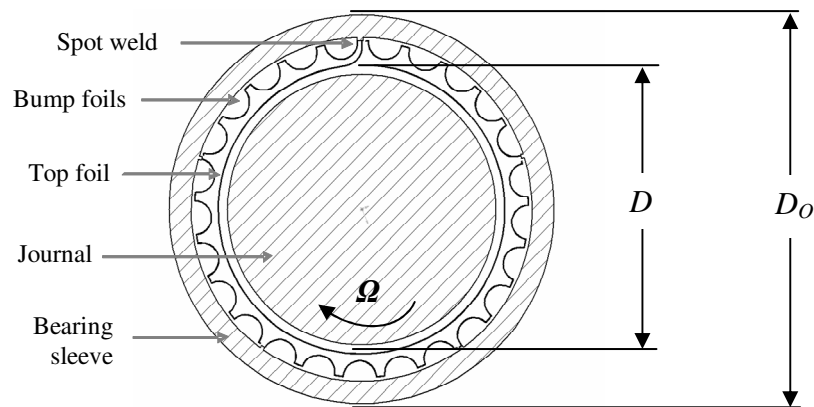
Figure 2 Cross-section of journal and bearing assembly labeling major components.

Table 1 gives the nominal dimensions and specifications of the test bearing as provided by the bearing manufacturer [17].

Table 1 Nominal dimensions and material specifications of test bump foil bearing

Parameters and Dimensions	Symbols	Values
Inner diameter, mm [in]	D	38.17 [1.5028]
Outer diameter, mm [in]	D_O	50.80 [2.00]
Axial bearing length, mm [in]	L	38.10 [1.50]
Radial nominal clearance[1], mm [in]	C_{nom}	0.0229 [0.0009]
Number of bumps	N_B	25
Bump pitch, mm [in]	s	4.572 [0.18]
Bump length, mm [in]	$2l_o$	4.064 [0.16]
Foil thickness, mm [in]	t	0.1016 [0.004]
Bump height, mm [in]	h	0.381 [0.015]
Poisson's ratio	υ	0.29
Modulus of elasticity, GPa [psi]	E	213.7 [$31*10^6$]
Bearing mass, kg [lb]	M_B	0.278 [0.613]

Figure 3 shows a schematic view of a FB with the location of bump foil weld junctions. Five bump foil strips support one top foil. Each bump strip spans 70° around the inner circumference of the bearing housing. One bump strips shares the spot weld with the top foil; the other bump strips are welded separately. The figure also shows the weld location orientation coordinate, φ. Notice that angle φ initiates at the free end of the top foil and increases in a direction towards the top foil fixed end.

---

[1] Nominal clearance is for a 38.125 mm [1.501 in.] diameter shaft base on information provided by the manufacturer.
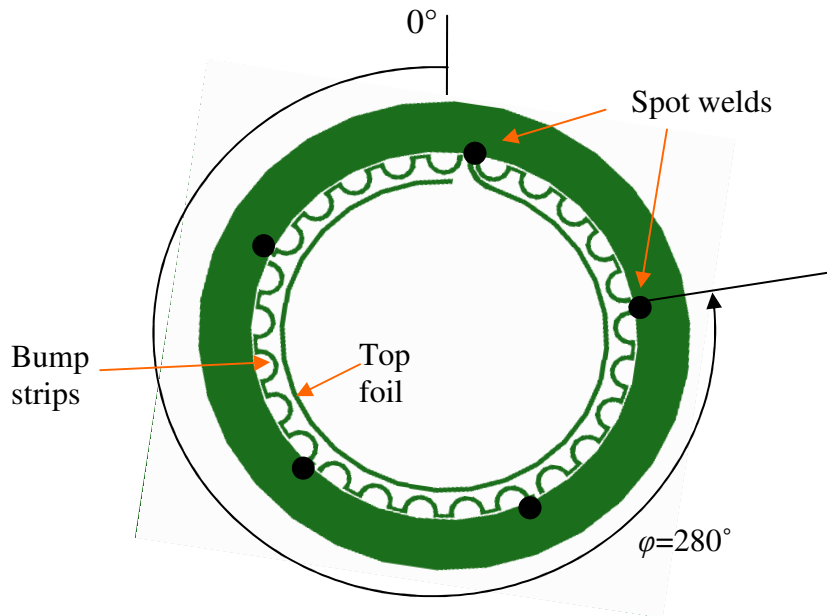
Figure 3 Schematic view of FB with bump strip spot weld locations every $\varphi=70°$.

The uncoated test shaft, made of AISI 4140 steel, consists of a hollow test portion with a wall thickness of 6.35 mm (0.25 in.), length of 88.9 mm (3.5 in.), and outer diameter of 38.125 mm (1.501 in.) at the bearing location. Figure 4 shows the test shaft and its main dimensions. The test portion has a polished (20-micro inch) finish. The solid shaft reduced cross-section portion is 133.35 mm (5.25 in.) long and 24.89 mm (0.98 in.) in diameter. A fillet radius of 6.35 mm (0.25 in.) at the diameter change reduces stress concentrations and deflection. The open end of the test shaft allows the insertion of a cartridge heater, as described below. The inner diameter of the hollow portion matches the diameter of the cartridge heater (nominal 1.0 in.) such that the heater must be forced into position (null interference). This allows excellent heat conduction to the shaft once power is supplied to the heater.

Ø 38.125 +/-0.00635 mm
(1.501+/-0.00025 in.)

133.35 mm (5.25 in.)

76.2 mm (3.00in.)

Indexing Fixture Chuck

Test Bearing Section

Ø 24.89 mm (0.98 in.)

R 6.35 mm (0.25 in.)

Ø 25.4 mm (1.0 in.)
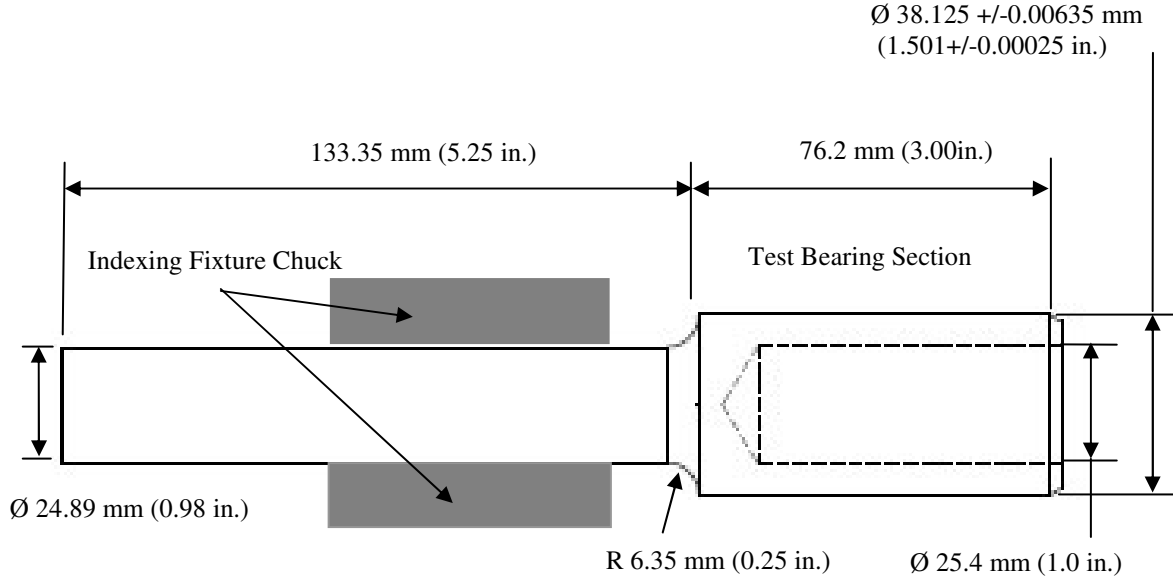
Figure 4 Dimensions of rigid test shaft

Description of Static Load Test Setup

A lathe provides a stationary support and loading mechanism for static load tests. Figure 5 shows a 4140 steel test shaft secured in the lathe chuck and the bearing supported on the shaft. The lathe tool holder applies static load, F, to the bearing by way of the hand dynamometer. The dynamometer provides force measurements (+/- 1.112 N [0.25 lb]) proportional to the translational motion of the tool holder with respect to the bearing. An eddy current sensor (ECS) records displacement (x) as the bearing moves due to the applied force. Figure 6 shows the test setup for increased temperatures (up to 188°C). Thermocouples (Type K) provide temperature measurements of the shaft and bearing housing surfaces. The cartridge heater inside the shaft, monitored and controlled by an external circuit, provides a controllable heat source.
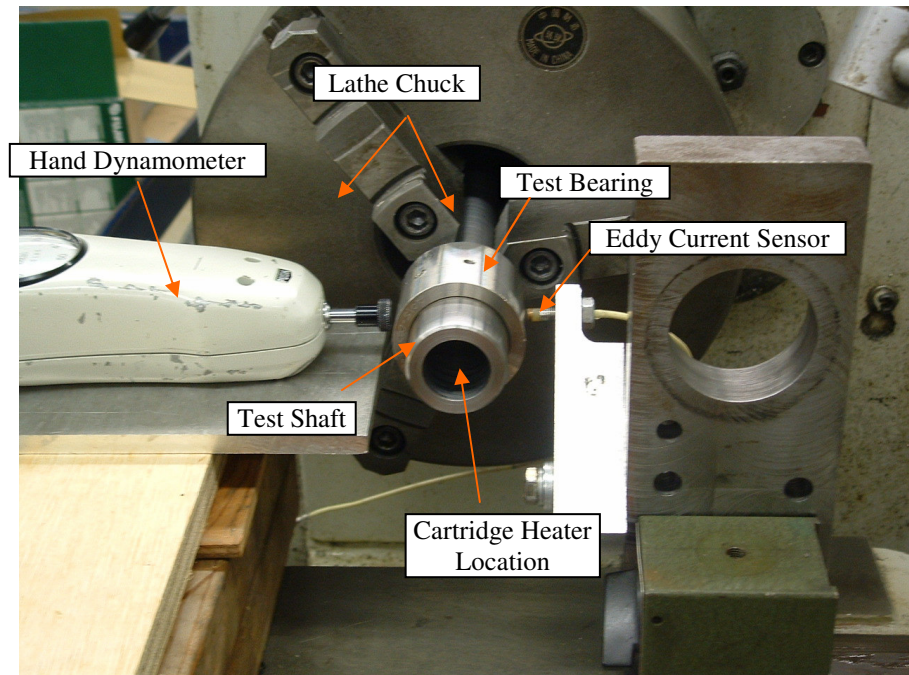
Figure 5 Test setup for static experiments at room temperature (side view).
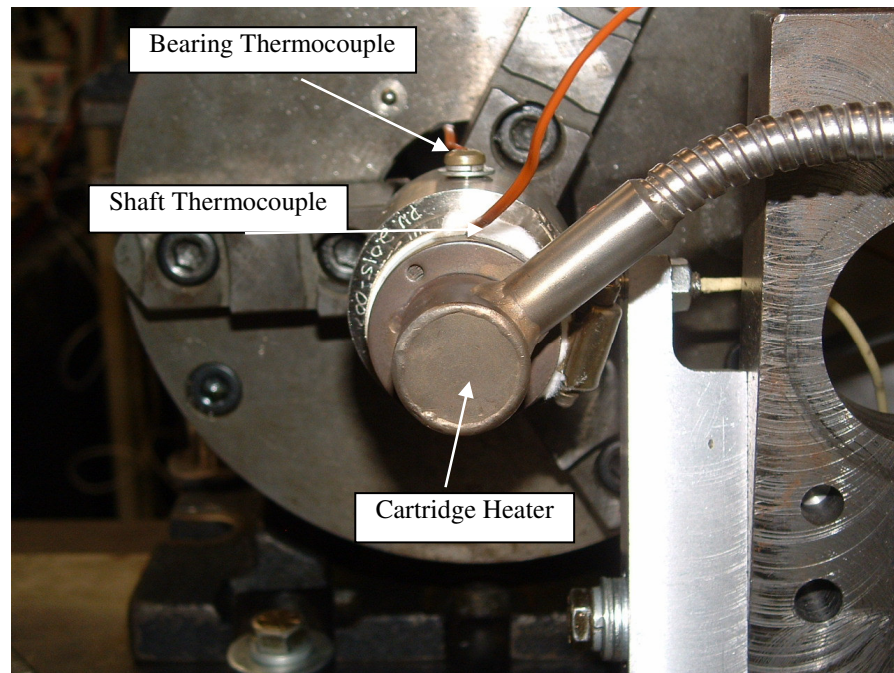
Figure 6 Cartridge heater and thermocouple locations for high temperature static load tests (side view).

Description of Electromagnetic Shaker Test Rig

Previous testing using the dynamic test setup used in [19] presented several issues that have been addressed. The aluminum shaft support was not rigid and proved to deflect under dynamic loading on the bearing. Also, the electromagnetic shaker was rigidly mounted to the laboratory table. This arrangement caused issues with parasitic vibrations throughout the table, shaft support, and eddy current sensor (ECS) mount. For example, to eliminate ECS mount resonance in the test frequency range, and the corresponding error in displacement readings, evidence shows that an ECS mount redesign was necessary. Thus, an ECS mount designed with a higher stiffness (natural frequency ~432 Hz) proved sufficient. Also, shaft and stinger alignment became critical. For example, test results comparing the FB displacement magnitudes and the FB displacement derived from acceleration magnitudes showed that, during dynamic excitation, one end of the bearing moved more or less than the opposite end. That is, the bump foil sub-structure did not experience uniform loading along its axis, which led to poor experimental repeatability and high uncertainty.

Thus, a primary task of was to re-design and build a suspension system for the electromagnetic shaker by reducing its support stiffness to less than that of the rigid shaft and support system. Assuming a rigid shaft and support system, the bearing mass is the only portion of the system in motion. Figure 7 shows the suspended shaker hanging from the test laboratory ceiling. Four coated steel cables (2 m long) connect the turnbuckles in the shaker base to a square plate that is connected by a bolt to a bracket in the ceiling (not pictured). The bolt through the square plate allows for large height adjustment, while the turnbuckles provide fine height adjustments and leveling. Initially the shaker stinger height matches the height of the centerline of the rigid shaft. Then, a digital level ensures that the flat shaker base rests at a 0° incline with ground.
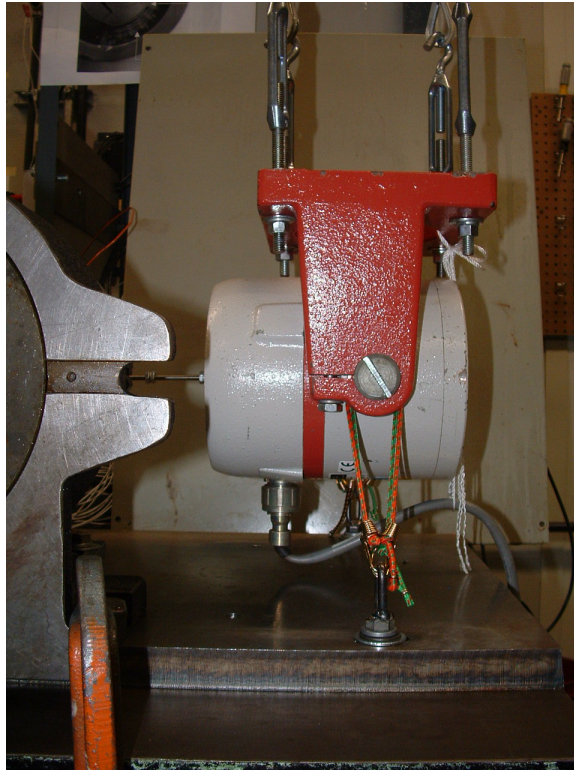
Figure 7 Suspended electromagnetic shaker setup including turnbuckles for leveling and height adjustment.

Figure 8 shows a top view of the test rig to conduct dynamic load experiments of a FB supported on a hollow shaft. A massive vertical/horizontal indexing fixture holds a reduced cross-section of the test shaft in its chuck. The fixture provides a rigid support for the shaft and minimizes relative motion between the shaft and ground such that during shaker testing the bearing is the only component moving. The natural frequency of the shaft and indexing fixture assembly is approximately 380 Hz, as identified in rap tests of the shaft in the horizontal direction. The electromagnetic shaker provides a periodic load of varying frequency. A LabVIEW® program analog output controls the shaker amplitude and frequency. Tests are conducted with loads of up to 31.1 N and over a frequency range from 40 Hz to 200 Hz.
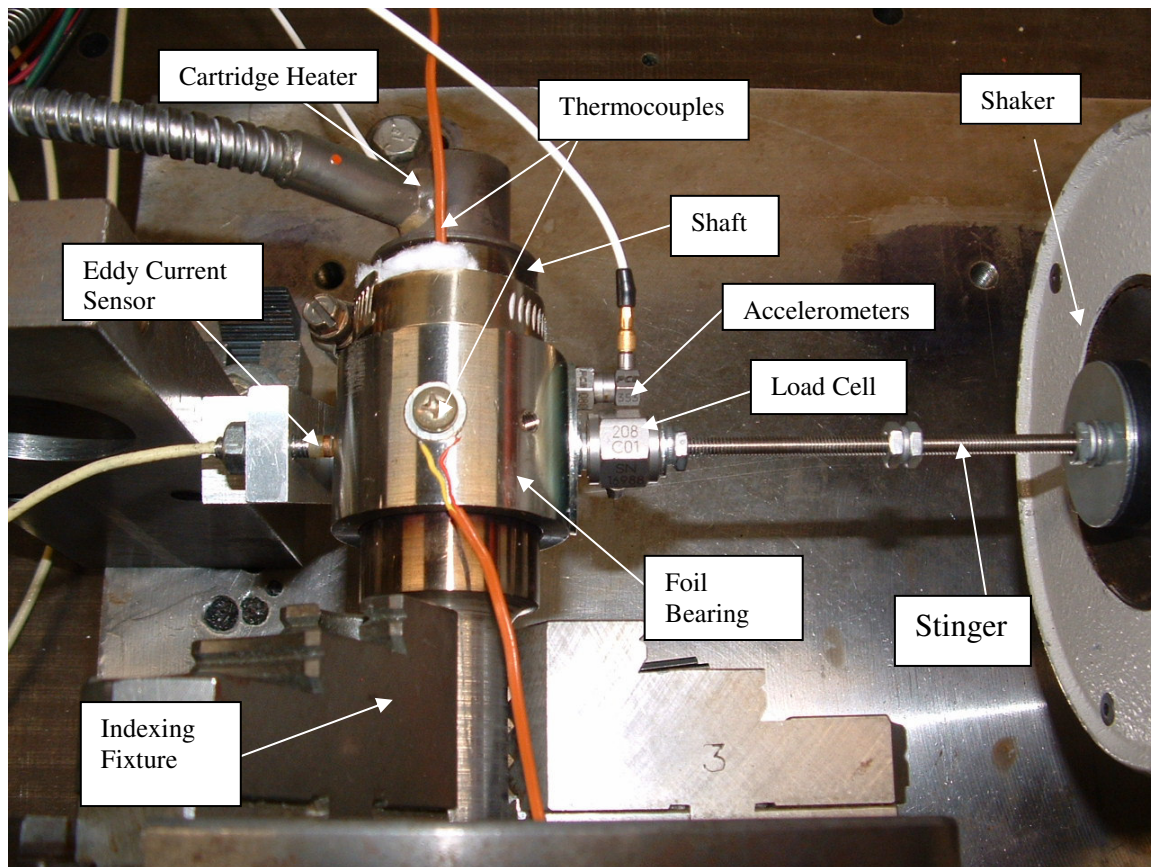
Figure 8 Test rig for structural force coefficient experiments of a *FB* supported on a rigid shaft (Top View)

Measurements of the foil bearing lateral displacements are taken with an ECS system (gain = 10.93 +/- 0.04 V/mm [278 +/- 2 mV/mil]^2). The sensor measures horizontal displacements of the FB mid-span on the side opposite the shaker. Voltage signals from the eddy current sensor are conditioned and then input to a DAQ system.

Dynamic loads applied to the bearing are measured by a piezoelectric load cell, which has a maximum temperature rating of 121°C (250°F). The load cell is threaded directly into the bearing housing at its axial mid-span. The sensitivity of the load cell is 111.4 mV/N (495.6 mV/lb). Measurements of the FB lateral accelerations are taken with a piezoelectric accelerometer. The accelerometer is magnetically mounted to a

---

^{2} ECS gain and uncertainty are reported in Appendix A.

metal washer that is tightened between the FB stainless steel housing and the load cell. The temperature limit of the accelerometer is also 121°C (250°F) and its sensitivity is 9.81 mV/g. These two measurement signals are output from the sensors to the DAQ board.

Finally, a LabVIEW® program provides signal control, real-time data display, and data acquisition. The operator inputs the test frequencies, the target load cell voltages (dynamic load amplitudes), and the preferred load tolerance. The tolerance is the acceptable amount of voltage, corresponding to the physical unit, above and below the target value at which data is saved. The program initializes the shaker at the first input frequency, while monitoring the output voltage of the load cell at a certain sample rate. If the output voltage is outside the tolerance range, then the program automatically adjusts the shaker amplitude to get closer to the target value. This iterative process of shaker amplitude adjustment continues until the load cell voltage is within the specified tolerance of the target voltage (load). If the load cell voltage stabilizes within this tolerance for five iterations, and the shaker requires no adjustment, then the program automatically saves the data for that load and frequency combination. The data saved includes the applied load, FB displacement and acceleration signals at the specified frequency. The display on the PC monitor includes a digital oscilloscope for the time signal and a frequency analyzer for the FFT of the input. Each scope is single-channel but the operator selects the signal to display. The stored data in ASCII form is subsequently used in analysis.

Cartridge Heater and Control Circuit

The cartridge heater, with nominal 25.4 mm (1.0 in.) outer diameter, is rated at 600 W when supplied with 240 V. The Texas A&M laboratory facility is wired to supply 120 V, which reduces the available heater power to 150 W. However, as determined through prior testing, this is sufficient to increase the test shaft temperature to over 320°C in less than 15 minutes. The heated section of the heater is less than 63.5 mm (2.5 in.) long. Since the heater simply provides an electrical resistance, a variable-

resistance voltage controller, or potentiometer ("pot"), must be incorporated into the heater's circuit to adjust the output temperature. It is desired to perform tests at intermediate temperatures, and manual control of the pot does not provide a suitable control. Therefore, a mechanical relay is built using digital temperature controller. The controller provides a means of monitoring and regulating the shaft temperature by opening the heater's electrical circuit once a specified target temperature is exceeded. If the shaft temperature falls below the given target, the relay closes the circuit, and current is again supplied to the heater.

Thermocouples (Type K) provide temperature measurements of the shaft and bearing housing surfaces. The cartridge heater inside the shaft, monitored and controlled by an external circuit, provides a controllable heat source. Bearing housing surface temperatures never achieve the same temperature of the shaft surface for a given test condition. Table 2 shows the shaft and bearing surface temperatures experienced during tests.

Table 2 Measured bearing surface temperature for corresponding shaft surface temperature

Shaft Surface Temperature (+/-1.0 °C)	Bearing Outer Surface Temperature (+/-0.5 °C)
22	22
77	67
132	110
188	155

IV CONSIDERATIONS ABOUT FOIL BEARING AND TEST SHAFT GEOMETRY AND MATERIAL BEHAVIOR DUE TO TEMPERATURE INCREMENTS

This Section establishes the geometric clearance between the test FB components and the 38.125 mm test shaft. A clearance differential is defined to determine changes in the bearing clearance with changes in shaft temperature. Next, the results of radial thermal expansion measurements of the FB housing and test shaft outer surfaces are given. A one dimensional radial conduction heat transfer model allows estimation of the FB housing inner surface temperature for the purpose of calculating the expansion of its inner radius. Finally, the above relationships and material behaviors are used to determine the changes in radial clearance with increasing assembly temperature.

Estimation of Bearing Radial Clearance from Geometry of Components

Figure 9 shows a one-quarter cross-section view of the FB and test shaft assembly. Dimensions are noted in the figure. Figure 10 shows a magnified view of the foil thickness layer height (Q) and its dimensions.
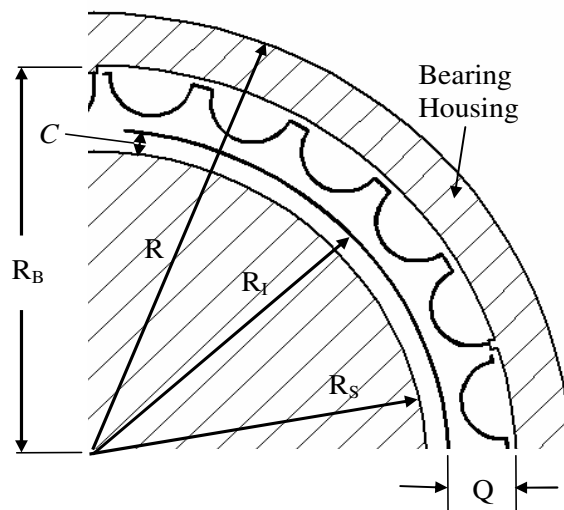
Figure 9 Detail of FB geometry and shaft dimensions.
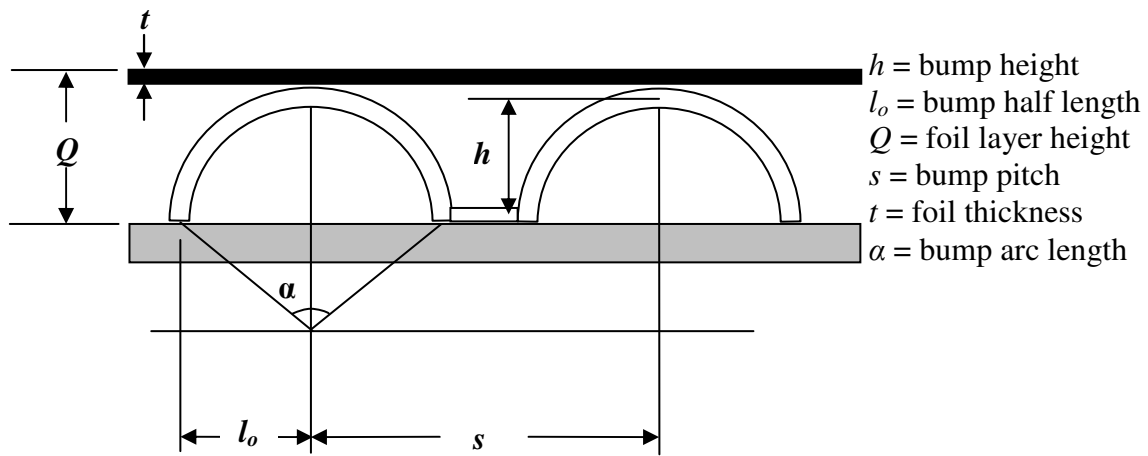
Figure 10 Detail of the top foil and bump foil layer height, *Q*.

The bearing radial clearance is given as

$$C = R_I - R_S \qquad (1)$$

where R_I is the FB inner radius and R_S is the measured test shaft outer radius. The FB inner radius, measured to the top foil, is

$$R_I = R_B - Q \qquad (2)$$

where R_B is the inner radius of the FB housing and Q = 0.5842 mm is the foil layer height. The bump foil and top foil layer height is

$$Q = 2t + h \qquad (3)$$

where t = 0.1016 mm is the bump foil and top foil thickness and h = 0.381 mm is the bump height (measured to the midspan of the foil), provided in Table 1.

Assembling Equations (1) and (2) leads to

$$C = R_B - Q - R_S = R_B - (Q + R_S). \qquad (4)$$

The inner radius of the bearing housing is $R_B = R - W_B = 19.6723\,mm$ where W_B = 5.7277 mm (0.2255 in.) is the bearing housing wall height measured by a digital caliper (uncertainty: 6.35 μm [0.25 mil]). The wall thickness given by the dimensions of the manufacturer is 5.73024 mm (0.2256 in.). The difference between the measured and

provided wall thicknesses is 2.54 μm (0.1 mil), which is within the uncertainty of the digital caliper.

The calculation of the FB inner radius (to the top foil) follows:

$$R_I = R_B - Q = R_B - (2t + h) = 19.0881 mm.$$ (5)

Comparison of the FB inner radius given by the manufacturer (19.08556 mm) and the calculated value R_I = 19.0881 mm shows a discrepancy of -2.54 μm (-0.1 mil), which is the difference between the wall thickness measurement and the wall thickness based on manufacturer specifications.

Finally, the estimated clearance, C_g, for a 38.125 mm (1.501 in.) diameter shaft based on measurements of the test bearing wall thickness and the $t = 0.1016$ mm and $h = 0.381$ mm given by the manufacturer is $C_g = R_I - R_S = 25.4 \mu m$. The estimated radial clearance from measurements between the test shaft and bearing is approximately 25.4 μm (1.0 mil) compared to C_{nom} = 22.9 μm (0.9 mil), see Table 1. However, this discrepancy is due to the uncertainty associated with the digital caliper used to measure the wall thickness of the FB housing.

Definition of Clearance Differential

Note that the 38.125 mm shaft is sufficiently smaller than the inner diameter of the bearing (see Table 1); therefore, the shaft does not induce a mechanical preload on the bump strips, along the applied load direction. The FB top foil rests on the top of the shaft. The FB weight resting on the shaft causes small deflections, on the order of 1 μm, of the bumps in this region of the bearing. However, the bumps on the sides of the bearing remain unloaded prior to external loading. Changing the shaft temperature changes the actual clearance between the shaft and the inner diameter of the bearing (to the top foil) due to the expansion of test component materials. The clearance differential, δC, is the difference between the nominal radial clearance and the actual radial clearance (C_{act}) between the shaft and its bearing; i.e., $\delta C = C_{nom} - C_{act}$. Rewriting this equation gives a useful form, $C_{act} = C_{nom} - \delta C$. Note that a negative δC

indicates an increase in radial clearance. Accordingly, if $\delta C = C_{nom}$, then there is actually no clearance; that is, $C_{act} = 0$ mm. Also, if $\delta C > C_{nom}$, then a mechanical preload does exist, and $C_{act} < 0$ mm.

Coefficients of Thermal Expansion of Test Setup Components

The expansion of each test component must be determined to predict the radial clearance between the shaft and the bearing top foil as the shaft temperature changes. This section demonstrates a method to extract the coefficients of thermal expansion (CTEs) from experimental measurements of the increase in radius of each component. The test shaft is set up in the chuck of the indexing fixture. The eddy current sensor (ECS) probe tip points towards the target, either the shaft of the bearing housing. The initial ECS reading is noted at room temperature ($T_S = 21°C$). The cartridge heater control circuit is set to the first temperature ($T_S = 55°C$). Once the shaft surface temperature reaches the target temperature, and the relay begins to cycle to maintain this target temperature, another 30 minutes elapse before noting the change in ECS voltage. The same procedure ensues for the other test temperatures (89°C, 122°C, 155°C, and 188°C). Each temperature has a corresponding ECS value. The change in the ECS voltage for each subsequent temperature gives the change in radius of the target. Table 3 gives the ECS gains calibrated for each target.

Table 3 The calibrated ECS gains and uncertainties for the AISI 4140 steel test shaft and AISI 304 stainless steel bearing housing used for CTE experiments

Target Material	Gain (V/mm)	Uncertainty (V/mm)
Test Shaft (AISI 4140 Steel)	8.40	0.016
Bearing Housing (AISI 304 Stainless Steel)	10.93	0.036

The test shaft and the FB housing radial expansions for a range of temperatures (up to $T_S = 188°C$) are noted and the CTEs are calculated via the formulas

$$\alpha_S = \frac{\delta R_S}{R_{S,i}\Delta T_S} \text{ and } \alpha_B = \frac{\delta R_B}{R_{B,i}\Delta T_B}, \tag{6}$$

respectively. The CTE estimation may occur in two ways. First, the total change in the radius and the total change in temperature can be used in the equation and the uncertainty (calculated in Appendix B) may be added. Or, the incremental change in the radius and the incremental change in temperature can be used in the equation and an average and standard deviation of the sample may be obtained.

AISI 4140 Steel Test Shaft

The hollow portion of the test shaft spans 63.5 mm, and the solid portion is approximately 12.7 mm long (see Figure 4). The cartridge heater fits into the hollow portion and contacts the solid portion inside the shaft. The heater conducts heat well radially into the hollow portion of the shaft but not well axially into the solid portion. Thus, there exists an axial thermal gradient along the shaft length as heat is conducted through the thin walls to the solid portion of the test shaft.

A FE heat transfer analysis of the test shaft provides insight of the temperature distribution along the length of the shaft. A constant heat flux is supplied at the inner diameter of the hollow test portion of the shaft, while free convection (coefficient h_{air} = 10 W/m^{2}K) occurs at all boundary surfaces of the shaft to surrounding air at 21°C (ambient). The constant flux is adjusted until the shaft outer temperature reaches approximately 191°C, which is close to the maximum test shaft temperature experienced during current testing. Figure 11 shows the resulting FEA temperature distribution through the shaft for these conditions. The results indicate over a 20°C temperature gradient along the 72.6 mm long test portion of the shaft. There is over a 60°C temperature gradient over the total length of the shaft.

Actual measurements of the shaft outer surface temperature verify an axial thermal gradient along the shaft. Temperature measurements are taken at three locations along the shaft from the direction of the open end of the shaft. The reference thermocouple, which controls the heater circuit, is located 10 mm away from the open

end of the shaft. A second temperature reading is taken at the location where the FB center rests during static and dynamic tests, 32 mm from the open end of the shaft. The third measurement is taken near the end of the cartridge heater, 58 mm from the open end of the shaft. The reference temperature (T_S) is set as the target temperature, which is monitored by the reference thermocouple. After the target temperature cycles for 30 minutes, the measured temperatures at the other locations are recorded.
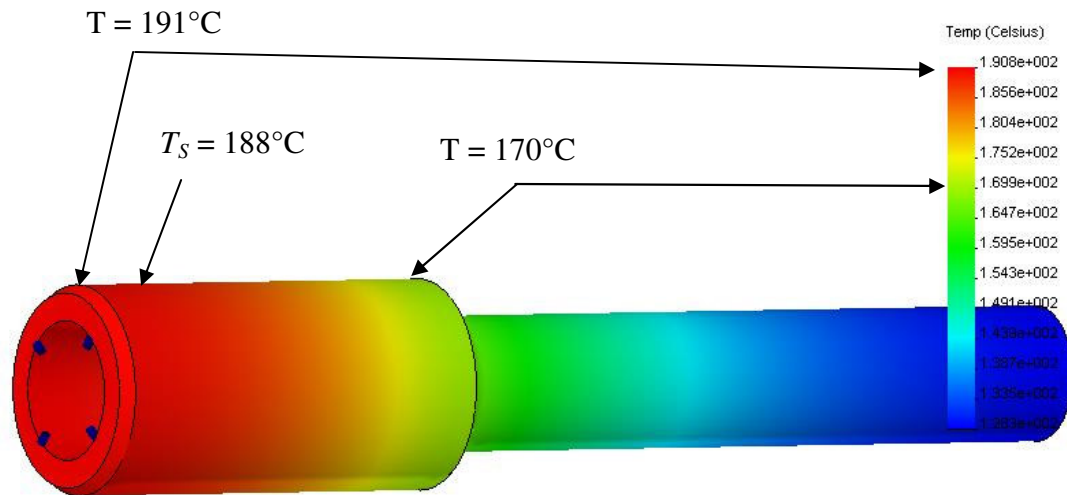
Figure 11 Thermal FEA analysis of test shaft showing an axial thermal gradient of 20°C along the 38.125 mm outer diameter portion of the test shaft.

Table 4 provides the results from each of the temperature trials measuring the change in shaft surface temperature for three increasing temperature cases, namely 77°C, 132°C, and 188°C. Note the temperature drop from the reference thermocouple to the location of the FB center is only 1°C for each of the tests. The more significant temperature drop occurs from the FB center location (32 mm) to near the end of the heater (58 mm). This indicates the thermal losses due to axial conduction from the thin-walled portion to the solid end of the shaft are considerable. Again, the poor axial conduction of the heater to the solid portion of the shaft causes this increased temperature gradient.

Table 4 Summary of shaft surface temperature measurements at 10 mm (reference), 32 mm (FB center), and 58 mm (near cartridge heater end) showing actual thermal gradient along the test shaft length for shaft reference temperatures (T_S) of 77°C, 132°C, and 188°C

	Shaft Surface Measurement Location[3]		
	10 mm	32 mm	58 mm
Reference Temperature	Measured Temperature (°C)		
$T_S = 77°C$	77	76	73
$T_S = 132°C$	132	131	124
$T_S = 188°C$	188	187	176

The heat transfer FEA allows detection of the resulting temperatures at any point of a solid part. This tool was used along the axial direction of the test portion of the shaft. This is the 38.125 mm (1.501 in.) outer diameter portion of the shaft. Its length is 72.6 mm (3.0 in.). Figure 12 shows the resulting FEA temperature distribution curve and the actual temperature measurement data versus axial shaft length. The uncertainty of the measured temperature is +/- 0.5°C. The curve from the FEA shows a temperature decline which is not linear along the shaft length. The experimentally measured axial temperature change shows that the test shaft surface temperature does not decrease as quickly as the FEA predicts for the location of the FB center. For example, the measured temperatures only decrease by one degree (from 188°C to 187°C) between the reference location and the FB center location. The temperature decrease is more drastic between the FB center location and near the edge of the heater due to the axial conduction to the solid portion of the test shaft from this latter location. The measured temperatures decrease by 11°C (from 187°C to 176°C) between the FB center location and the edge of the heater.

Test shaft radial expansion measurements are made without the test FB in place using an eddy current sensor (ECS) as discussed above. The ECS probe tip points towards the test shaft, again, at the location where the FB center rests during tests, approximately 32 mm from the open end of the shaft. The heater controller circuit is

---

[3] See Figure 12 for the location of temperature measurements.

sequentially set at the designated temperatures (55°C, 89°C, 122°C, 155°C, and 188°C), and the corresponding changes in ECS voltage are noted.
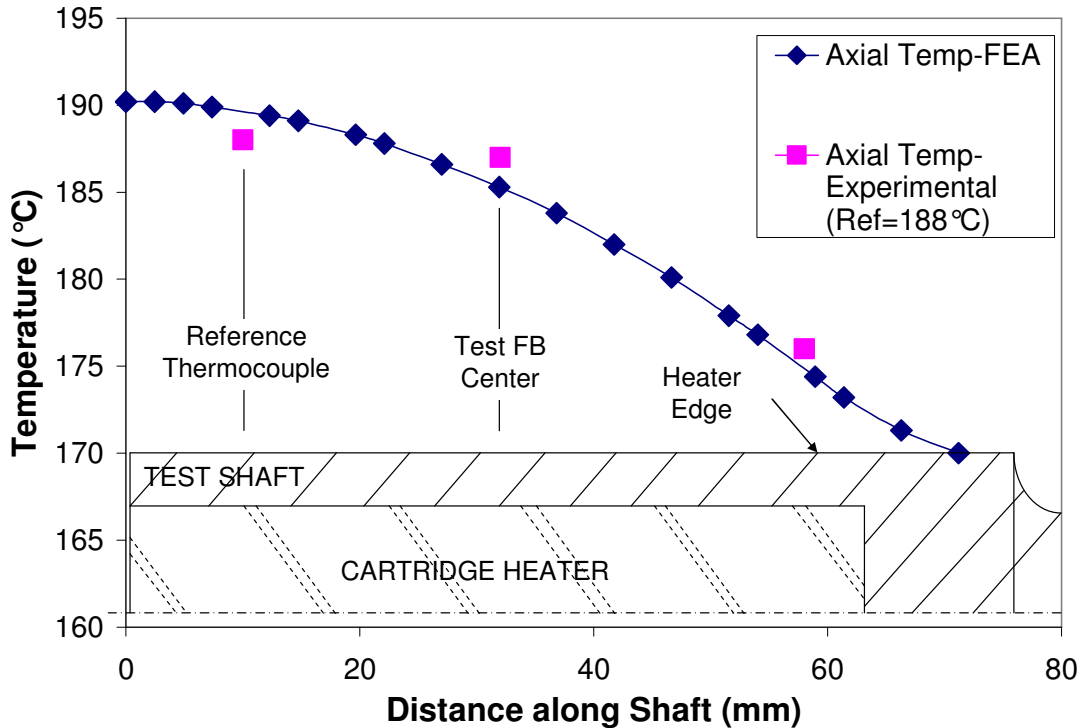
Figure 12 FEA temperature distribution results and measured shaft surface temperature at 10 mm (reference), 32 mm (FB center), and 58 mm (near cartridge heater end) showing the actual thermal gradient along the test shaft for shaft reference temperature T_S = 188°C.

Table 5 provides the resulting expansion measurement data and the CTE predictions using Equation (6) for the test shaft at a distance of 32 mm from the open end of the shaft. The resulting CTE from expansion measurements of the test shaft is α_S = 6.98 μm/m°C. The uncertainty associated with this calculation is $U_{\alpha,S}$ = 0.07 μm/m°C (as shown in Appendix B). Note that, from the above discussion of the axial temperature gradient along the test shaft, the expansion measurements and resulting CTE would essentially vary with measurement location along the test shaft. Thus, the shaft expansion measurements occur at the location where the FB center rests to minimize uncertainty as pertains to the clearance behavior between the shaft and bearing.

Table 5 Experimental thermal expansion data for the AISI 4140 steel test shaft coefficient of thermal expansion calculation (taken at 32 mm along the shaft length)

T_S (°C)	δT_S (°C)	$\delta T_{S,I}$ (°C)	ECS (Volts)	δR_S (μm)	$\delta R_{S,I}$ (μm)	CTE, α_S (μm/m°C)	
21	0	0	4.6551	0.000		Incremental	Total
55	34	34	4.6195	4.238	4.238	6.36	
89	68	34	4.577	9.298	5.060	7.59	
122	101	33	4.5393	13.786	4.488	6.94	6.98
155	134	33	4.4981	18.690	4.905	7.58	
188	167	33	4.4632	22.845	4.155	6.42	
				Average Value, $\alpha_{S,I}$		6.98	
				Standard Deviation		0.60	

A published CTE value for AISI 4140 steel is α_{4140} = 12.2 μm/m°C [24]. The discrepancy between the published value and the calculated value from radial expansion measurements is due to the non-uniform temperature distribution along the length of the test shaft. Since the cartridge heater does not heat the entire shaft to 188°C, for example, the whole shaft does not expand uniformly, or completely, at a rate of 12.2 μm/m°C. Instead, the cooler portion of the shaft restricts the expansion of the hotter portion.

AISI 304 Stainless Steel Bearing Housing

The FB housing is a thin-walled cylinder of uniform cross section with an outer diameter of 50.8 mm (2.0 in.), an inner diameter of 39.33952 mm (1.5488 in.), and an axial length of 38.1 mm (1.5 in.). Its uniform cross section and short axial length serve in simplifying the analysis of the thermal expansion of the FB housing. There is presumably no axial thermal gradient within the housing, only a radial gradient. A FE heat transfer analysis of the FB housing provides the temperature distribution through the bearing housing. A constant heat flux supplied at the inner surface of the housing until the outer surface reaches 155°C. Note, this is the measured FB housing surface temperature when the shaft temperature is at its maximum (T_S = 188°C). Once again, free convection (coefficient: h_{air} = 10 W/m²K) occurs at all outer surfaces of the housing

to the surrounding air at 21°C. Figure 13 shows the resulting FEA temperature distribution through the housing for the noted conditions. The results indicate that the inner surface is approximately 164°C for the given conditions, which is a radial thermal gradient of 9°C through the wall thickness.
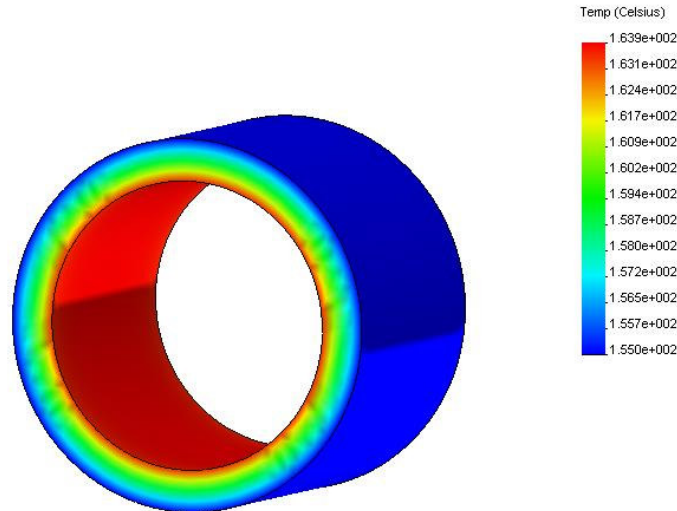
Figure 13 Thermal FEA analysis of FB housing showing a radial thermal gradient of 9°C through the 5.7277 mm wall thickness of the housing.

FB housing expansion measurements are made with the FB assembled onto the test shaft using the eddy current sensor (ECS) as described above. The ECS probe tip points to the center of the FB housing side wall and detects radial thermal expansion. The heater controller circuit is, again, sequentially set at the test temperatures (55°C, 89°C, 122°C, 155°C, and 188°C), and the corresponding changes in ECS voltage are noted. Table 6 provides the resulting expansion measurement data and CTE calculations for the stainless steel housing at its axial centerline. The resulting CTE from expansion measurements of the FB housing is α_B = 17.28 µm/m°C. The uncertainty associated with this calculation is $U_{\alpha,B}$ = 0.03 µm/m°C (as shown in Appendix B).

The published CTE value for AISI 304 stainless steel is α_{304} = 17.3 µm/m°C [24]. The percent error between the calculated CTE and the published value is approximately

0.1%; therefore, the measurement and CTE calculation methods are hereby verified as an acceptable process. This negligible amount of error also confirms that no significant temperature gradients exist along the length of the FB housing. That is, there is no significant distortion, or non-conformity, of the expected FB housing expansion, as in the case with the test shaft.

Table 6 Experimental thermal expansion data for the AISI 304 stainless steel FB housing coefficient of thermal expansion calculation

T_B (°C)	δT_B (°C)	$\delta T_{B,I}$ (°C)	ECS (Volts)	δR_B (µm)	$\delta R_{B,I}$ (µm)	CTE, α_B (µm/m°C)	
21	0	0	4.6551	0.000		Incremental	Total
47	26	26	4.6195	10.119	10.119	14.76	
73	52	26	4.577	21.025	10.906	16.84	
97	76	24	4.5393	31.784	10.759	17.29	17.28
123	102	26	4.4981	43.358	11.574	17.53	
147	126	24	4.4632	55.737	12.379	20.31	
				Average Value, $\alpha_{B,I}$		17.34	
				Standard Deviation		1.99	

Cr-Mb (Cr 5% - 9%) Bump and Top Foils

The thermal expansion of the foil material could neither be measured directly, nor could a published value for its coefficient of thermal expansion (CTE) be found. However, a web-based source [25] provides expansion calculations for lengths of pipe made of user-specified materials. The source allows the user to input an arbitrary initial pipe length and initial and final temperatures. The source outputs the change in pipe length due to thermal expansion. Finally, a CTE for the foil material (α_f) is calculated using the same relation as used for the test shaft and FB housing materials above.

An initial pipe length of the foil material ($L_{f,I}$) of 3.048 m (10 ft) at an initial temperature ($T_{f,I}$) of 21°C (70°F), or room temperature, are specified. The final temperature of the pipe is incrementally changed up to 204°C (400°F), to include the actual test temperature range, and the resulting change in length of the foil material (δL_f) is noted for each temperature change (δT_f). Table 7 provides the resulting expansion

calculations given by [25] and the incremental and total CTE calculations for the foil material. The average of the incremental CTE values is $\alpha_f = 11.1$ μm/m°C. The standard deviation (uncertainty) of the sample is $U_{\alpha,f} = 0.2$ μm/m°C.

Table 7 Theoretical thermal expansion data for the foil material coefficient of thermal expansion calculation [25]

T_f (°C)	δT_f (°C)	$\delta T_{f,I}$ (°C)	δL_f (μm)	$\delta L_{f,I}$ (μm)	CTE, α_f (μm/m°C)	
21	0	0	0	0	Incremental	Total
38	17	17	558.8	558.8	11.0	
49	28	11	914.4	355.6	10.8	
60	39	11	1295.4	381	10.9	
71	50	11	1651	355.6	10.8	
82	61	11	2032	381	10.9	
93	72	11	2387.6	355.6	10.8	
104	83	11	2768.6	381	10.9	
116	94	11	3175	406.4	11.0	11.4
127	106	11	3581.4	406.4	11.1	
138	117	11	3962.4	381	11.1	
149	128	11	4343.4	381	11.2	
160	139	11	4724.4	381	11.2	
171	150	11	5130.8	406.4	11.2	
182	161	11	5537.2	406.4	11.3	
193	172	11	5943.6	406.4	11.3	
204	183	11	6350	406.4	11.4	
			Average Value, $\alpha_{f,I}$		11.1	
			Standard Deviation		0.2	

One Dimensional Steady State Radial Conduction

The temperatures of the various surfaces must be determined to properly predict the radial expansions of the test components and subsequently predict the clearance between the test shaft and foil bearing, The following heat transfer analysis assuming one-dimensional steady state radial conduction with constant heat flux [26] provides these surface temperatures.

Figure 14 shows the composite cylindrical layers that compose the shaft and foil bearing assembly with the cartridge heater at the origin. The temperatures of interest are

those which cannot be directly measured during tests due to spatial limitations, namely the temperature at the inner wall of the shaft ($T_{S,i}$) and the temperature at the inner wall of the bearing housing ($T_{B,i}$). Also, a lumped conduction coefficient (k_f), derived in this analysis, indicates conduction through the top and bump foils.
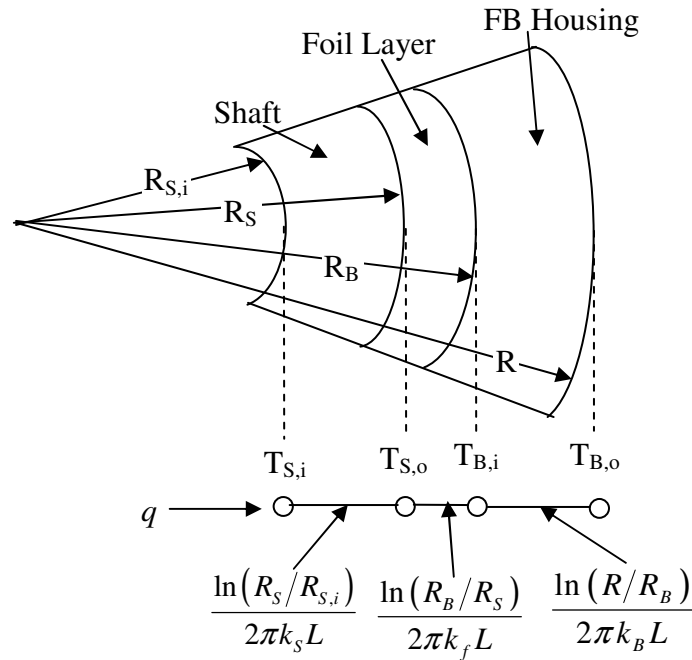
Figure 14 One-dimensional steady state conduction through a composite cylinder [26] simulating the test shaft, foil thickness layer (*Q*), and FB housing.

Radial conduction dictates the temperature gradient through each layer is logarithmic, instead of linear as in a plane wall [26]. The general equation for the heat transfer rate for each cylindrical layer is

$$q_r = \frac{2\pi L k \left(T_1 - T_2\right)}{\ln\left(\dfrac{r_2}{r_1}\right)}. \tag{7}$$

Solving for the constant radial heat flux yields

$$q_r'' = \frac{q_r}{2\pi L_h r_h} = \frac{k\left(T_1 - T_2\right)}{r_h \ln\left(\dfrac{r_2}{r_1}\right)} \,. \tag{8}$$

The definitions for the variables and constants (with values) are given in Table 8.

Table 8 Descriptions of the variables and constants used in Equation (8) with physical values of known parameters

Variable or Constant	Description and Value
k_B	Thermal conductivity of FB housing material [27], 16.2 W/mK
k_f	Thermal conductivity of foil layer, unknown W/mK
k_S	Thermal conductivity of test shaft material [27], 42.6 W/mK
L_h	Length of cartridge heater, 63.5 mm (2.5 in.)
q_r	Cartridge heater radial power, variable W
q_r''	Cartridge heater radial flux, variable W/m^2
r_h	Cartridge heater outer radius, 12.6746 mm (0.4990 in.)
R	FB housing outer radius, 25.4 mm (1.0 in.)
R_B	FB housing inner radius, 19.6698 mm (0.7744 in.)
R_S	Test shaft outer radius, 19.0627 mm (0.7505 in.)
$R_{S,i}$	Test shaft inner radius, 12.6873 mm (0.4995 in.)
$T_{B,i}$	Temperature at FB housing inner radius, unknown °C
$T_{B,o}$	Temperature at FB housing outer radius, measured °C
$T_{S,i}$	Temperature at test shaft inner radius, unknown °C
$T_{S,o}$	Temperature at test shaft outer radius, measured °C

The variable resistor used in the cartridge heater control circuit adjusts the output power of the heater to reduce overshoot of the target voltage for each target shaft temperature case. Table 9 provides the heater power and resultant flux for each test shaft surface temperature case. Equation (8) provides means to calculate the unknowns

using the given component radial dimensions, the respective material conduction coefficients, and the flux values for the respective test.

Table 9 Cartridge heater power converted to a constant heat flux and the measured test shaft and FB housing outer surface temperatures for each test condition

q (W)	q'' (W/m^2)	$T_{S,o}$ (°C)	$T_{B,o}$ (°C)
------	------	21	21
53	10,389	77	67
88	17,444	132	110
133	26,316	188	155

Table 10 shows the radial progression of resultant temperatures at the inner and outer (measured) surfaces of the shaft and bearing housing, along with the foil layer conduction coefficient. For example, for the case when the measured shaft surface temperature is $T_{S,o} = 77$°C, the calculated inner surface temperature is $T_{S,i} = 78$°C. The conduction coefficient through the lumped foil layer is $k_f = 0.521$ W/m*K, and the temperature at the inner diameter of the bearing housing is $T_{B,i} = 69$°C (with measured $T_{B,o} = 67$°C).

Table 10 Prediction of test shaft and FB housing inner surface temperatures and the foil layer conduction coefficient for each test condition

$T_{S,i}$ (°C)	$T_{S,o}$ (°C)	k_f (W/m*K)	$T_{B,i}$ (°C)	$T_{B,o}$ (°C)
78	77	0.521	69	67
134	132	0.374	113	110
191	188	0.377	160	155

It is clear from the data in Table 10 that the temperature difference at the inner and outer surfaces of each component is small. However, the temperature gradient across a solid body, the FB housing for example, is sufficient to cause different strain rates at the inner and outer surfaces. That is, using the measured (lower) outer surface temperature in the net temperature change calculation may underestimate the expansion of the hotter inner surface.

Change in Bearing Radial Clearance Due to Thermal Expansion

During tests at increasing temperatures, it is important to determine the behavior of the clearance between the shaft surface and the top foil. The test components comprise different materials with different coefficients of thermal expansion (CTEs). Table 11 provides the theoretical and experimental values of the CTEs for the corresponding test component. This section shows a method to predict the clearance change for the experimental temperature range.

Table 11 Predicted [24] and experimentally determined coefficient of thermal expansion for test components (uncertainty noted)

	Theoretical	Experimental	
Component (Material)	CTE (μm/m°C)	CTE (μm/m°C)	Uncertainty (μm/m°C)
Test Shaft (AISI 4140 Steel)	12.2	6.98	0.07
FB Housing (AISI 304 Stainless Steel)	17.3	17.28	0.03
Foils[4] (Cr-Mo Steels, Cr 5% - 9%)	------	11.1	0.2

The expansion of the outer radius of the shaft is given as

$$\delta R_S = \alpha_S R_{S,I} \Delta T_{S,o}$$
$$R'_S = R_{S,I} + \delta R_S \tag{9}$$

where R_S' is the final shaft radius after expansion. Recall from experiments measuring the axial temperature gradient along the length to the shaft, that the shaft temperature at the location of the FB center consistently evidenced a decrease of 1°C from the reference temperature (T_S). This trend provides an assumption in this radial clearance behavior analysis; therefore, the temperature at the outer surface of the test shaft ($T_{S,o}$) is reported as one degree less than the reference temperature. Thus, $\Delta T_{S,o}$ is the change of the shaft surface temperature at the bearing center.

The expansion of the inner radius of the bearing housing is given as

---

[4] The CTE of foil material is based on an average of 11 calculations performed above given temperature expansion data in [25]. The reported uncertainty is the standard deviation of the sample of averaged values.

$$\delta R_B = \alpha_B R_{(B,i)I} \Delta T_{B,i}$$
$$R_B' = R_{(B,i)I} + \delta R_B \tag{10}$$

where R_B' is the final inner radius of the bearing housing after expansion. The temperature at the inner surface of the FB housing ($T_{B,i}$) is determined using the one dimensional radial conduction with constant heat flux calculation, as shown above. The term $\Delta T_{B,i}$ is the change of the bearing housing inner surface temperature.

The expansion of the foil layer height is given as

$$\delta Q = (2\delta t) + h = \left[2(\alpha_f t_I \Delta T_Q) \right] + h$$
$$Q' = Q_I + \delta Q \tag{11}$$

where Q' is the final height of the foil layer after expansion. The temperature used for the expansion calculation of the foil layer height (T_Q) is determined as a weighted average of the surrounding surface temperatures, $T_{S,o}$ and $T_{B,i}$. Since the top foil directly contacts the hot shaft surface, and heat is then conducted to the bump foils, the temperature of the foil layer should receive more influence from the shaft surface temperature. Accordingly, a weighted average relation consistent with this rationale is $T_Q = 0.7(T_{S,o}) + 0.3(T_{B,i})$, and the term ΔT_Q provides the related temperature change.

Finally, combining Equations (4) and (9) through (11), the change in clearance between the test shaft and inner radius of the test bearing (R_I) with temperature becomes

$$C' = R_B' - (Q' + R_S'). \tag{12}$$

This analysis uses the radial clearance based on the actual geometry of the test components at room temperature. Thus, $C_g = 25.4$ μm is the basis of all calculations. Recall the clearance differential tracks any changes to the clearance with temperature. More specifically,

$$C' = C_g - \delta C' \Leftrightarrow \delta C' = C_g - C'. \tag{13}$$

Once again, a negative $\delta C'$ indicates an increase in clearance.

Table 12 shows the calculations of the changes in clearance and clearance differential with test shaft temperature (55°C, 89°C, 122°C, 155°C, and 188°C) for the experimental values of the component material CTEs. The results show that the radial

clearance increases by 22.3 µm at the maximum temperature. This indicates that the shaft, even at its higher temperature compared to the other components, expands approximately 22 µm less than the increase of the foil layer thickness coupled with the expansion of the FB housing inner radius.

It is of interest to determine the behavior of the radial clearance for the condition that the test shaft may actually be uniformly heated and allowed to expand at its theoretical rate (α_S = 12.2 µm/m°C). Table 12 also shows the changes in clearance and clearance differential with test shaft temperature (55°C, 89°C, 122°C, 155°C, and 188°C) based on theoretical CTE values for the test shaft and FB housing. The results show that the radial clearance increases by 5.7 µm at the maximum temperature. The shaft radius expands 16.6 µm more in this theoretical case than in the experimentally measured case.

Table 12 Change in clearance and clearance differential as a function of shaft temperature based on experimentally derived (α_S = 6.98 µm/m°C, α_B = 17.28 µm/m°C, α_f = 11.1 µm/m°C) and published (α_S = 12.2 µm/m°C, α_B = 17.3 µm/m°C, α_f = 11.1 µm/m°C) coefficients of thermal expansion for the test components

				Experimental CTEs		Theoretical CTEs	
T_S (°C)	$T_{S,o}$ at Bearing Center (°C)	$T_{B,i}$ (°C)	T_Q (°C)	C' (µm)	$\delta C'$ (µm)	C' (µm)	$\delta C'$ (µm)
20	20	20	20	25.4	0.0	25.4	0.0
55	54	48	52.2	30.3	-4.9	26.9	-1.5
89	88	75	84.1	34.9	-9.5	28.1	-2.7
122	121	100	114.7	38.9	-13.5	28.9	-3.5
155	154	127	145.9	43.6	-18.2	30.3	-4.9
188	187	152	176.5	47.7	-22.3	31.1	-5.7

* Initial dimensions: $R_{S,i}$ = 19.0627 mm, $R_{B,i}$ = 19.6723 mm, Q_i = 0.5842 mm

The results of the expansion of components analysis show that the inner diameter bearing housing expands more than the outer diameter of the shaft and the foil layer thickness combined. Therefore, the clearance increases over the temperature range. The reader must keep in mind that this test setup is rather unusual. That is, in practice the

bearing will be constrained on its outer diameter, and thus the FB bearing inner diameter expansion will be different from that stated here.

Figure 15 shows the predicted increase of radial clearance over the range of test shaft temperature due to the experimentally determined CTE (6.98 μm/m°C) and the theoretical CTE (12.2 μm/m°C). The clearance increases from 25.4 μm at room temperature to 47.7 μm and 31.1 μm at the maximum shaft temperature for the two CTE values, respectively. Recall that the bump structure does not become mechanically preloaded until the radial clearance becomes $C < 0$ mm.
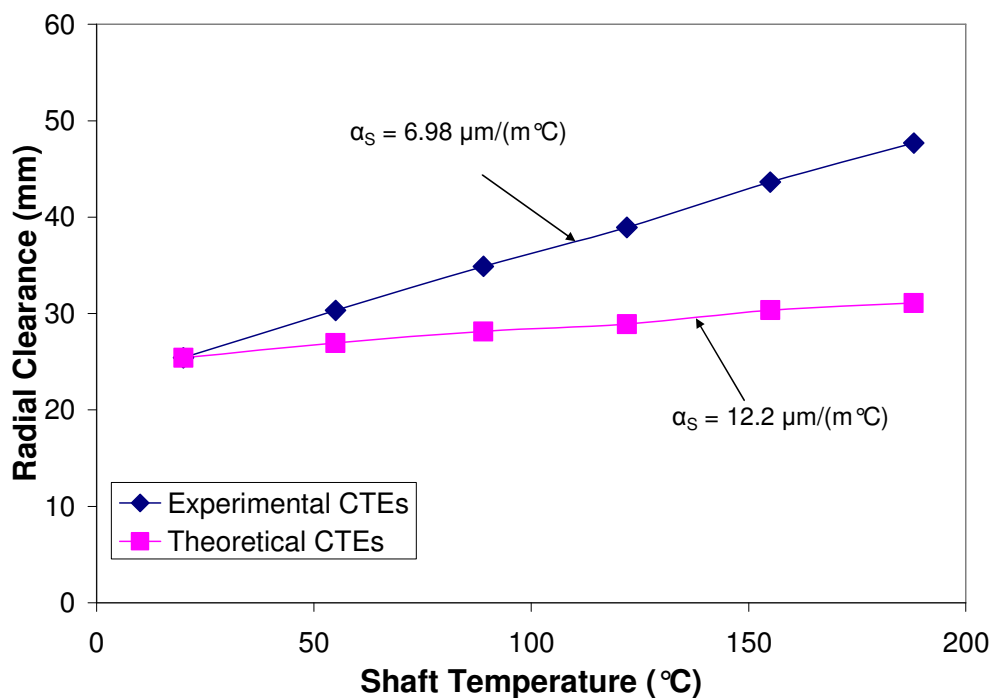
Figure 15 Estimated radial clearance between 38.125 mm diameter shaft and FB as a function of measured T_S for the experimentally derived and published CTE values for the test components with C_{nom} = 25.4 μm (the test shaft CTEs are noted near its respective curve).

Figure 16 shows the clearance differential as a function of the change in shaft surface temperature for the experimental and theoretical CTE values for the test components. The difference between the measured (α_S = 6.98 μm/m°C) and theoretical (α_S = 12.2 μm/m°C) CTE values for the test shaft causes the discrepancy in the predicted radial clearance behavior. Again, no mechanical preload of the bump structure occurs

until the clearance differential becomes greater than the nominal clearance; i.e., $\delta C > C_{nom} = 25.4$ µm. However, for the maximum temperature conditions, the clearance differential is $\delta C = -22.3$ µm, and the actual clearance is $C_{act} = C_{nom} - \delta C = 47.4$ µm, which is nearly $2*C_{nom}$.
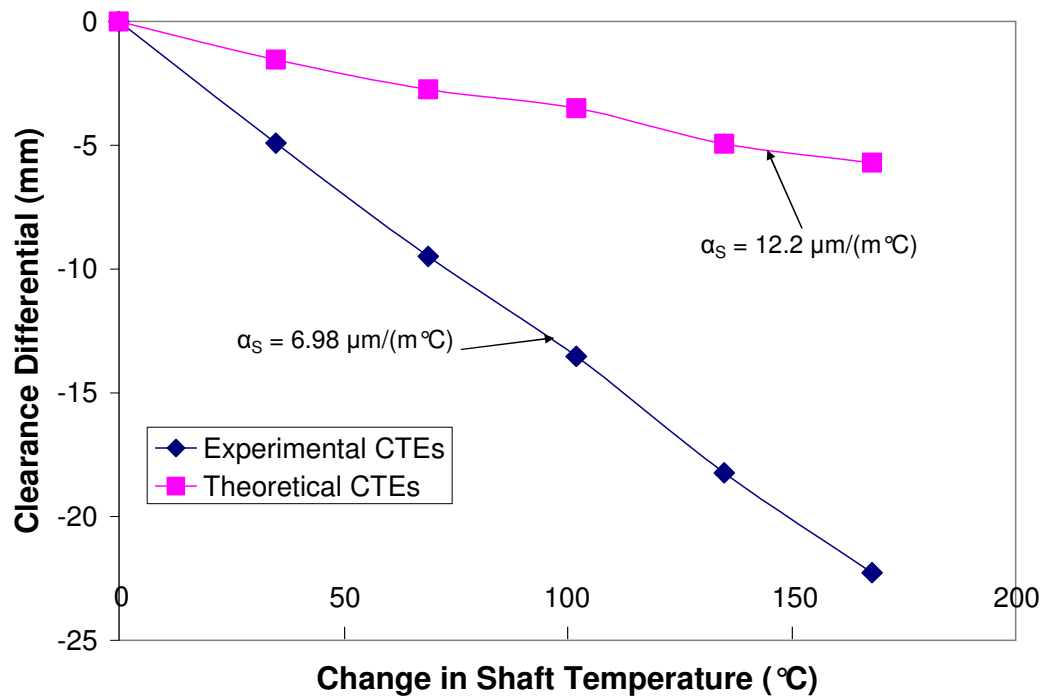
Figure 16 Clearance differential versus change in shaft temperature derived from the published and experimentally derived CTE values showing increasing clearance.

V EXPERIMENTALLY DETERMINED FOIL BEARING STRUCTURAL STIFFNESS

The FB undergoes static load tests while varying the shaft temperature. These tests provide the bearing deflection as a function of applied static load, from which the FB stiffness is determined. These tests aim to identify FB stiffness as a function of bearing deflection and its dependence on shaft temperature. The bearing orientations indicate the load application direction measured from the top foil spot weld towards the free end of the foil. Test temperatures indicate the shaft surface temperature during tests. Note that testing for the 38.075 mm shaft only occurs at room temperature (22°C).

Experimental Procedure

Table 13 provides the conditions of the static load tests and indicates that tests involve two shafts of differing diameters. The 38.075 mm shaft induces more clearance of the compliant structure than the larger 38.125 mm shaft. Note that tests for the smaller shaft diameter were conducted only at room temperature.

Table 13 Static load test parameters

Shaft Diameter, mm [in]	38.075 [1.499]	38.125 [1.501]
Nominal Radial Clearance (C_{nom}), μm [mil]	48.3 [1.9]	22.9 [0.9]
Uncertainty in C_{nom}, μm [mil]	3.2 [0.13]	
Bearing Orientation	45°, 90°, 225°, 270°	
Shaft Temperature	22°C, 89°C, 188°C	
Static Load Range, N [lb]	0-133.44 [0-30]	

Thermocouples provide temperature measurements of the shaft and bearing housing surfaces. The cartridge heater inside the shaft, monitored and controlled by an external circuit, provides a controllable heat source. During tests, the temperature in Table 13 denotes the measured shaft temperature. The bearing housing surface never achieves the same temperature of the shaft surface for a given test condition. Table 2 shows the bearing surface temperature experienced during tests.

For room temperature tests, the tool holder moves the dynamometer into contact with the bearing housing. The bearing moves from its resting position ($x = 0$ μm) as the load is increased incrementally throughout the load range. The voltage measurement from the eddy current sensor provides FB deflection as a function of static load. This procedure performed in reverse supplies information during unloading. Figure 17 and Figure 18 show the load application directions with respect to the spot weld location for the given bearing orientations.

Tests at higher shaft temperatures follow the above procedure, with special consideration to the resulting bearing housing expansion with temperature increase. That is, the outer diameter of the bearing increases as its temperature increases. Accordingly, after tests at a certain temperature, the bearing is manually returned to its initial location, or starting eddy current sensor voltage, before setting the temperature controller to the next shaft temperature.
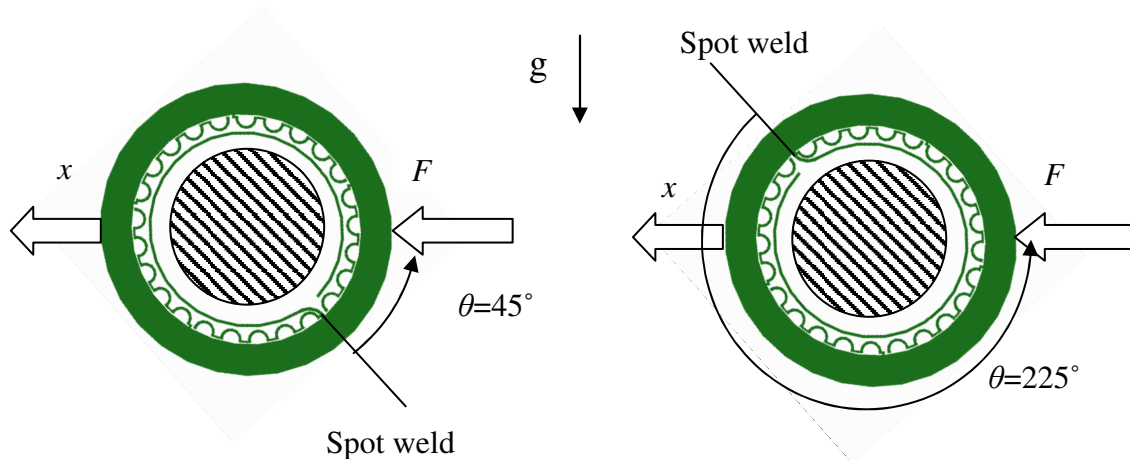
Figure 17   Load application and displacement directions for 45° and 225° bearing orientations.
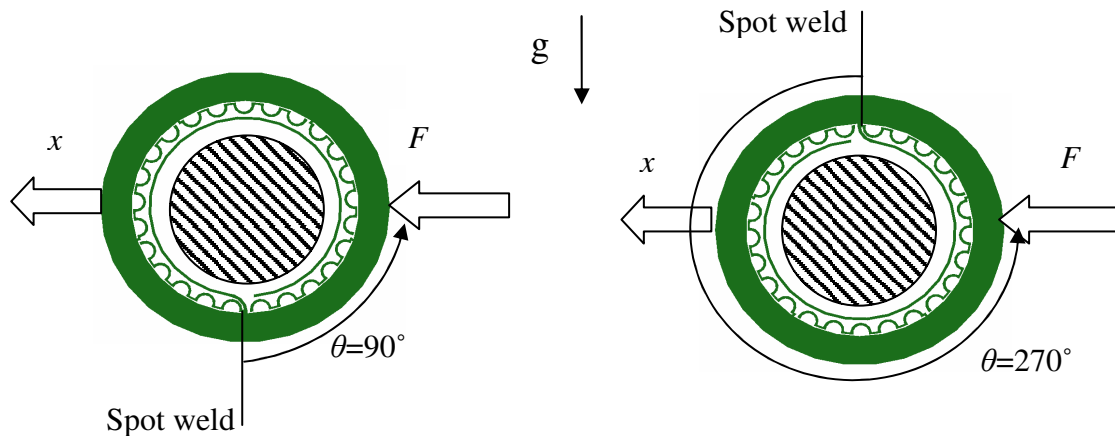
Figure 18 Load application and displacement directions for 90° and 270° bearing orientations.

Experimental Results

The experimental data are presented herein. Figure 19 shows the loading and unloading FB deflection versus load curves for the 45° bearing orientation on the 38.125 mm shaft with $T_S = 22°C$ (ambient conditions). Note the loading and unloading curves follow different paths that form a loop. The loop, which is common to all tests, indicates hysteresis due to friction between contacting surfaces during the unloading process. When the bearing is fully unloaded, the amount of remaining deflection may also indicate an amount of clearance between the shaft and the elastic foils before loading. Three trials for each condition were conducted and show good repeatability.

The FB deflection versus load curves for the 45° (90°) and 225° (270°) bearing orientations combine to make a single push-pull curve. Positive loads (push) correspond to loading at the 45° (90°) orientation, while negative loads (pull) correspond to loading at the 225° (270°) orientation, hereafter, referred to as the 45°-225° orientation and the 90°-270° orientation, respectively.
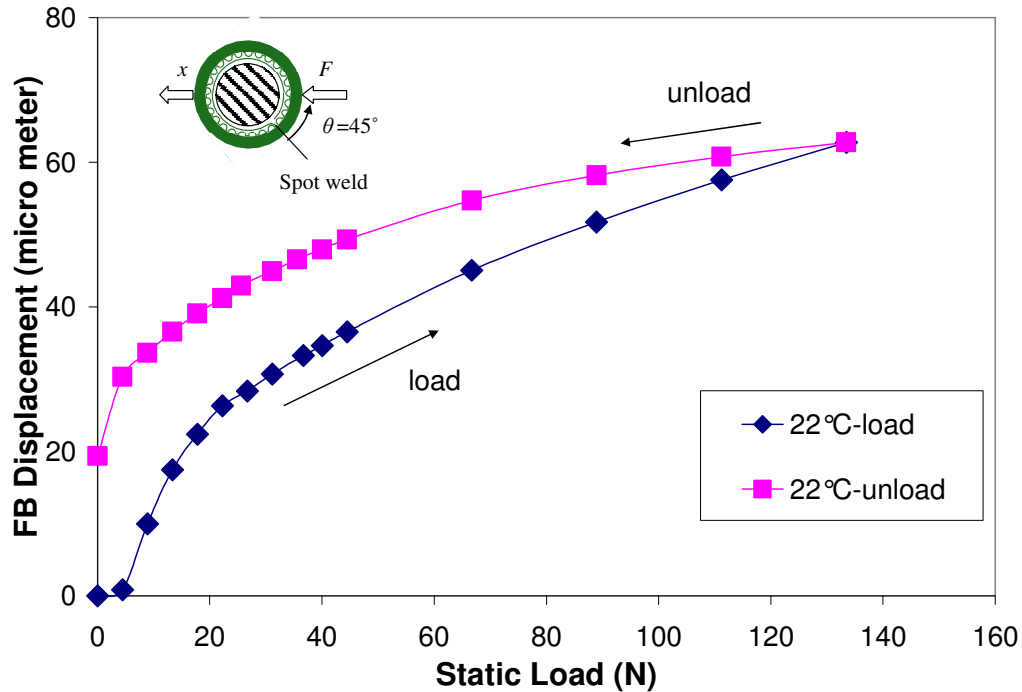
Figure 19 Loading and unloading displacement versus load data for the 45° bearing orientation showing hysteresis (38.125 mm shaft, C_{nom} = 22.9 μm, T_S = 22 °C).

Figure 20 shows the push-pull curves[5] for the two orientations for the 38.075 mm shaft. This figure makes clear the difference in stiffness bearing orientation as found in [17]. That is, under the same load, the 90°-270° curve shows more deflection than the 45°-225° curve, which indicates less stiffness. The actual stiffness estimation and data reduction method appears in the following section.

Figure 21 and Figure 22 show the change in FB deflection for the 45°-225° and 90°-270° bearing orientations, respectively, for the 38.125 mm shaft at increasing temperatures. All of the push-pull curves increase in total deflection with increasing temperature. Figure 22 shows a peculiar FB deflection behavior along the 270° direction. Unlike the significant increases with temperature seen for other bearing orientations, FB deflection appears to converge to a limit.

---

[5] Push-pull curves show the measurements corresponding to the loading curves for each bearing orientation (no unloading, i.e., hysteresis not shown in any of the results).
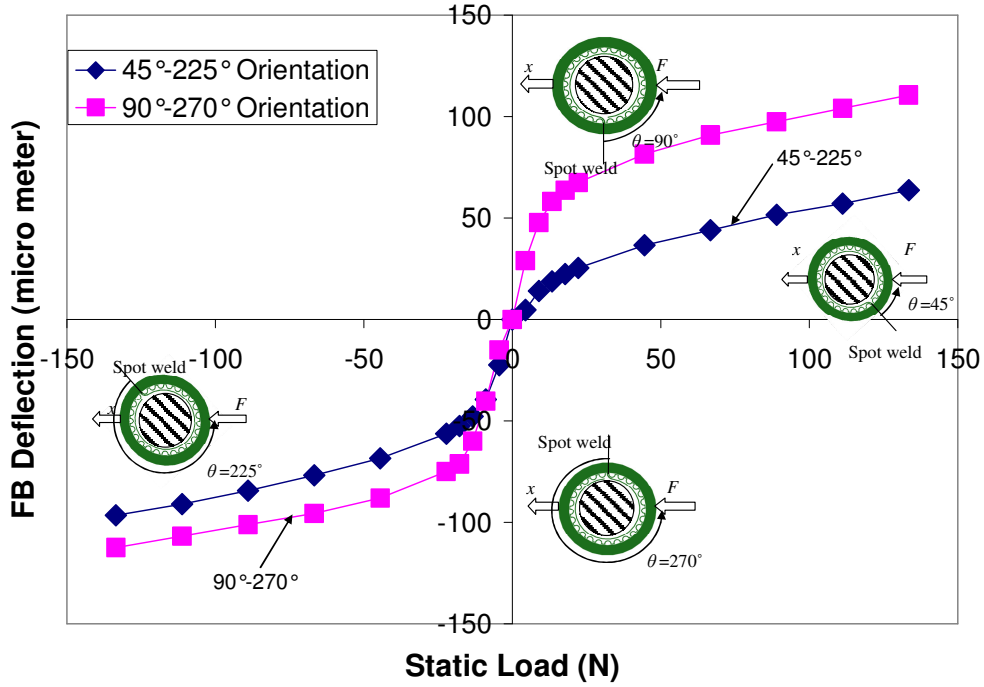
Figure 20 FB deflection versus load data 45°-225° and 90°-270° bearing orientation (38.075 mm shaft, C_{nom} = 48.3 μm, T_S = 22℃).
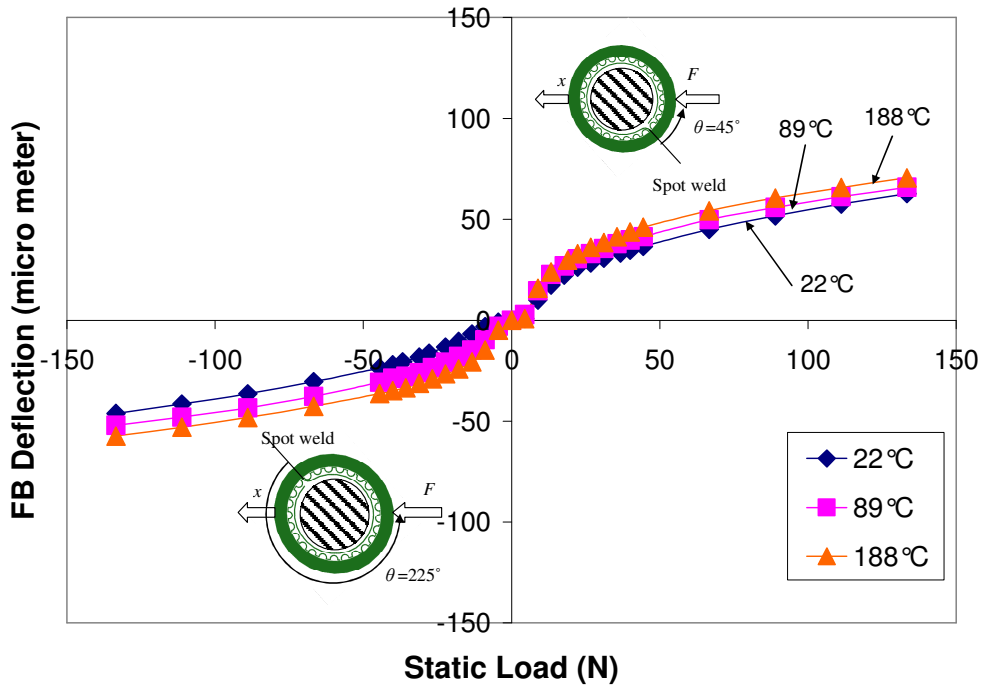
Figure 21 FB deflection versus applied load data for the 45°-225° bearing orientation at three shaft temperatures (38.125 mm shaft, C_{nom} = 22.9 μm).
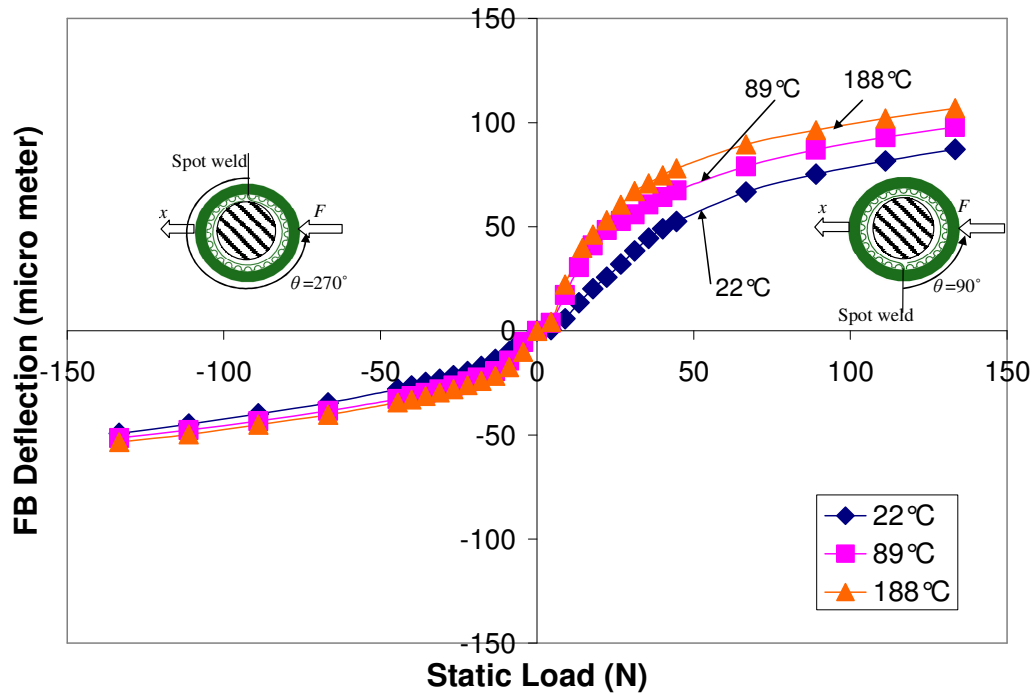
Figure 22 FB deflection versus applied load data for the 90°-270° bearing orientation with shaft at three temperatures (38.125 mm shaft, C_{nom} = 22.9 µm).

Table 14 presents the largest FB static deflections for the same load (133.4 N) applied along the respective directions. Note the larger deflections for both bearing orientations for the smaller shaft, compared to the larger shaft. Indeed, the FB deflection increases with temperature for the 38.125 mm shaft.

Table 14 Summary of FB deflection interval experienced for +/-133.4 N for each shaft and test temperature.

		FB Deflection Interval (µm)	
Test Shaft	Shaft Temperature	45°-225° Orientation	90°-270° Orientation
38.075 mm	22°C	[-96.5 , 63.7]	[-112.5 , 110.6]
	22°C	[-46.2 , 62.8]	[-49.2 , 87.2]
38.125 mm	89°C	[-52.1 , 65.9]	[-51.4 , 97.9]
	188°C	[-57.4 , 70.6]	[-53.4 , 106.9]

Data Reduction to Determine Foil Bearing Structural Stiffness

This portion of the analysis estimates the FB stiffness for increasing shaft temperature using the load versus FB deflection curves for the 45°-225° and 90°-270° bearing orientations. Each experimental FB deflection versus static load curve from the previous section is converted to a load versus FB deflection curves for the data reduction. Figure 23 shows the measured load versus FB deflection curve for the 45°-225° bearing orientation for the 38.125 mm shaft at $T_S = 22$°C. The boxed area shows a discontinuous portion of the curve for low loads.
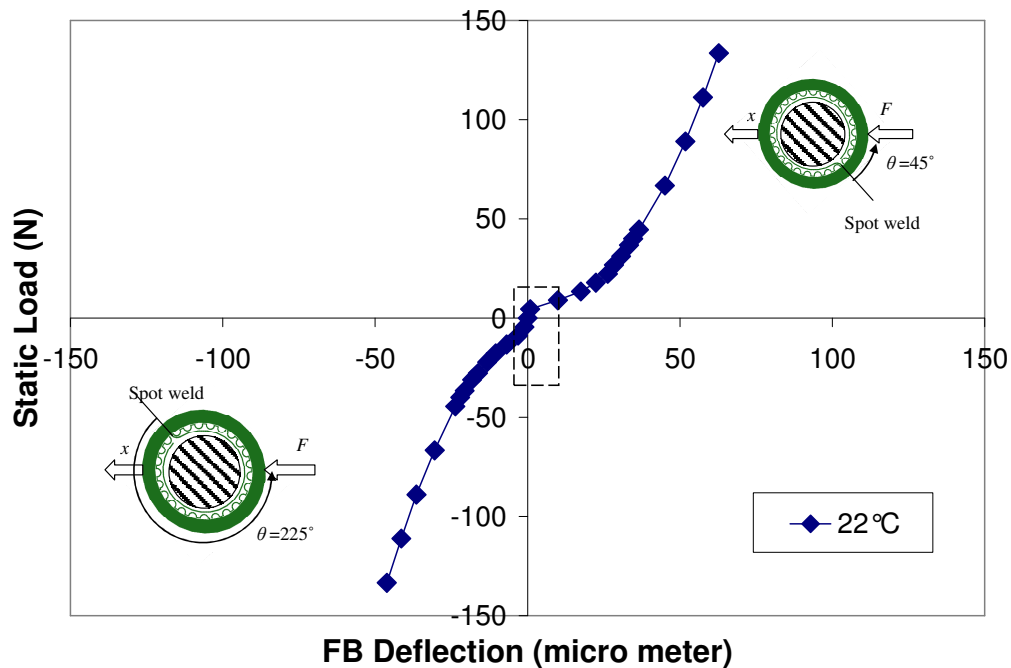
Figure 23 Load versus FB deflection data for the 45°-225° bearing orientation with shaft at $T_S = 22$°C (38.125 mm shaft, $C_{nom} = 22.9$ µm).

Figure 24 shows this boxed portion of the load versus deflection curve magnified for the same test case shown in Figure 23. Note the small deflections for the +/- 4.4 N (1 lb) load along each direction. This result contradicts the expected behavior of movement through a radial clearance between the shaft and the top foil. For example, the FB stiffness along the 45° (positive) direction, given as the slope of the line from the origin

to the first data point (0.82 μm, 4.4 N), is 5.4 MN/m. It is obvious that this high stiffness magnitude cannot be caused by the lightly loaded bumps or the radial clearance. Therefore, another mechanism must explain this behavior. Since the FB weight rests on the top of the shaft, the top foil rests on the shaft when there is no external load acting on the bearing. As an external load is applied to the FB, the sliding friction between the top foil and the shaft impedes bearing motion before the radial clearance in the load direction is traversed. Once the bumps on the compressed side of the bearing become progressively activated, there is no longer sliding between the shaft and the top foil. There exists only increasing compression of the bump structure. The subsequent decreased stiffness for the $F = 8.9$ N data point to 0.49 MN/m indicates a transition from sliding contact between the shaft and top foil to the compression of the bump structure by the shaft.
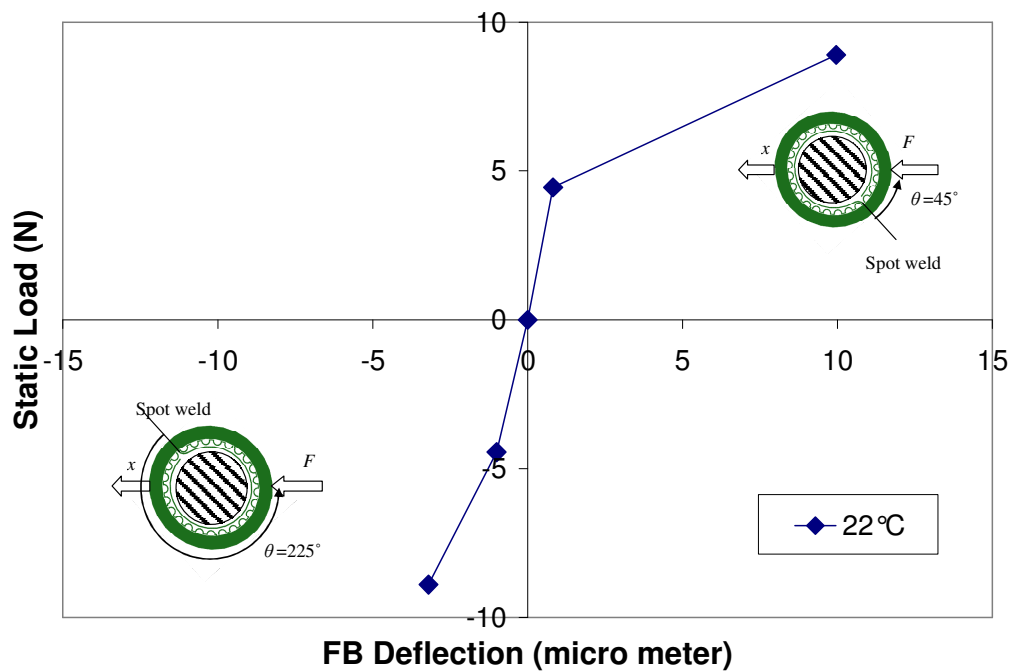
Figure 24 FB deflection for +/-8.9 N for the 45°-225° bearing orientation with shaft temperature at T_S = 22°C (38.125 mm shaft, C_{nom} = 22.9 μm).

The data reduction scheme separates the experimental load versus FB deflection curves into three regions: deflection data corresponding to loads $F \leq$-8.9 N, $F \geq$8.9 N, and the load interval -8.9 N$\leq$$F$$\leq$8.9 N. The data within the load interval -8.9 N$<$$F$$<$8.9 N is subject to sliding friction and is not repeatable from test to test. This apparent friction increases the stiffness estimation uncertainty at low loads. Therefore, this small load interval is disregarded for the current analysis due to lack of repeatability. The outer regions of a load versus FB deflection data are fitted with a cubic polynomial of the form $F(x)=a+bx+cx^3$, fully described in the next section. The bearing stiffness (K) is the derivative of the force curve with respect to displacement.

Cubic Polynomial Curve Fit of Force versus Deflection Measurements

Figure 25 through Figure 27 show the measured load versus FB deflection data used for estimation of the bearing static structural stiffness. Figure 25 shows the measured load versus FB deflection data for the 45°-225° and 90°-270° bearing orientations for the 38.075 mm test shaft at room temperature. Figure 26 shows the load versus FB deflection data for the 45°-225° bearing orientation with the 38.125 mm shaft at increasing shaft temperatures. Figure 27 shows the load versus FB deflection data for the 90°-270° bearing orientation with the 38.125 mm shaft at increasing shaft temperatures. The previously mentioned deflection limit in the 270° direction is evidenced for the 38.125 mm shaft.
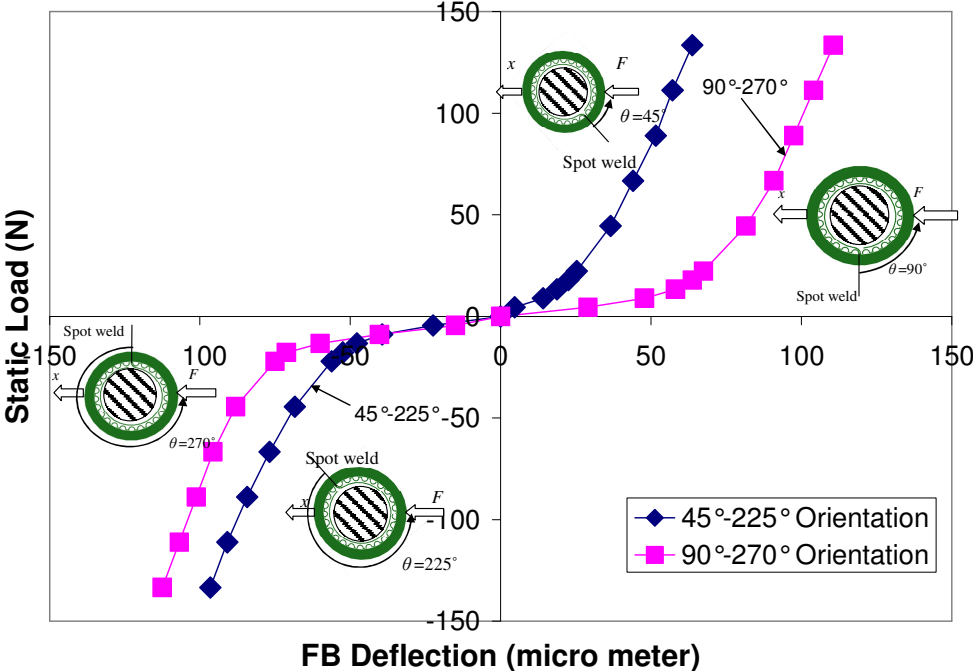
Figure 25 Load versus FB deflection data for the 45°-225° and 90°-270° bearing orientations (38.075 mm shaft, C_{nom} = 48.3 μm, T_S= 22°C).
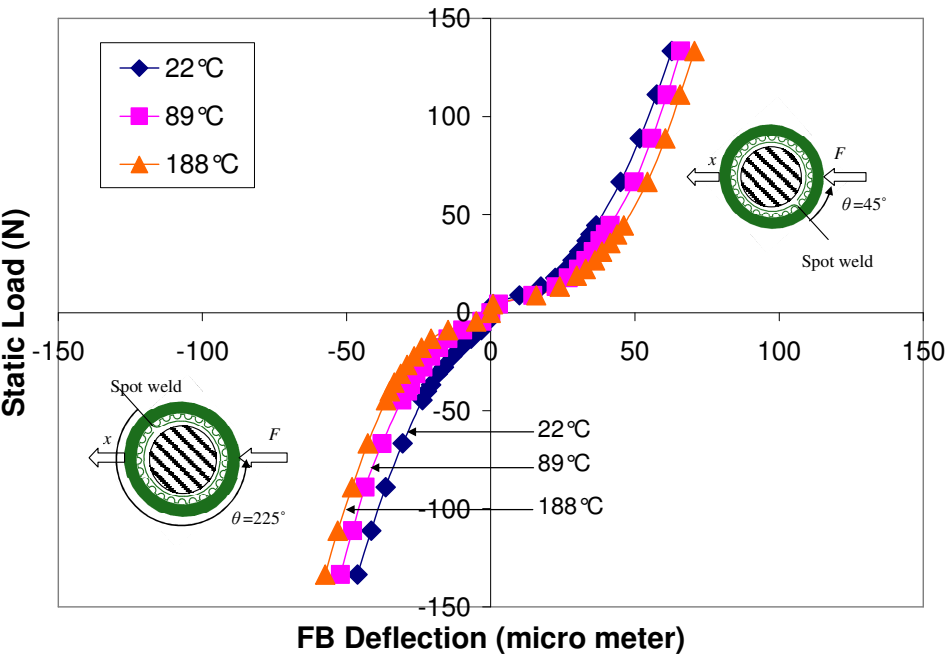
Figure 26 Load versus FB deflection data for the 45°-225° bearing orientation for increasing shaft temperatures (38.125 mm shaft, C_{nom} = 22.9 μm).
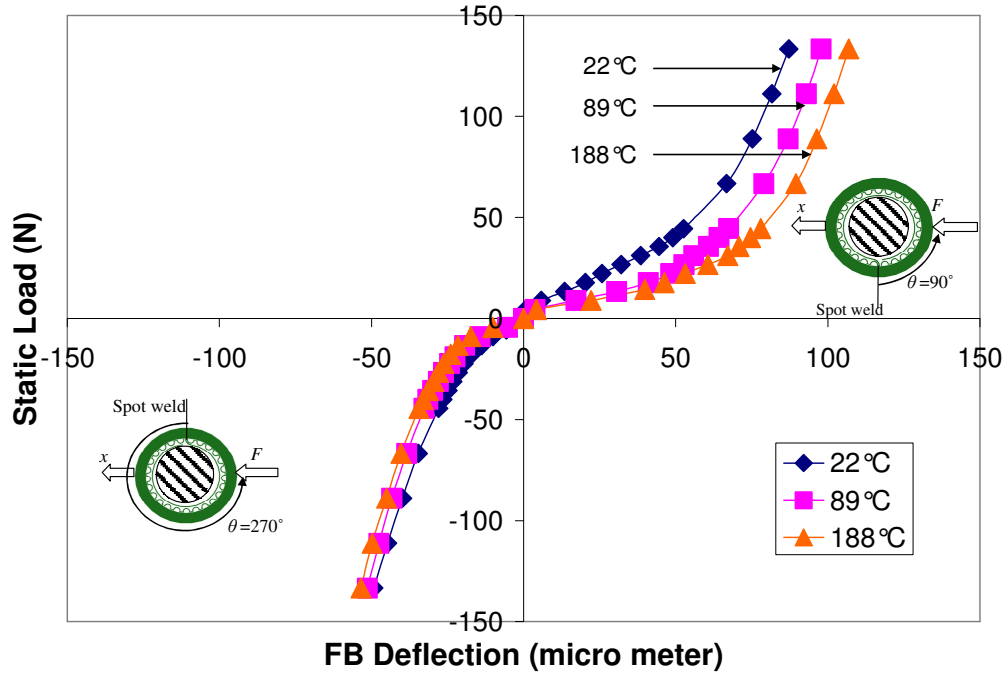
Figure 27 Load versus FB deflection data for the 90°-270° bearing orientation for increasing shaft temperatures (38.125 mm shaft, C_{nom} = 22.9 µm).

Computational software divides each load versus FB deflection data into the three segments noted. x_a denotes the FB deflections caused by loads $F \leq$ -8.9 N, while x_b is the deflection resulting from loads $F \geq 8.9$ N.

For $x \leq x_a$,

$$F(x) = -8.9N + A_{n1}(x - x_a) + A_{n2}(x - x_a)^3 \tag{14}$$

where A_n are the coefficients for the pull (negative) displacement cases. For $x \geq x_b$,

$$F(x) = 8.9N + A_{p1}(x - x_b) + A_{p2}(x - x_b)^3 \tag{15}$$

where A_p are the coefficients for the push (positive) displacement cases. For the case that $x_a \leq x \leq x_b$, no analysis is conducted because the lack of repeatability.

By definition, the stiffness is $K = \partial F / \partial x$. More specifically, for $x \leq x_a$,

$$K(x) = A_{n1} + 3A_{n2}(x - x_a)^2 \tag{16}$$

And if $x \geq x_b$

$$K(x) = A_{p1} + 3A_{p2}(x - x_b)^2 \tag{17}$$

Figure 28 shows the experimental load versus deflection data and the cubic polynomial curve fits for the 45°-225° bearing orientation with the shaft at ambient temperature. Equations (14) and (15) evidence a goodness of fit $R^2 = 0.998$ or better for every force versus deflection curve in the analysis. Note the circled region in the figure, which is the ignored interval corresponding to deflection resulting from loads -8.9 N $\leq F$ $\leq$ 8.9 N.

Figure 29 shows the derived stiffness versus FB deflection for the two regions a and b from the test case shown in Figure 28. Note the differing values of stiffness at the deflection values corresponding to +/-8.9 N. The ranges of stiffness values correspond to the deflection intervals. For example, for the deflection interval along the 225° direction [-46.2 μm, -3.2 μm] the stiffness range is [1.39 MN/m, 6.10 MN/m]. For clarity, the deflection interval along the 45° direction [10.0 μm, 62.8 μm] has the stiffness range [0.89 MN/m, 5.46 MN/m].
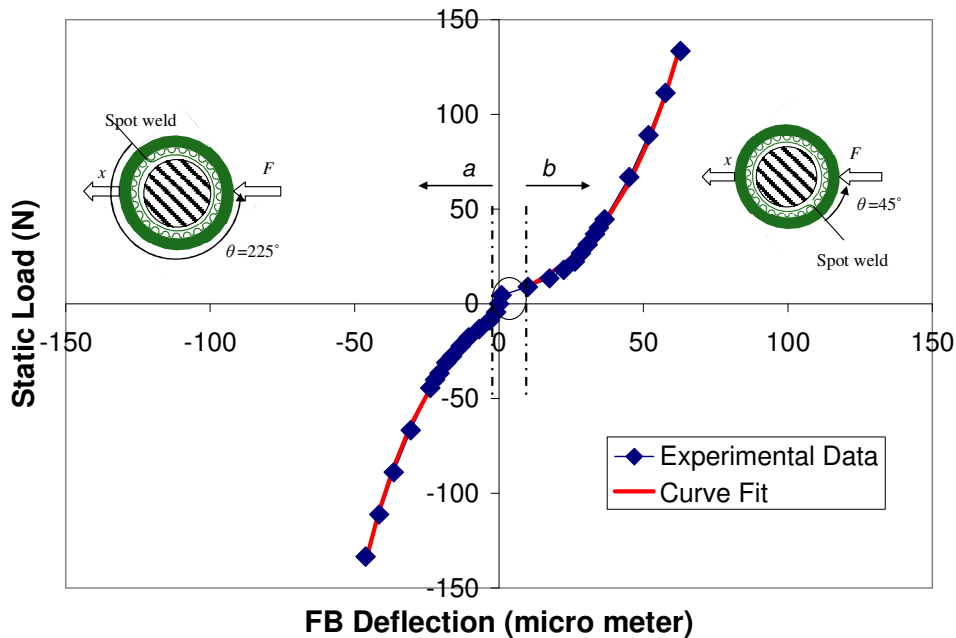
Figure 28 Curve fitted portions of the experimental load versus deflection data for the 45°-225° bearing orientation at 22℃ (38.125 mm shaft, C_{nom} = 22.9 μm). The unidentified portion remains within the noted circle.
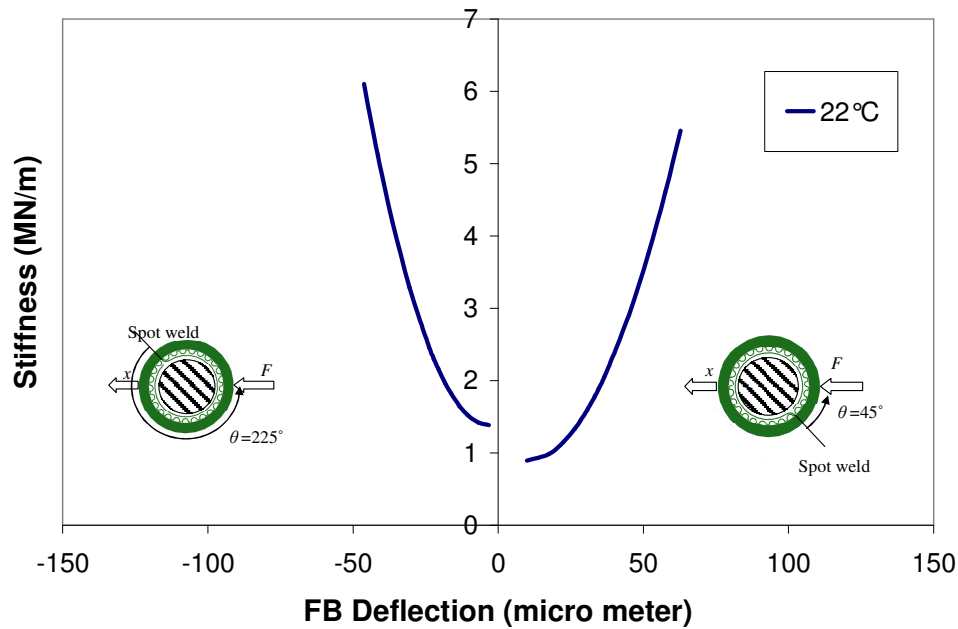
Figure 29 Derived stiffness from load versus deflection curve fit versus FB deflection for the 45°-225° bearing orientation at T_S = 22 °C (38.125 mm shaft, C_{nom} = 22.9 μm).

Each experimental load versus FB deflection data set is fitted with a cubic polynomial as described above, and the stiffness estimation is performed for all the noted cases and grouped for comparison as follows. Figure 30 shows the stiffness as a function of FB deflection for the smaller 38.075 mm shaft at room temperature for the two bearing orientations. The stiffness for the 90°-270° bearing orientation is indeed less than that of the 45°-225° bearing orientation, as inferred from observing the deflection magnitudes from the experiment. Note the stiffness versus FB deflection data form a wider curve for the 90°-270° bearing orientation than for the 45°-225° bearing orientation.
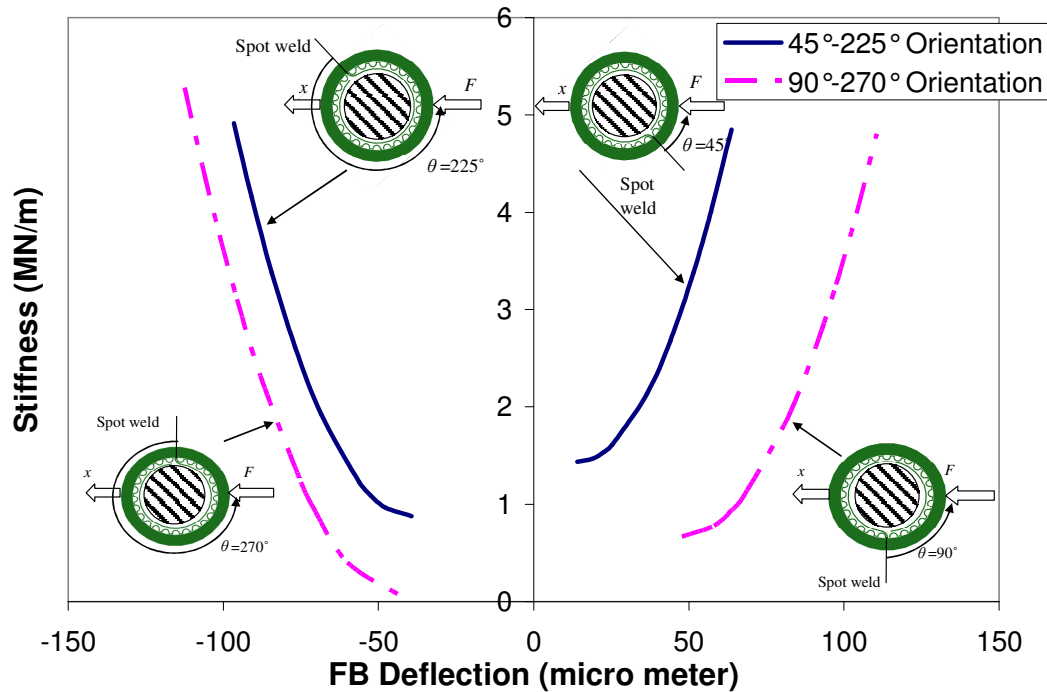
Figure 30 Stiffness derived from load versus deflection curve fit for the 45°-225° and 90°-270° bearing orientations with shaft at T_S = 22°C (38.075 mm shaft, C_{nom} = 48.3 μm).

Figure 31 and Figure 32 show the resulting stiffness versus FB deflection curves with the 38.125 mm shaft at increasing temperatures for the 45°-225° and 90°-270° bearing orientations, respectively. Indeed, the stiffness for a certain FB deflection decreases for increasing shaft temperatures. The experimental FB stiffness is noted at 40 μm FB deflection along each load direction for each shaft temperature. Experiments show that, for the shaft temperature change from T_S = 22°C to T_S = 188°C, the FB stiffness decreases 32% for the 45° direction and 35% for the 225° direction. In Figure 32, note the markedly different stiffness behavior in the pull direction for the 90°-270° bearing orientation at the aforementioned limit (as seen in Figure 27). That is, the FB stiffness is higher in the 270° direction than it is in the 90° direction. Experiments show that the FB stiffness decreases 70% for the 90° direction and 15% for the 270° direction for the same change in shaft temperature.
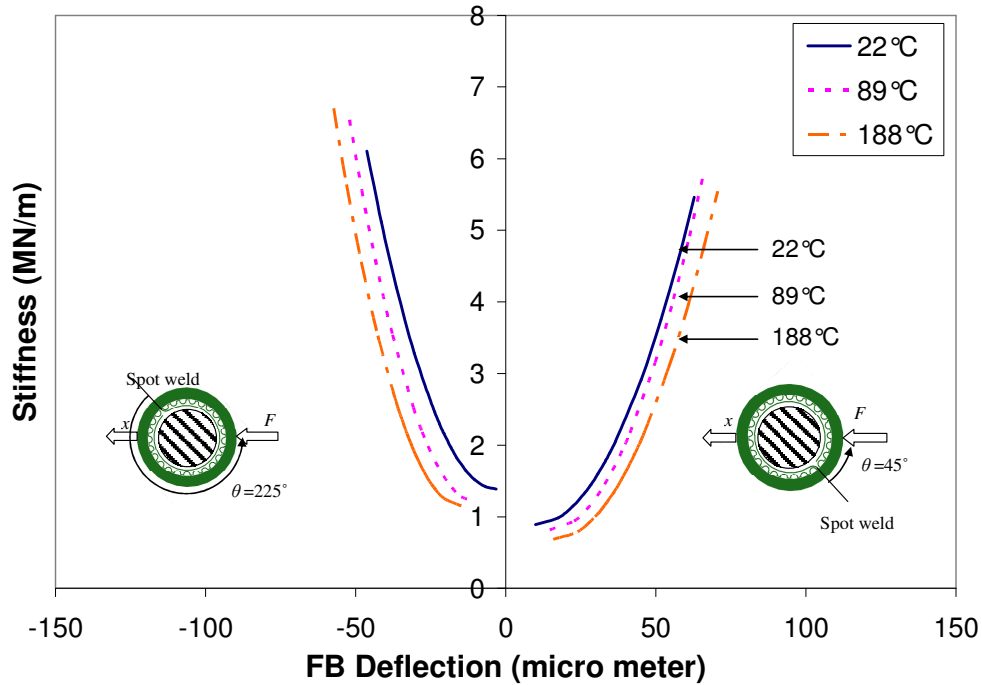
Figure 31 Stiffness derived from load versus deflection curve fit for the 45°-225° bearing orientation at increasing shaft temperatures (38.125 mm shaft, C_g varies with T_S).
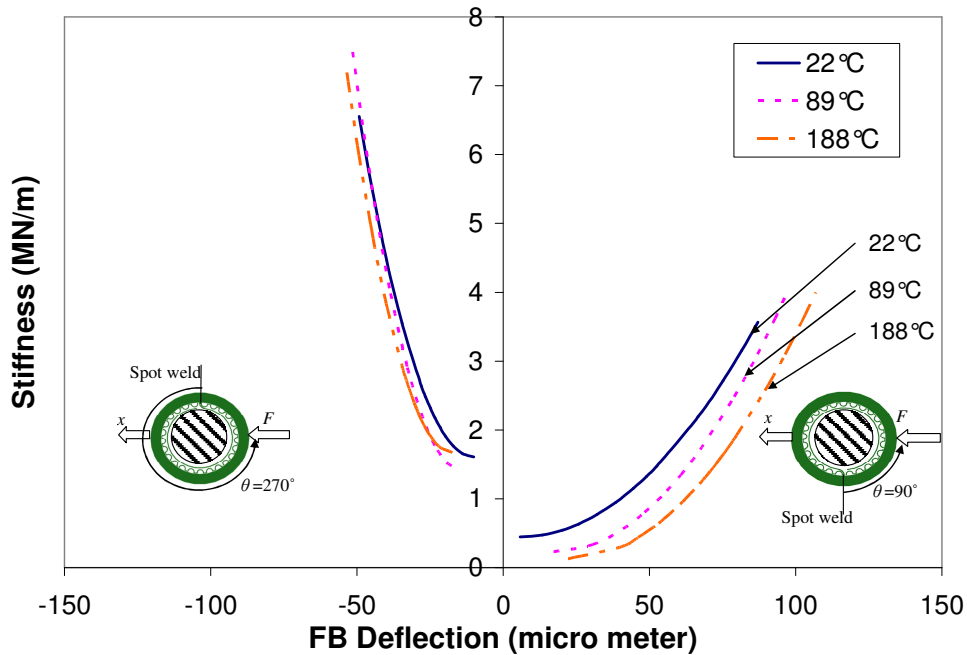
Figure 32 Stiffness derived from load versus deflection curve fit for the 90°-270° bearing orientation at three shaft temperatures (38.125 mm shaft, C_g varies with T_S), distinct behavior in the pull (negative) direction.

Appendix D gives a summary of the curve fit coefficients for Equations (14) and (15). Also, the goodness of fit coefficients for the curve fits to the experimental data, R^2, are also included.

Table 15 presents a summary of the stiffness range for each FB deflection interval. Note for the 38.125 mm shaft, as temperature increases for both bearing orientations, the bearing deflection increases. This indicates a reduction in stiffness with temperature. For the 38.075 mm shaft, the larger deflection interval indicates reduced stiffness for the 90°-270° bearing orientation as compared to the 45°-225° bearing orientation. Also, for the 38.075 mm shaft, note the large deflection values corresponding to +/-8.9 N loads, which indicate a larger clearance between bump foils than for the larger shaft.

Table 15 Summary of derived stiffnesses for corresponding FB deflection intervals for the 45°-225° and 90°-270° bearing orientations with the 38.075 mm shaft at room temperature and the 38.125 mm shaft at increasing temperatures

D_S (mm)	Bearing Orientation	T_S (°C)	Pull		Push	
			x (μm)	K (MN/m)	x (μm)	K (MN/m)
38.075	45°-225°	22	[-96.5 , -39.4]	[0.88 , 4.92]	[14.1 , 63.7]	[1.44 , 4.85]
	90°-270°	22	[-112.5 , -40.3]	[0.01 , 5.28]	[47.8 , 110.6]	[0.67 , 4.81]
38.125	45°-225°	22	[-46.2 , -3.2]	[1.39 , 6.10]	[10.0 , 62.8]	[0.89 , 5.46]
		89	[-52.1 , -9.7]	[1.20 , 6.54]	[14.6 , 65.9]	[0.82 , 5.78]
		188	[-57.4 , -14.8]	[1.15 , 6.70]	[15.8 , 70.6]	[0.68 , 5.55]
	90°-270°	22	[-49.2 , -10.1]	[1.61 , 6.55]	[5.8 , 87.2]	[0.45 , 3.57]
		89	[-51.4 , -14.3]	[1.41 , 7.49]	[17.3 , 97.9]	[0.23 , 4.07]
		188	[-53.4 , -17.4]	[1.67 , 7.19]	[22.2 , 106.9]	[0.13 , 4.00]

VI STIFFNESS PREDICTION MODEL

The objective of a predictive study is to provide insight on the FB static stiffness behavior with increasing temperature and suggest improvements in modeling. Rubio and San Andrés [17] forward a foil bearing structural stiffness prediction program based on Iordanoff's bump foil formulas [28]. The current investigation uses the simple computer program to predict changes in clearance with shaft temperature by matching the experimental stiffness versus FB deflection curves with the predictive model curves.

Description of Stiffness Prediction Model

Iordanoff derived the stiffness of a single bump based on its deflection (δ) due to a static force (F). The bumps are characterized as either one with both ends free, or one with a welded end and a free end. Obviously, the stiffness of a welded bump (K_W) is higher than the stiffness of a bump with two free ends (K_F). The major assumptions of Iordanoff's model are that a bump pitch (s) remains constant and the interactions between the bumps are neglected. The formulas for the two types of bump stiffness are:

$$K_W = \frac{F}{\delta} = \frac{Et^3 \sin^3\left(\alpha/2\right)}{6l_o^3 s^2 J(\alpha, \mu_f)\left(1-v^2\right)L_b} \tag{18}$$

and

$$K_F = \frac{F}{\delta} = \frac{Et^3 \sin^3\left(\alpha/2\right)}{12l_o^3 s^2 I(\alpha, \mu_f)\left(1-v^2\right)L_b} \tag{19}$$

E and v are the foil material Young modulus and Poisson ratio, respectively. The nominal bump half-length (l_o), height (h), and foil thickness (t) are provide in Table 1. The axial bump length (L_b) is the length of the bearing divided by the five axial sections of a bump strip. The parameters I and J are functions of the bump arc length (α) and μ_f is the dry friction coefficient. Figure 33 shows the noted bearing dimensions and the direction of the applied force and deflection for the stiffness approximation.
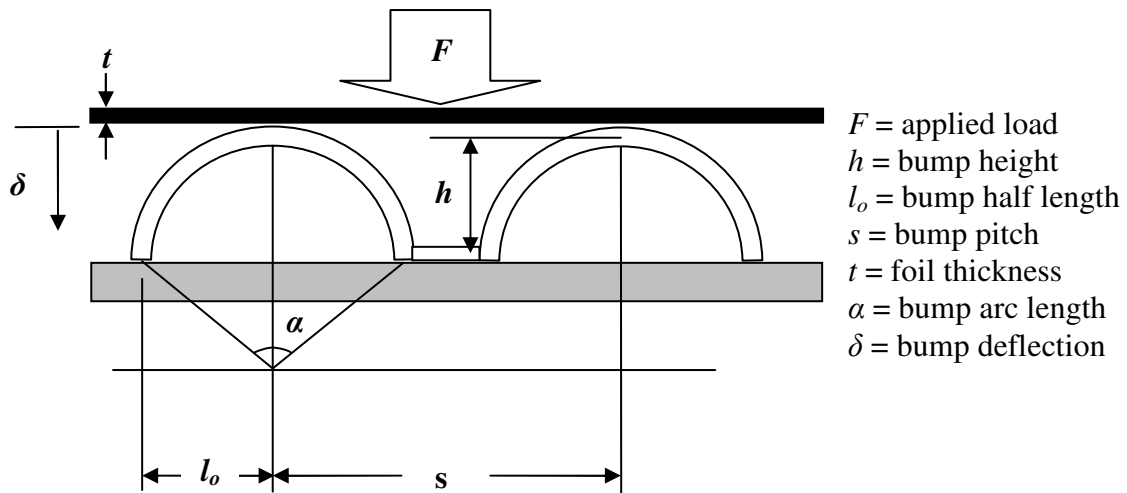
Figure 33 Bump dimensional parameters for stiffness approximation of a single bump.

The model includes differing bump stiffnesses with respect to angular position within the circumference of the bearing housing. Figure 34 shows the structural stiffness of a single bump as a function of its angular position based on the nominal dimensions and $\mu_f = 0.1$. The stiffness of the free end bumps is approximated as $K_F = 0.32$ MN/m. The higher stiffness magnitude ($K_W = 2.1$ MN/m) in the figure indicates a bump strip fixed end at every 70°. Lines added to Figure 34 show the direction of applied load location during the static tests.

Note the weldment at 280°. This weld may cause the aforementioned FB deflection limit from tests performed along the 270° bearing orientation. Recall that for a bump strip the individual bump stiffnesses increase from the free end to the fixed end from the accumulation of friction and interactive forces [7,8]. Observe the 90° load is directed towards the first bump of a strip, and the 270° load is directed towards the fourth bump of a strip. The stiffness of the first bump of a strip is expected to be relatively low, while the stiffness of the fourth bump should be near the maximum evidenced on a strip. This accounts for the markedly different stiffnesses experienced along the respective directions of the 90°-270° bearing orientation.
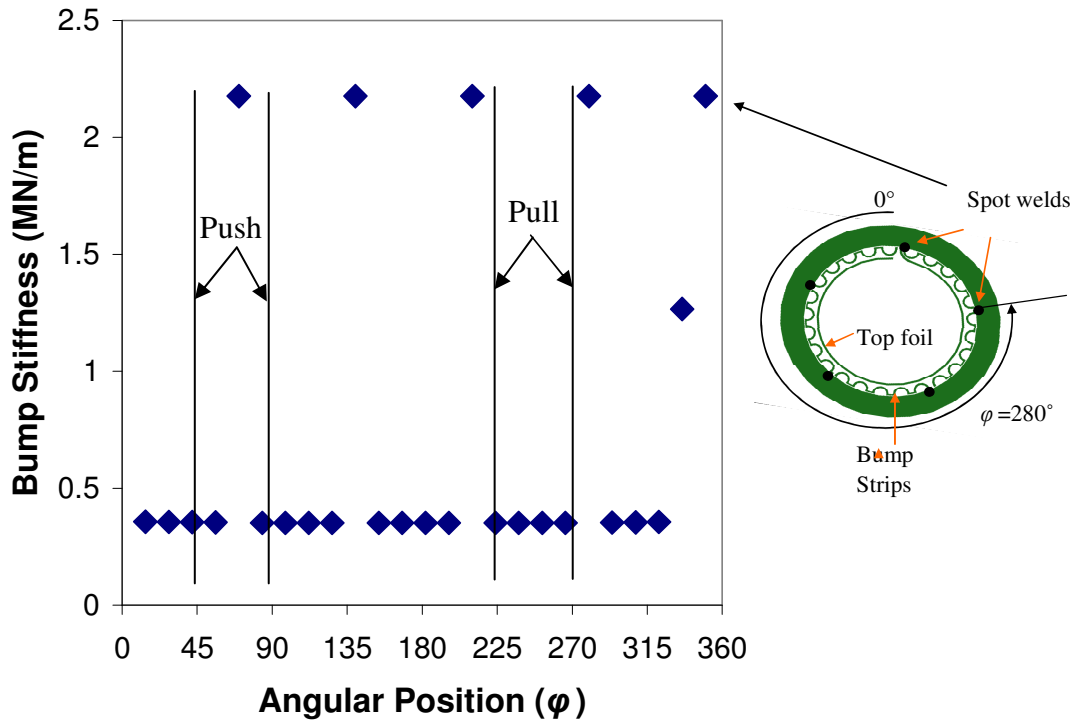
Figure 34 Predicted bump foil stiffness distribution showing weldment locations at every 70° [17].

The stiffness prediction model approximates each bump as a linear spring of known stiffness. Equation (18) provides the stiffness estimation of the five bumps welded to the FB housing. Equation (19) gives the estimated stiffness of the remainder of the bumps, with the exception of the bump at 336°. This is the bump next to the final bump, which is welded in conjunction with the top foil. This particular bump is given an intermediate stiffness ($K_I = 1.2$ MN/m), which is the average of K_W and K_F.

For small changes in deflection, the FB stiffness may be approximated as piecewise linear. Figure 35 shows the assemblage of the individual bump stiffnesses (k) to equal the FB stiffness (K) due to increasing FB deflection, where k is either K_W or K_F. Note that the FB stiffness is, of course, zero as the shaft translates within the nominal clearance (C_{nom}). As a single bump continues to deflect under the load from the shaft, another bump (or several bumps) becomes engaged, then the net stiffness increases and becomes the sum of the stiffnesses of the depressed bumps; e.g., $K_3 = k_1 + k_2 + k_3$.
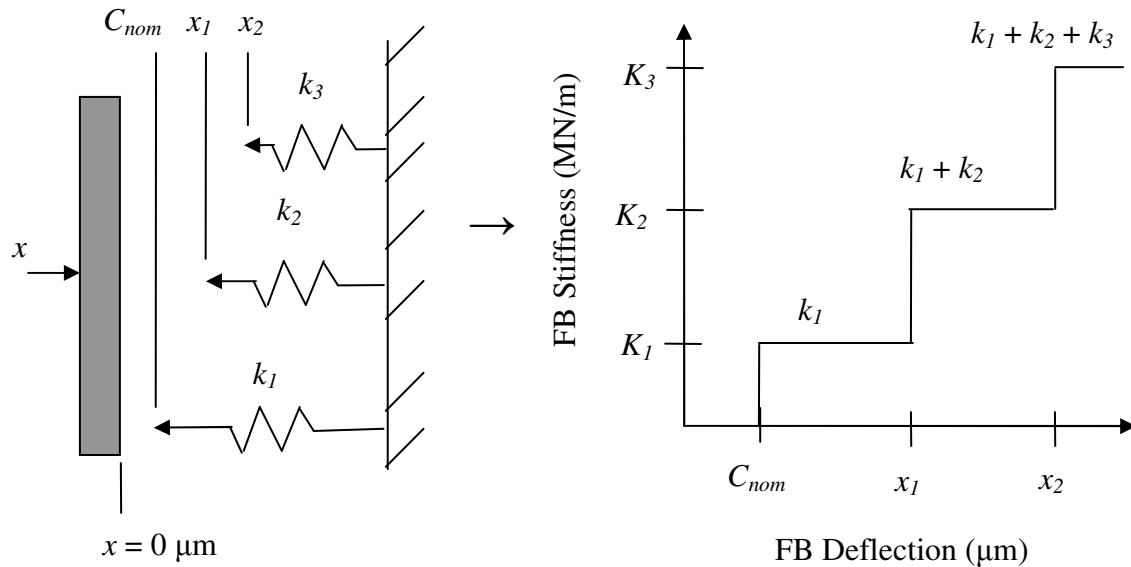
Figure 35 Schematic view showing piecewise linear FB stiffness approximation summing individual bump stiffness.

More specifically, the model determines the reaction forces of the foil structure based upon the actual clearance ($C_{act} = C_{nom} - \delta C$) and the range of FB displacements. Figure 36 shows the coordinate system used to determine the bump reaction forces. The *X-Y* coordinate system is the basis for deflection direction. The *X* coordinate is along the spot weld and the *Y* coordinate is 90° away in the direction of the free end of the top foil. The ζ-η coordinate system corresponds to the normal (ζ_i) and the transverse (η_i) deflections of each bump. The normal deflection direction is directed θ_i away from the spot weld, *X*.
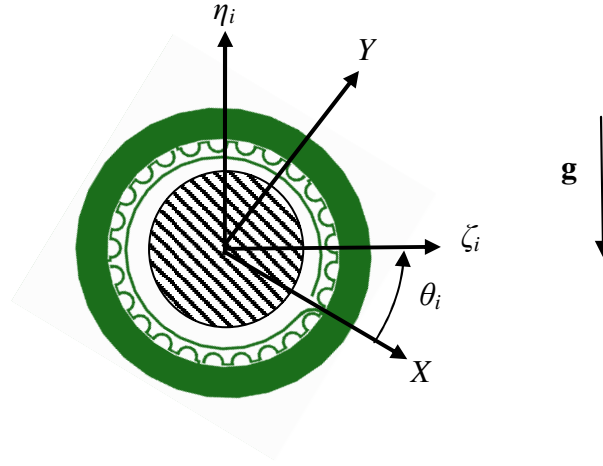
Figure 36 Bearing stiffness prediction model coordinate system.

The normal deflection of each bump, considering the nominal clearance (C_{nom}), the clearance differential (δC), and the deflections along the X and Y axes, is

$$\begin{aligned} \zeta_i &= X \cos \theta_i + Y \sin \theta_i - C_{act} \\ \zeta_i &= X \cos \theta_i + Y \sin \theta_i + \delta C - C_{nom} \end{aligned} \tag{20}$$

If $\zeta_i > 0$, then the reaction force of each bump is

$$F_{\zeta_i} = K_B(H_i)\zeta_i \tag{21}$$

where $H_i = h - \zeta_i$ is the actual bump height as a result of the deflection, and K_B (a function of H_i) corresponds to K_W or K_F, depending on the orientation of the load. The program then sums the reaction forces in the X and Y directions, respectively, as

$$F_{X_i} = \sum_{i=1}^{N} F_{\zeta_i} \cos \theta_i \tag{22}$$

and

$$F_{Y_i} = \sum_{i=1}^{N} F_{\zeta_i} \sin \theta_i \tag{23}$$

Finally, the overall FB reaction forces along the direction of applied load (β) is the sum

$$F_{\delta_i} = F_{X_i} \cos \beta + F_{Y_i} \sin \beta \tag{24}$$

The program plots this resultant force (F_δ) as a function of FB deflection (δ). A cubic polynomial curve is then used to fit the force versus FB deflection data, and the derivative of this cubic polynomial yields the predicted FB stiffness.

It is important for the reader to understand that the code used for the model differs from the data reduction scheme described in Section V. Recall that the data reduction of the experimental data separates a force versus FB deflection data into three regions. Then, a cubic polynomial curve fits the outer regions. However, the analytical (predicted) stiffness is derived from a continuous cubic polynomial curve fit over a certain displacement range covering both "positive" and "negative" deflections. Clearly, this procedure does not accurately predict the FB behavior at small deflections. Note that, over the deflection range encompassing the bearing clearance, the FB stiffness should actually be zero. The physical model is, thus, inaccurate for deflections within the noted range due to the reduced goodness of fit of the cubic polynomial at small bearing deflections.

Bump Structural Stiffness Change with Friction Coefficient

A friction force reacts to relative motion between the bumps and the top foil and the bumps and the FB housing. As the dry friction coefficient increases, the friction force opposing motion increases between the contacting surfaces, and thus increases the bump stiffness. Figure 37 shows the change in free-end and fixed-end individual bump stiffness as a function of the dry friction coefficient (μ_f). Stiffness of bump begins to increase sharply for dry friction coefficients above 0.6. Rubio and San Andrés [17] find that dry friction coefficients ranging between 0.01 and 0.2 correlate best with their static stiffness experimental results. Note from the figure that within this friction coefficient range (0.01 to 0.2) the bump stiffness does not change considerably. Results described herein are expected to experience the same range of magnitudes for μ_f.

$l_o = 2.032$	mm
$h = 0.381$	mm
$s = 4.572$	mm
$t = 0.102$	mm
$E = 2.13 \times 10^{11}$	Pa
$v = 0.29$	
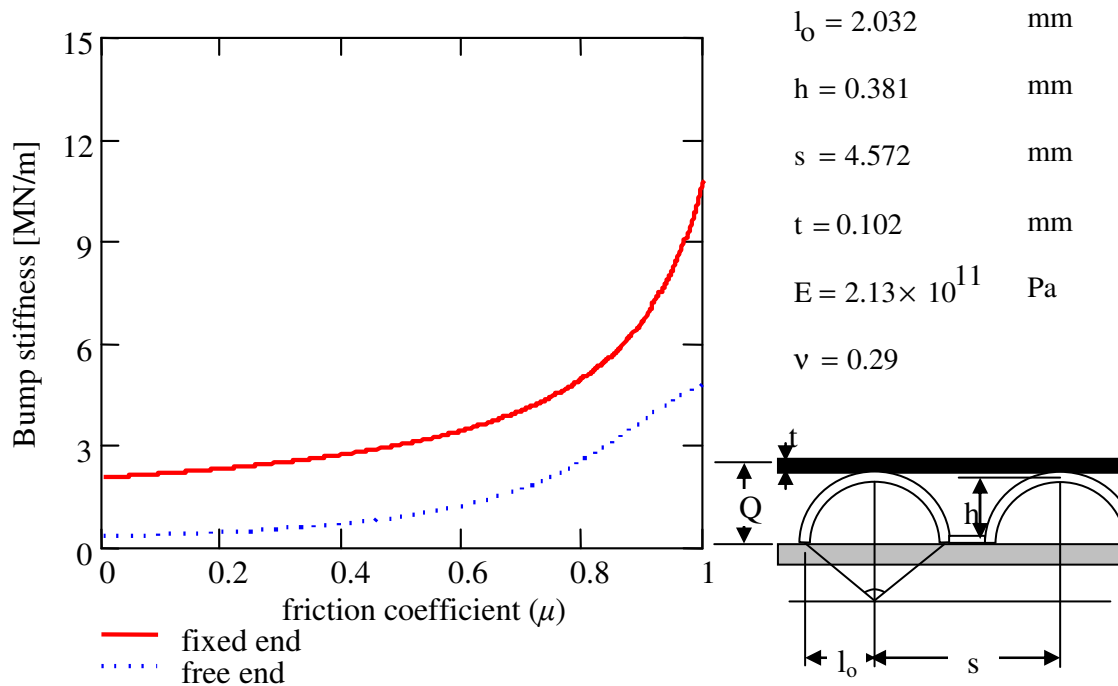
Figure 37 Predicted structural stiffness of a single bump for increasing dry friction coefficient (nominal bump foil dimensions). Physical parameters for analysis appear on the right.

Bump Structural Stiffness Change with Foil Young Modulus

The bump structural stiffness model is sensitive to Young Modulus (E) thus it is important to assess the influence of over the range of test temperatures. As the test temperature increases from 21°C to 188°C, E of the bump foil material decreases from 213 GPa to approximately 201 GPa (5.4% decrease) [29] (Appendix E). The bump stiffness is directly proportional to E; therefore, by linearity, any percent decrease in E leads to an equal decrease in bump stiffness.

FB Structural Stiffness Change with Clearance

Figure 38 shows the change in static load versus FB deflection behavior as the radial clearance varies for the 38.125 mm shaft. The load direction $\beta = 45°$, nominal clearance $C_{nom} = 22.9$ m, friction coefficient $\mu_f = 0.1$, and modulus $E = 213$ GPa remain

constant. The actual clearance, C_{act}, between the bearing and shaft is given as $C_{act} = C_{nom} - \delta C$. When the actual clearance is equal to the nominal clearance, $C_{act} = C_{nom}$, the bearing deflection increases with little applied load (predicted as 0 N) until the clearance is traversed and the bumps are engaged, at which point the load begins to increase. When no clearance exists, that is $C_{act} = 0$ µm, the load is linear with FB deflection. As the clearance differential decreases and becomes $\delta C = -C_{nom}$, $C_{act} = 2C_{nom}$ and the bearing moves twice the nominal clearance before the bumps become engaged.
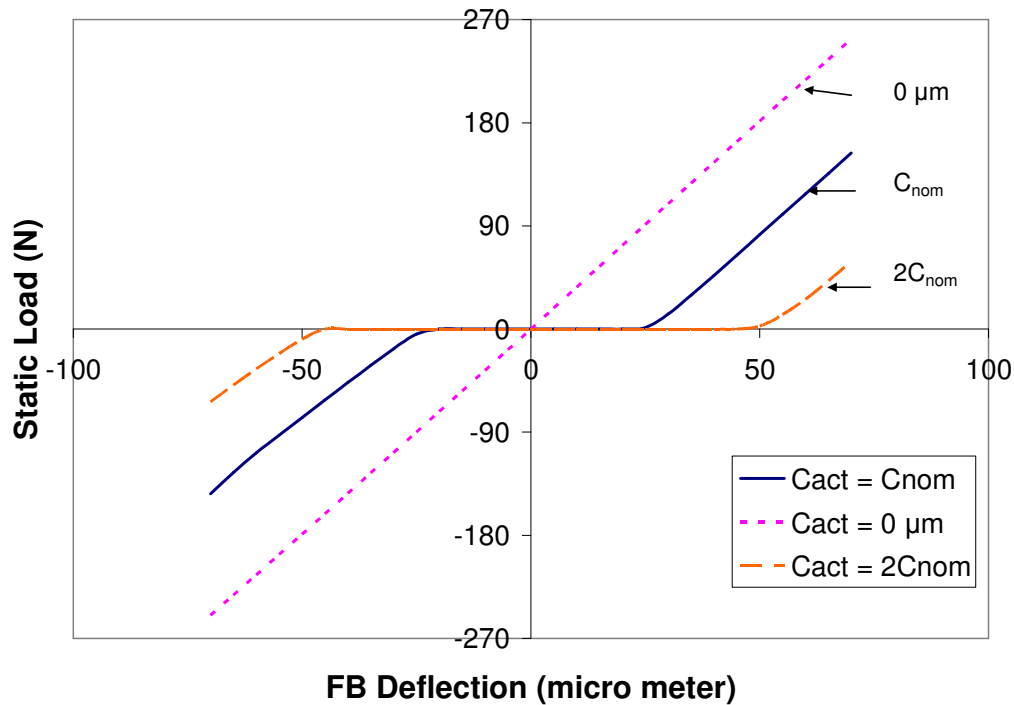
Figure 38 Predicted static load versus FB deflection for different bearing clearances (38.125 mm shaft, $\mu_f = 0.1$, $C_{nom} = 22.9$ µm, $\beta = 45°$).

Figure 39 shows the change in stiffness versus FB deflection behavior as the clearance varies. The load direction $\beta = 45°$, nominal clearance $C_{nom} = 22.9$ µm, friction coefficient $\mu_f = 0.1$, and modulus $E = 213$ GPa, again, remain constant. For the case of no clearance differential, $C_{act} = C_{nom}$, the nominal clearance dictates FB stiffness behavior. For $C_{act} = 0$ µm, there is no clearance and the stiffness remains constant along the FB deflection. As the clearance differential decreases and becomes $\delta C = -C_{nom}$, C_{act}

$= 2C_{nom}$ and the stiffness decreases as indicated by the wider stiffness curve. In the first and third cases, no stiffness is shown for the respective FB deflection range $-C_{act} \leq x \leq C_{act}$.
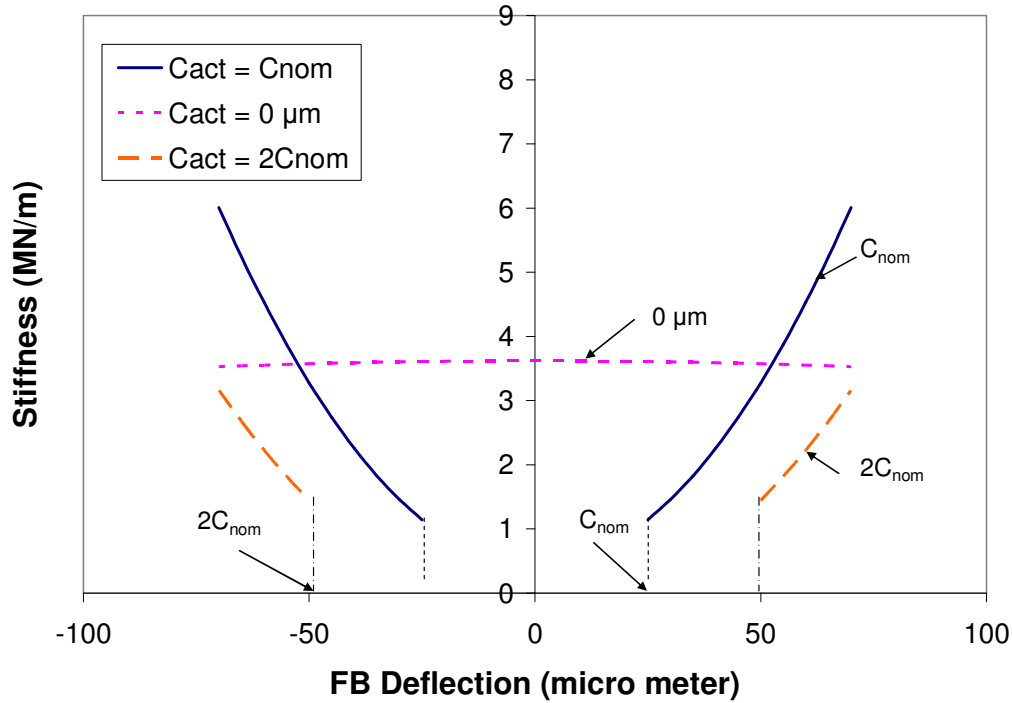
Figure 39 Predicted structural stiffness versus FB deflection for different bearing clearances (38.125 mm shaft, μ_f = 0.1, C_{nom} = 22.9 μm, β = 45°).

Figure 38 and Figure 39 show the expected behaviors of load and stiffness with FB deflection, respectively, for the case of $\delta C = C_{nom}$ ($C_{act} = 0$). Thus, experimental results indicate that a small clearance does exist between the shaft and the bearing since neither is the static load linear nor is the stiffness constant with respect to FB deflection.

FB Structural Stiffness Change with FB Deflection

A limitation of the code arises because the model assumes uniform push-pull stiffnesses for a certain applied load angle, β. That is, the predicted stiffness for the push and pull directions are equal for the same deflection, regardless of the load direction

designated. For instance, Figure 34 shows that a load applied towards a spot weld at β_1 = 280° would experience more resistance than an equal load applied at β_2 = 100° (i.e., β_1 - 180°). However, Figure 40 shows a symmetric stiffness curve about the bearing center when β = 280°.

$\mu_f = 0.1$

$x_o = 0$ micro meter

$\delta_{max} = 70.0$ micro meter

$\delta_{min} = -70.0$ micro meter

$c_{nom} = 22.9$ micro meter

$\delta C = 0.0$ micro meter

$E = 213$ GPa

$\beta = 280°$
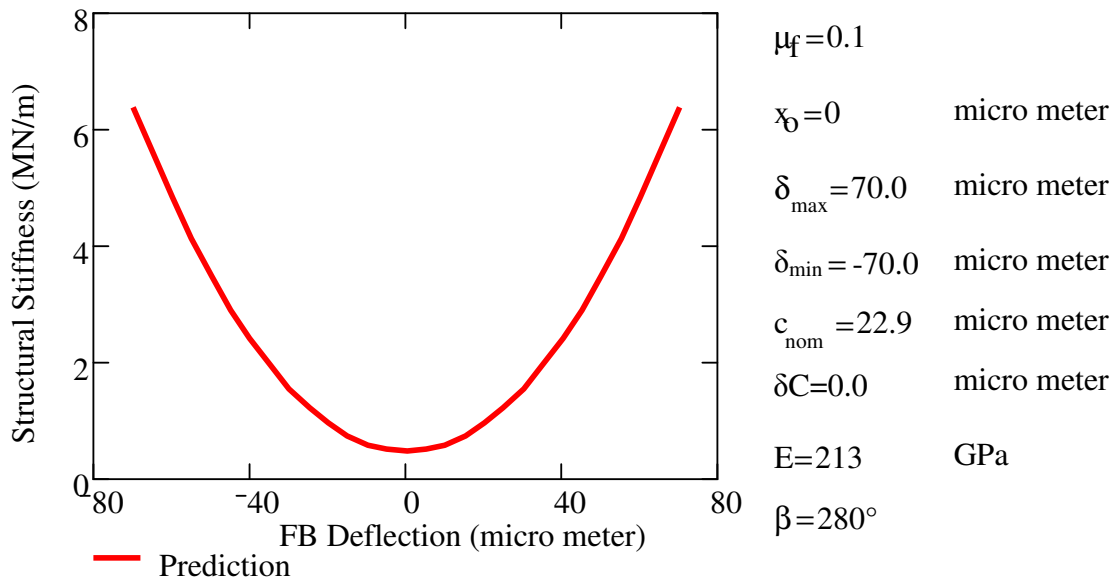
Figure 40 Predicted structural stiffness versus FB deflection for equal deflection along opposite directions (38.125 mm shaft, μ_f = 0.1, C_{nom} = 22.9 μm, δC = 0 μm, δ_{min} = -70 μm to δ_{max} = 70 μm, β = 280°). Physical parameters for analysis appear on the right.

The model yields a prediction based on an input deflection range, δ_{min} to δ_{max}. Generally, the input deflection range is taken from experiments. For instance, Figure 32 shows that, for the 90°-270° bearing orientation with the 38.125 mm shaft at 22°C, the deflection range from δ_{min} = -49.2 μm to δ_{max} = 87.2 μm yields experimental stiffnesses of 6.55 MN/m and 3.57 MN/m from curve fit estimates, along the respective directions. Introducing an offset, x_o, to the experimental FB deflection before inputting the range into the model simulates a shift of the bearing center. The adjusted FB deflection becomes $\delta_{adj} = (\delta - x_o)$, where δ is the measured deflection. This changes the amount of deflection along each load direction, which allows adjustments to the predicted stiffness magnitude for each load direction. Figure 41 compares the resulting predicted and experimental static versus FB deflection data for this particular test case. Note that the

center of the experimental force curve (at $F = \sim 0$ N) has been shifted, via x_o, nearly to the edge of $-C_{nom}$.
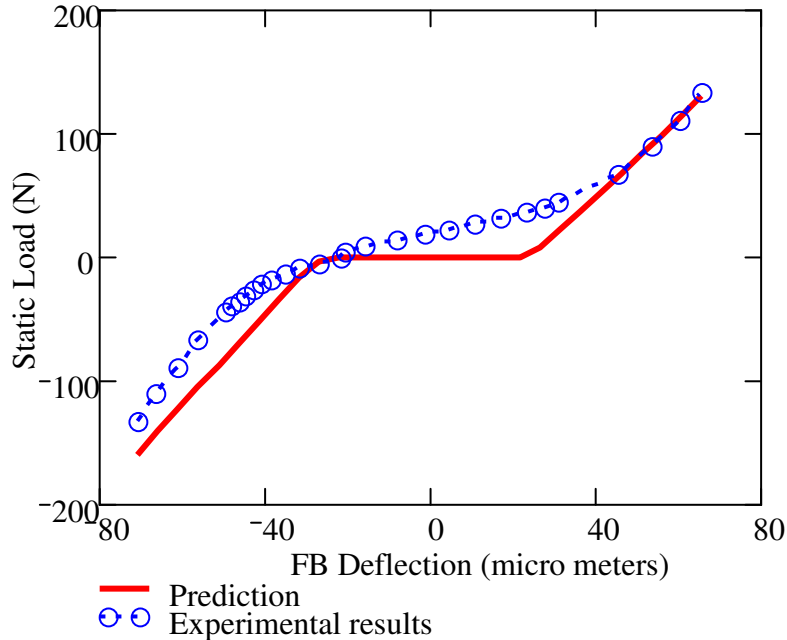
Figure 41 Predicted and experimental static load versus adjusted FB deflection, with x_o = 25.8 µm, showing the correction for 90°-270° bearing orientation at 22 °C (38.125 mm shaft, μ_f = 0.01, C_{nom} = 22.9 µm, δC = 0.0 µm, x_o = 25.8 µm, β = 90°).

Figure 42 shows the effect of this offset on the predicted stiffness plotted versus the adjusted FB deflection. The offset x_o = 21.8 µm changes the deflection range to δ_{min} = -71.0 µm to δ_{max} = 65.4 µm and yields predicted stiffnesses of 6.60 MN/m (+0.6% error) and 5.65 MN/m (+37% error), along the 270° and 90° directions, respectively. Further adjustments to the FB deflection offset may optimize the percent error along each direction of motion.
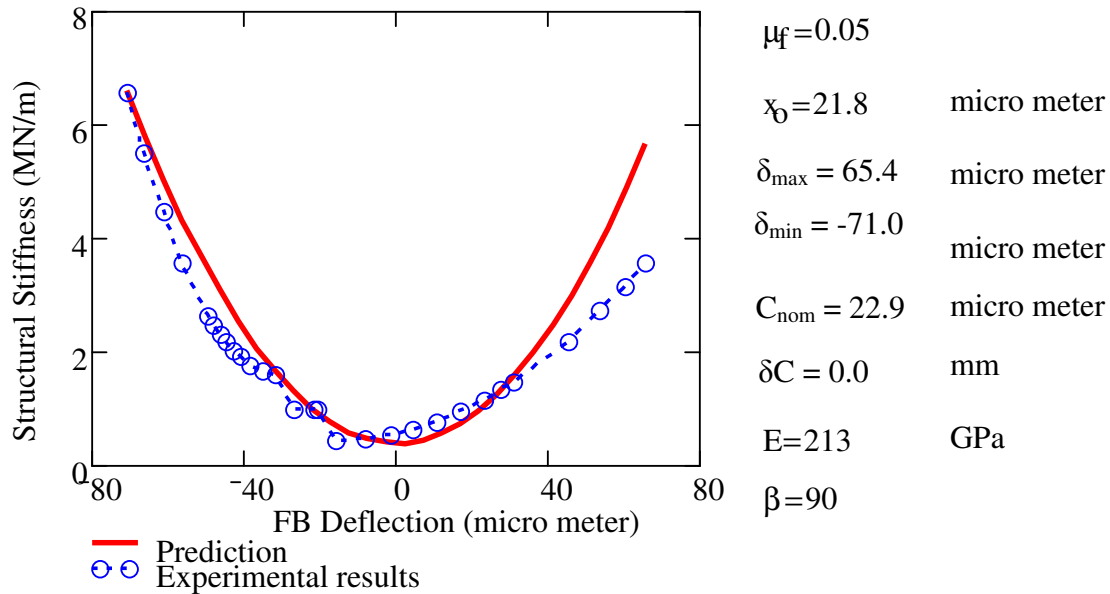
Figure 42 Predicted and experimental structural stiffness versus adjusted FB deflection, x_o = 21.8 μm, showing the correction for 90°-270° bearing orientation at 22°C (38.125 mm shaft, $μ_f$ = 0.01, C_{nom} = 22.9 μm, $δC$ = 0.0 μm, x_o = 21.8 μm, $β$ = 90°).

Comparison between Predicted and Experimental Results

The previous sections show the behavior of the model due to changes of certain parameters. For example, increasing the bearing clearance decreases FB structural stiffness, while increasing the dry friction coefficient increases bump stiffness, along with the ensuing FB stiffness. This section shows how the various parameters may be changed to make predicted force and stiffness curves coincide with the corresponding experimental curves to estimate certain parameters.

Figure 43 shows the force versus bearing deflection prediction and experimental results for the 45°-225° bearing orientation with the 38.125 mm shaft at T_S = 22°C. Note that, unlike the experimental force curve, the predicted force varies linearly for increasing FB deflection values along each direction. The analytical model idealizes the actual non-linear FB stiffness. In the regions of the linear force behavior, the resulting FB stiffness is expected to be constant. However, since the predictive force curve is

fitted with a continuous cubic polynomial, the reported predicted stiffness follows the same even behavior as reported by the experimental stiffness curves.
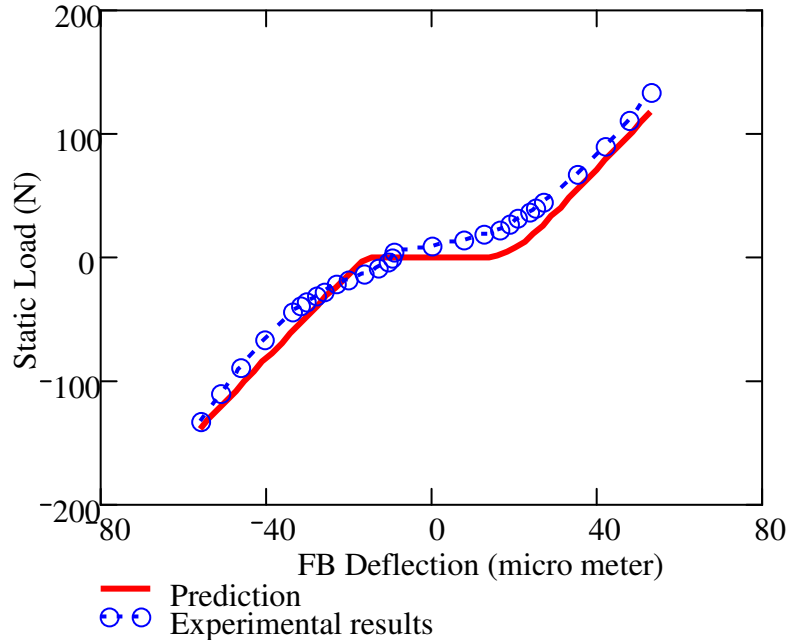
Figure 43 Predicted and experimental static force versus adjusted FB deflection, x_o = 10 μm, showing the correction for 45°-225° bearing orientation at 22°C (38.125 mm shaft, μ_f = 0.1, C_{nom} = 22.9 μm, δC = 8.0 μm, x_o = 10.0 μm, β = 45°).

Figure 44 shows the structural stiffness versus bearing deflection prediction and experimental results for the 45°-225° bearing orientation with the 38.125 mm shaft at T_S = 22°C. The experimental stiffness along the 225° direction is higher than that along the 45° direction. A deflection offset x_o = 10 μm to the predicted code provides an appropriate adjustment to the stiffnesses along the respective directions; the adjusted deflection range becomes δ_{min} = -56.2 μm to δ_{max} = 52.8 μm. Adjustments made to the clearance differential (δC) suggest that the actual radial clearance (C_{act}) may be less than the nominal clearance. A differential δC = 8 μm (C_{act} = 14.9 μm) provides good coincidence between the predicted and experimental stiffnesses.
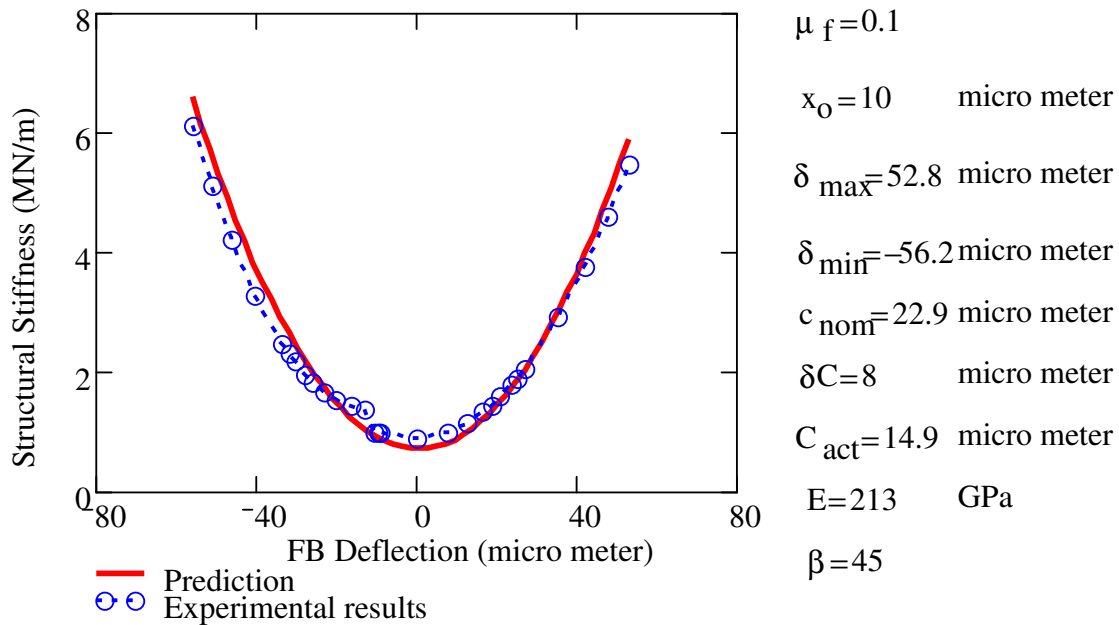
Figure 44 Predicted and experimental structural stiffness versus adjusted FB deflection, x_o = 10 μm, showing the 45°-225° bearing orientation at 22°C (38.125 mm shaft, μ_f = 0.1, C_{nom} = 22.9 μm, δC = 8.0 μm, x_o = 10 μm, β = 45°).

Figure 45 and Figure 46 show the predicted and experimental structural stiffness versus FB deflection curves for the 45°-225° bearing orientation with the 38.125 mm shaft at temperatures of 89°C and 188°C, respectively. The appropriate deflection adjustments are made such that the predicted stiffnesses along the respective directions match the relative magnitudes of the experimental results. From these two figures, notice that the clearance differential decreases to δC = 0 μm at 188°C from its assumed value at room temperature δC = 8 μm. This indicates the bearing clearance increasing with temperature. The dry friction coefficient must increase from 0.1 to 0.15 over the same temperature range to maintain good agreement between the prediction and experiments. Note that the values of the estimated model parameters are not as important as the trends which they reveal. The demonstration shows that the changes in clearance and friction coefficient, or any of the other analytical parameters of interest, with increasing shaft temperature may be tracked by the model.

$\mu_f = 0.1$

$x_o = 8$ micro meter

$\delta_{max} = 57.9$ micro meter

$\delta_{min} = -60.1$ micro meter

$c_{nom} = 22.9$ micro meter

$\delta C = 3.4$ micro meter

$C_{act} = 19.4$ micro meter

$E = 208.3$ GPa

$\beta = 45$
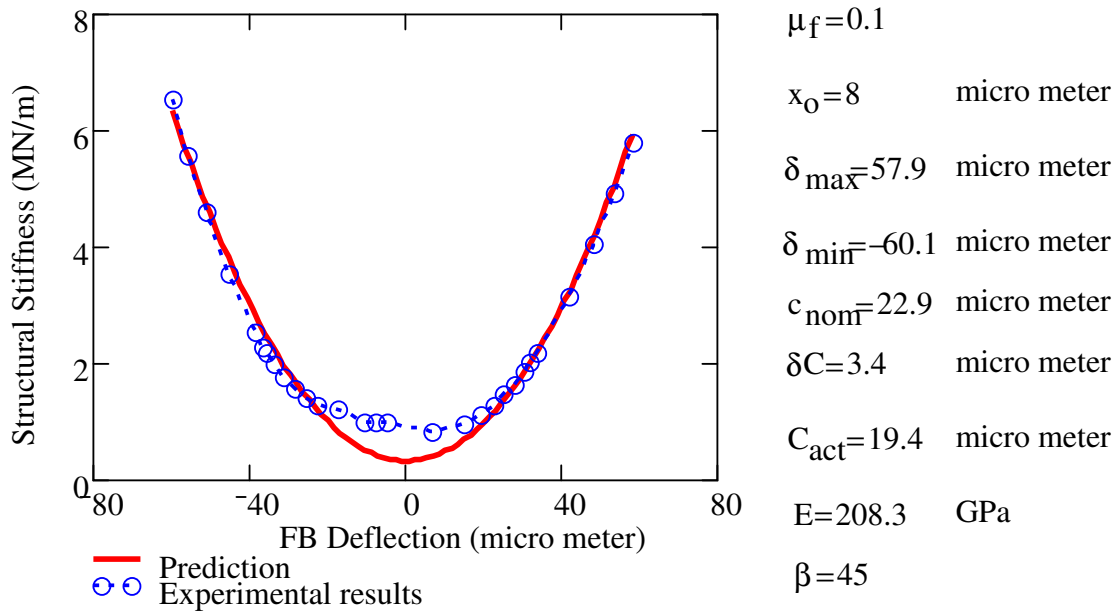
Figure 45 Predicted and experimental structural stiffness versus adjusted FB deflection, x_o = 8 μm, showing the 45°-225° bearing orientation at 89°C (38.125 mm shaft, μ_f = 0.1, C_{nom} = 22.9 μm, δC = 3.4 μm, x_o = 8 μm, β = 45°).

$\mu_f = 0.15$

$x_o = 9$ micro meter

$\delta_{max} = 61.6$ micro meter

$\delta_{min} = -66.4$ micro meter

$c_{nom} = 22.9$ micro meter

$\delta C = 0$ micro meter

$C_{act} = 22.9$ micro meter

$E = 201.5$ GPa

$\beta = 45$
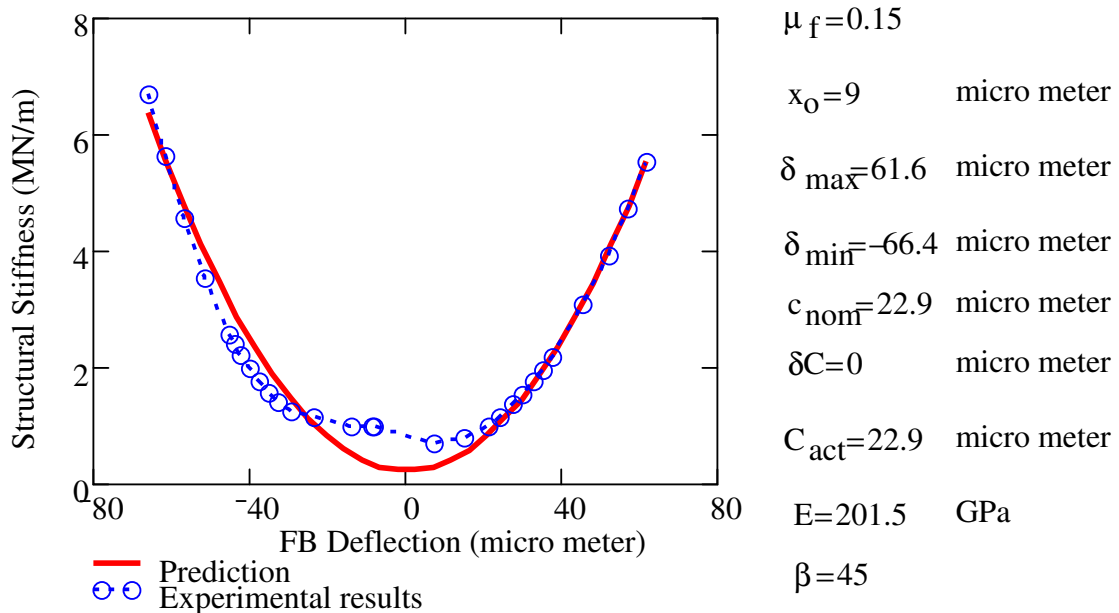
Figure 46 Predicted and experimental structural stiffness versus adjusted FB deflection, x_o = 9 μm, showing the 45°-225° bearing orientation at 188°C (38.125 mm shaft, μ_f = 0.15, C_{nom} = 22.9 μm, δC = 0.0 μm, x_o = 9 μm, β = 45°).

The predicted FB stiffness is noted at a deflection of 40 μm along each load direction for each shaft temperature. The stiffnesses in the respective bearing orientations show a decrease in magnitude with increasing temperature. The model predicts, for the shaft temperature change from $T_S = 22°C$ to $T_S = 188°C$, a 35% and 32% decrease for the 45°-225° bearing orientation. The predicted static stiffness decrease for the same temperature range is 47% along each direction for the 90°-270° bearing orientation.

VII DYNAMIC STRUCTURAL STIFFNESS, EQUIVALENT VISCOUS DAMPING, AND DRY FRICTION PARAMETERS IN A GAS FOIL BEARING

The characterization of FB dynamic structural parameters follows. The parameters of interest include FB dynamic stiffness, K, equivalent viscous damping, C_{eq}, and/or friction coefficient, μ_f. The experimental method varies the amplitude of the dynamic load, F_O, its excitation frequency, and the operating shaft temperature.

Experimental Procedure

The experiments for identification of FB structural force coefficients include single frequency dynamic loads of differing amplitudes. Table 16 summarizes the experimental parameters. An electromagnetic shaker is suspended from cables connected to the ceiling of the test facility. The shaker mount natural frequency in the direction of loading is approximately 1 Hz. The shaker excites the FB, which is supported on the stationary shaft, along the horizontal direction to produce radial bump foil deflections. The frequency at which the dynamic load is applied ranges from 40 to 200 Hz, varying at 20 Hz increments. Dynamic load levels are selected as 13.3 N, 22.2 N, and 31.1 N (3 lbs, 5 lbs, and 7 lbs) to avoid the lightly loaded region, $F_O < 8.9$ N (2 lbs). Recall in Section V that this lightly loaded region showed high uncertainty in the static load behavior. The 31.1 N amplitude of dynamic load is chosen as a precaution as not to cause permanent damage or distortion to the bump foils. As shown in Figure 47, the experiments are conducted at the 45°-225° bearing orientation with respect to the foil spot weld location (0°). This bearing orientation is chosen to avoid applying dynamic load directly to the spot weld location, which may yield misleading stiffness behavior. The shaft temperature at which the experiments are conducted ranges from room temperature, ~21° C (70°F), up to 188°C (370°F), which is limited by the operational

temperature limit of the Emralon 33 spray-on coating (400°F) applied to the top foil. The shaft test temperatures are controlled +/- 1°C via a cartridge heater and control circuit. Once the shaft surface attains the target temperature, the system stands for 30 minutes before testing begins. This ensures the shaft and bearing housing are respectively heated throughout and all material expansion is complete. Section IV details the expected behavior of the radial clearance between the shaft and FB throughout the test temperature range.

Table 16 Shaker test parameters

Dynamic Load, N [lb]	13.3, 22.2, 31.1 [3, 5, 7]
Load Tolerance, N [lb]	+/- 0.445 [0.1]
Frequency Range, Hz	40-200, increments of 20 Hz
Shaft Temperature, °C	22, 77, 132, 188
Bearing Orientation	45°
Bearing Mass[6], kg [lb]	0.295 [0.650]
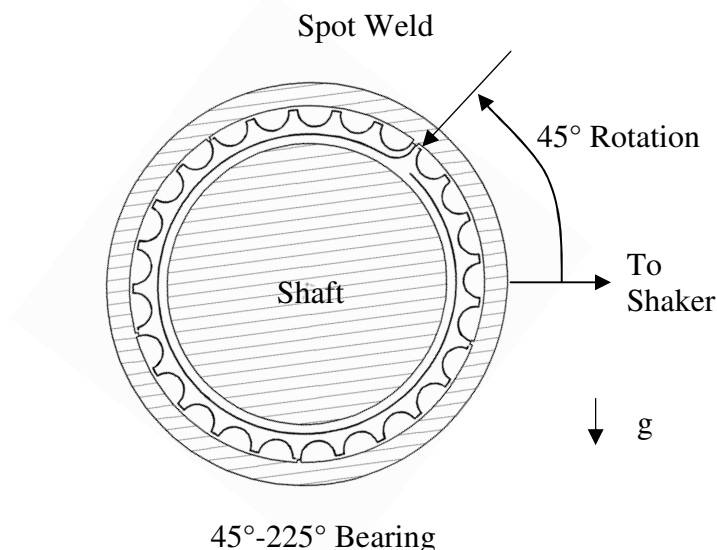
Figure 47 Test FB angular orientations for shaker tests.

---

[6] Bearing mass includes load cell, accelerometer, and attachment hardware.

Tests are performed at one load amplitude F_O = 13.3 N for the nine frequencies. Then the subsequent load amplitude is input to the DAQ system and excitation commences for the nine frequencies. Three trials are performed for each load and frequency span with the shaft at a given test temperature to determine repeatability. The test results prove highly repeatable. For example, structural stiffness data are compiled for three trials. An average and standard deviation of the three reported stiffnesses at each frequency are calculated, and the standard deviation is reported as a percentage of the average to indicate error. A maximum percent error of 3.71% is evident. Appendix F shows the compiled data with a complete list of the percent errors for all experiments.

Parameter Identification Procedure

The identification procedure for estimation of FB structural force coefficients follows the procedures advanced by Rubio and San Andrés [19] and Salehi et al. [18]. The harmonic forcing function $F(t)$, of known frequency and magnitude, from the shaker causes a response of the FB. The response is measured by the displacement and acceleration sensors. These recorded responses allow for the determination of FB stiffness and equivalent viscous damping.

The equation of motion (EOM) for the FB mass, M, as a SDOF system is

$$M\ddot{x} = F(t) - F_B \tag{25}$$

where $F(t) = F_o \cos(\omega t)$ and F_B is the reaction force of the foil bearing. F_O is the excitation force amplitude of the shaker at frequency ω. The reaction force of the FB consists of the elastic restoring force from its structural stiffness (K) and a dissipative energy force due to dry friction between the mating surfaces, $F_{DRY}\operatorname{sgn}(\dot{x})$ [19]. Thus, the EOM becomes

$$M\ddot{x} + Kx + F_{DRY}\operatorname{sgn}(\dot{x}) = F_o \cos(\omega t) \tag{26}$$

In the test data analysis, the energy dissipation over one cycle of motion leads to estimates of an equivalent viscous damping, C_{eq}, or a dry-friction force, F_{DRY}. The FB

structural stiffness is identified using the mechanical impedance model in the frequency domain.

The work done by the shaker on the FB over a period of motion is

$$W = \int F(t)\dot{x}(t)dt = -\pi F_O X \sin(\theta) \tag{27}$$

where X is the bearing displacement amplitude and θ is the phase lag between the excitation force F and the response x.

For one period of motion, the energy dissipated by viscous damping forces, E_V, or the energy dissipated by dry friction, E_F, are calculated as:

$$E_V = \int C_{eq}\dot{x}dx = C_{eq}\pi\omega X^2 \tag{28}$$

and

$$E_F = \int F_{DRY}\,\text{sgn}(\dot{x})dx = 4F_{DRY}X \tag{29}$$

This energy dissipation approach states that the external work input must equal the energy dissipated by each damping mechanism. Therefore, setting equation (27) equal to Equation (28) or Equation (29), the equivalent viscous damping force coefficient and the dry-friction force, respectively, from [18,19] and Ginsberg [30] are

$$C_{eq} = \frac{W}{\pi\omega X^2} = \frac{-F_O\sin\theta}{\omega X} \tag{30}$$

and

$$F_{DRY} = \frac{W}{4X} = \frac{-F_O\pi\sin\theta}{4} \tag{31}$$

Assuming a simple friction model, the dry friction force is $F_{DRY} = \mu_f F_O$, where F_O is the force acting normal to the plane of sliding motion. From this formulation, it follows that the dry-friction coefficient, μ_f, is

$$\mu_f = \frac{F_{DRY}}{F_O} = \frac{-\pi\sin\theta}{4} \tag{32}$$

As mentioned above, the FB structural stiffness is identified using the mechanical impedance model in the frequency domain. The transfer function gives the relationship between the input force, F, and the output displacement, x.

$$\frac{x}{F} = \frac{1}{K - M\omega^2 + iC_{eq}\omega} \tag{33}$$

Here, M is the system mass and K is the FB structural stiffness. The inverse of the transfer function gives the mechanical impedance of the system, F/x. The mechanical impedance model for a SDOF system is

$$\frac{F}{x} = (K - M\omega^2) + iC_{eq}\omega \tag{34}$$

The real part of the mechanical impedance gives the FB dynamic structural stiffness $(K - M\omega^2)$, and the imaginary part of the mechanical impedance provides C_{eq}, identical in magnitude to that derived from Equation (30) [19].

Manipulating Equation (33) leads to the following development, where $\dot{x} \quad x\omega$ and $\ddot{x} \quad -x\omega^2$:

$$F - M\ddot{x} = x(K + iC_{eq}\omega) \tag{35}$$

Equation (35) leads to a transfer function in which the inertia term, $M\ddot{x}$, is subtracted:

$$\frac{x}{F - M\ddot{x}} = \frac{1}{K + iC_{eq}\omega} \tag{36}$$

The inverse of Equation (36) gives the mechanical impedance, which isolates the FB stiffness, yields

$$\begin{aligned} K(\omega) &= \text{Re}[(F - M\ddot{x})/x] \\ C_{eq}\omega &= \text{Im}[(F - M\ddot{x})/x] \end{aligned} \tag{37}$$

Note that the experimental results below indicate that the FB structural stiffness is not constant as a function of excitation frequency. Therefore, the notation $K(\omega)$ is used to signify the frequency-dependence of the FB stiffness.

A Mathcad® code processes the recorded time traces (displacement, acceleration, force), transforms the data using an FFT algorithm into the frequency domain, and performs the various operations to extract the test FB force coefficients.

Experimental Results

Two resonant frequencies exist for the experimental setup. The natural frequency associated with the FB mass, as shown in Appendix G, is approximately 260 Hz. The natural frequency of the shaft and indexing fixture assembly is identified in rap tests as approximately 380 Hz. Results in Appendix G identify a resonance band, the band of frequencies encompassing the two natural frequencies of the test setup, from 230 Hz up to 380 Hz. Performing test within this frequency span produces odd-integer harmonics (especially 5X and 7X) vibration amplitudes of the same order of magnitude as the fundamental frequency. Figure 48 shows the waterfall plot of the 20 N load cell signals with the test shaft at $T_S = 188°C$ showing excessive 5X- and 7X-synchronous vibration component for excitation frequency 40 Hz to 420 Hz.
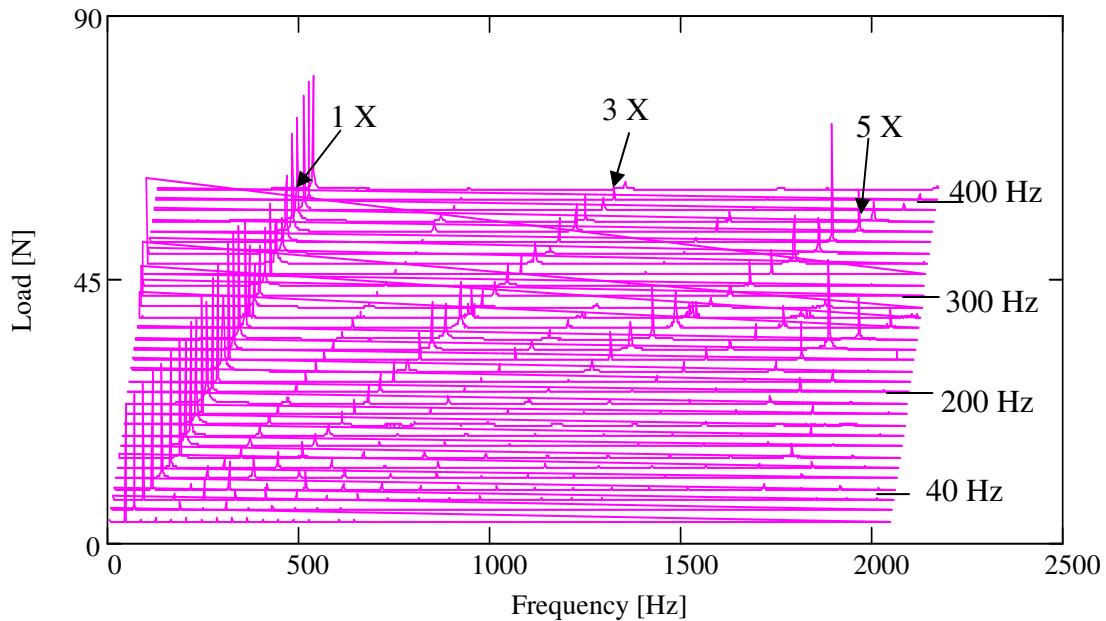
Figure 48 Waterfall plot of dynamic load cell signal showing excessive 5X- and 7X-synchronous vibration component for excitation frequency 40 Hz to 420 Hz (T_S = 188°C and F_O = 20 N).

Note that odd-integer harmonics are typical of the frequency spectrum of a system with dry friction; however, the peak amplitude of each subsequent harmonic is expected to be 1/n (for n = 3, 5, 7, etc.) of the response at the fundamental frequency.

These results show the 5X and 7X responses of the same magnitude or greater than those of the fundamental frequency. These excessive amplitude odd-integer harmonics lead to test results with low repeatability. Therefore, tests and analysis of single frequency excitation in this report are restricted to frequencies below 200 Hz.

Figure 49 shows the three applied dynamic loads versus excitation frequency at 22°C. The plot clearly shows steady amplitude of loading for the frequency range tested. This figure attests to the repeatability and reliability of the DAQ system for automatically saving data at desired target loads. Also, this ensures that changes in experimental FB dynamic behavior are not caused by erratic load conditions. This behavior is common to all tests.

Figure 50 shows the measured FB acceleration magnitudes for the three load cases versus excitation frequency for shaft at 22°C (ambient condition). Obviously, acceleration magnitudes increase with load magnitude and frequency.
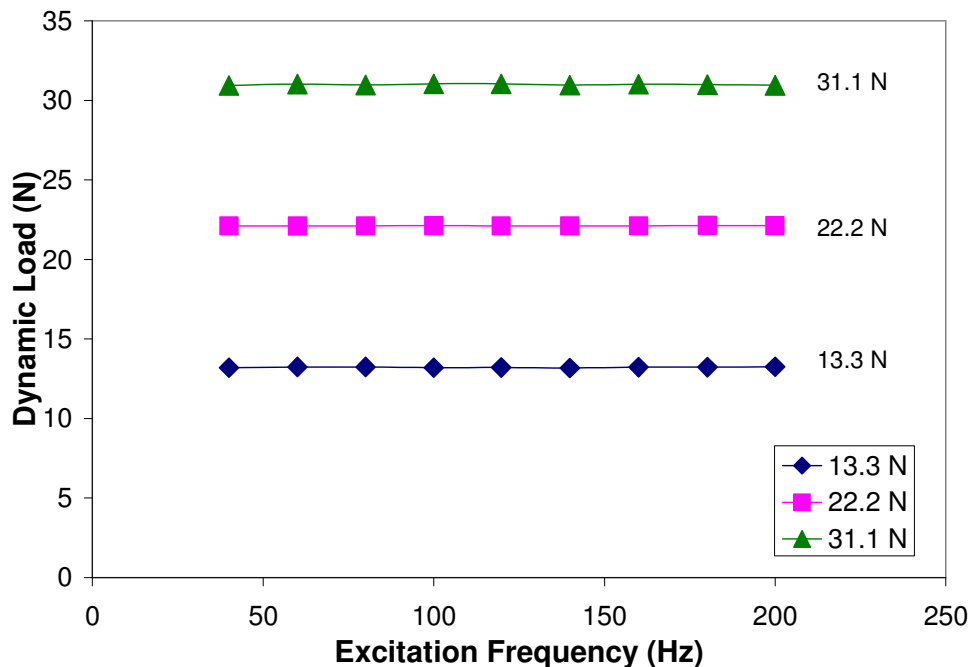
Figure 49 Applied dynamic load amplitude versus excitation frequency for all loads with shaft at 22°C (38.125 mm shaft, C_{nom} = 22.9 μm).
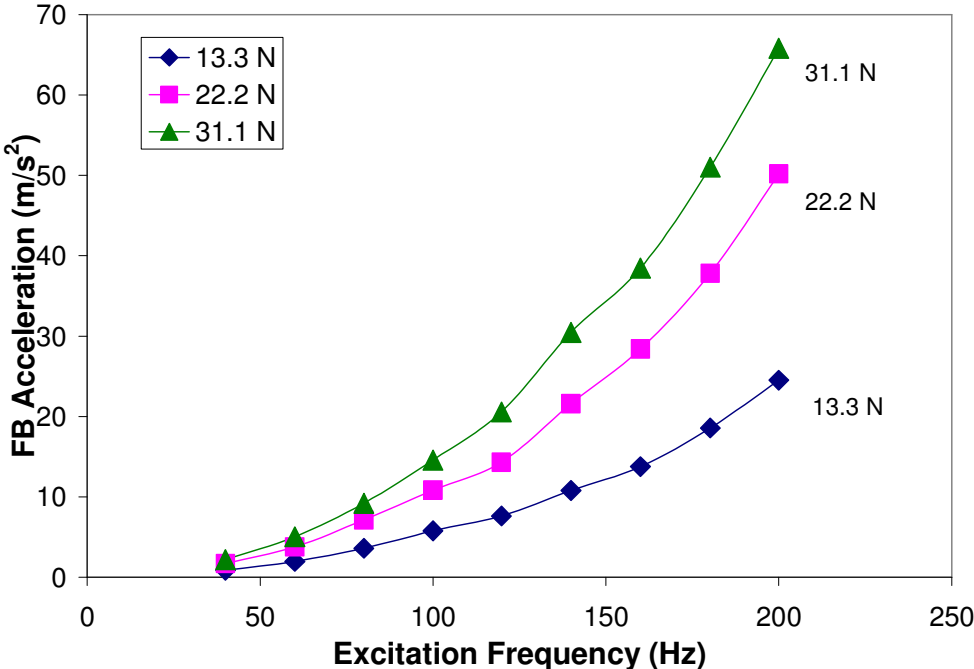
Figure 50 FB acceleration magnitude versus excitation frequency for all test load cases with shaft at 22℃ (38.125 mm shaft, C_{nom} = 22.9 μm).

Figure 51 shows the FB motion amplitudes versus excitation frequency for the four load cases at 22°C. The maximum dynamic displacements for the 13.3N and 31.1-N load cases are approximately 13 μm and 38 μm, respectively. This is the baseline case.
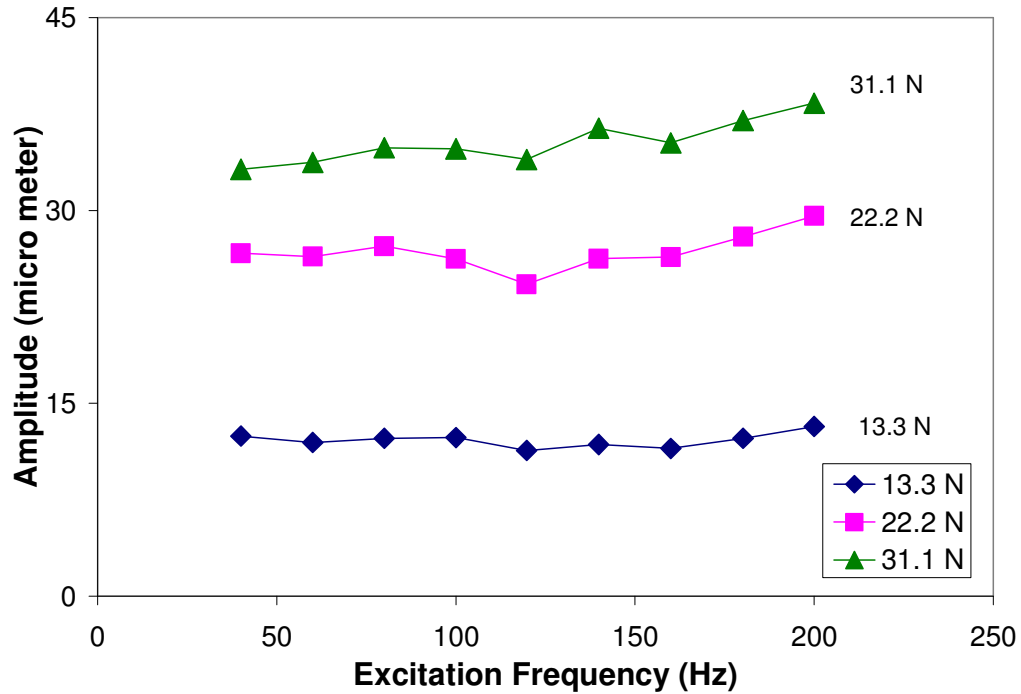
Figure 51 FB amplitude of motion versus excitation frequency for all load cases with shaft at 22°C (38.125 mm shaft, C_{nom} = 22.9 μm).

Figure 52 thru Figure 54 show the FB amplitude of motion versus frequency for all shaft temperatures at 13.3 N, 22.2 N and 31.1 N of dynamic load, respectively. Note the increase in displacement magnitudes with temperature for the specific load cases. The dynamic displacement magnitudes for the 13.3 N load with temperature increases significantly more than the other two load cases.
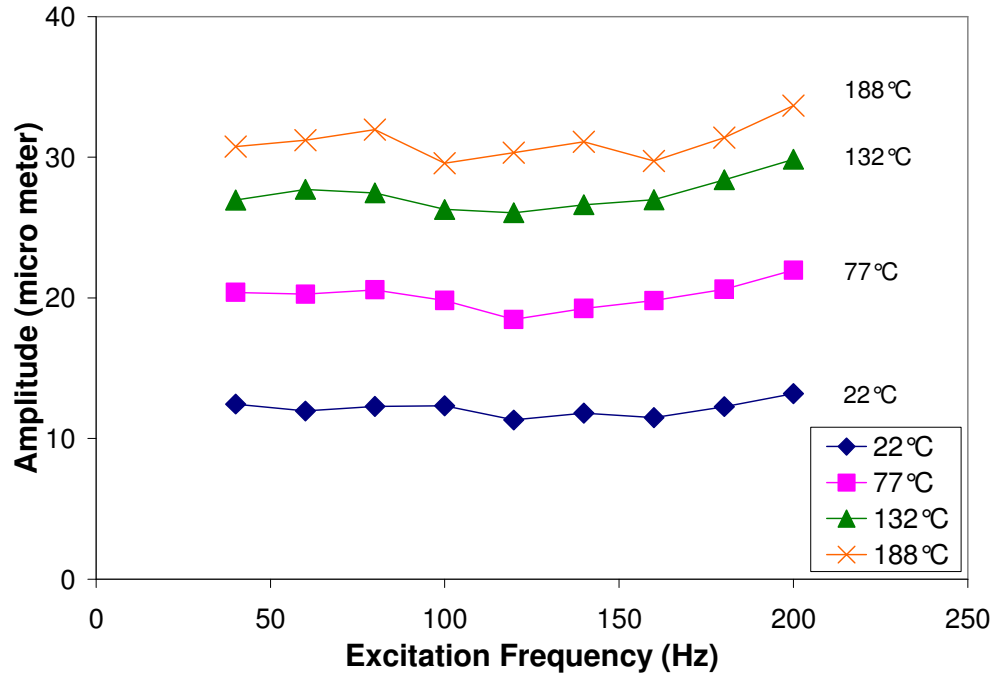
Figure 52 FB amplitude of motion versus excitation frequency for 13.3-N load case at all test shaft temperatures (38.125 mm shaft, C_{nom} = 22.9 μm).
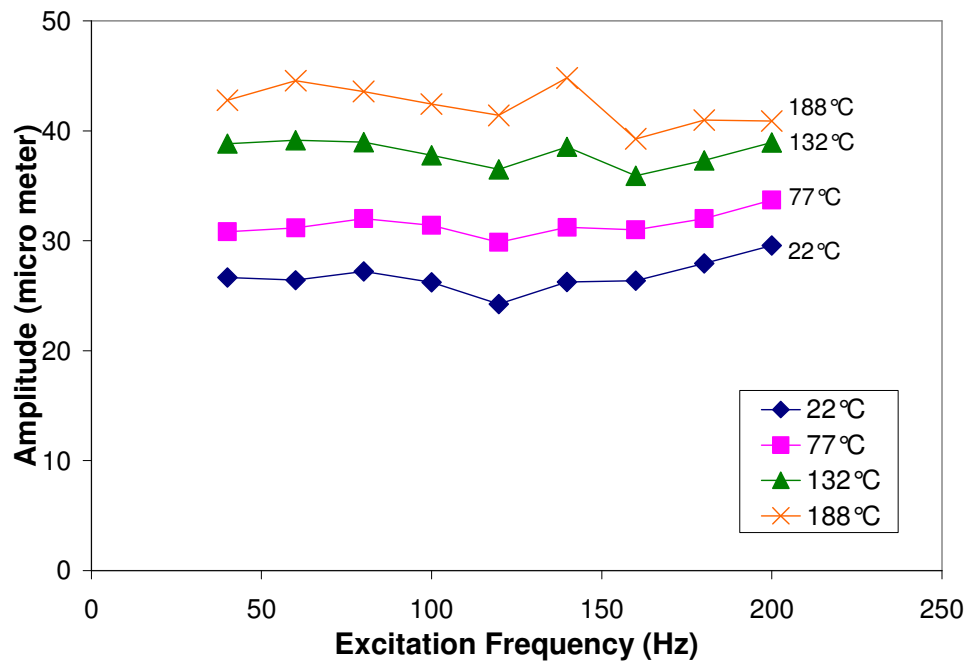
Figure 53 FB amplitude of motion versus excitation frequency for 22.2-N load case at all test shaft temperatures (38.125 mm shaft, C_{nom} = 22.9 μm).
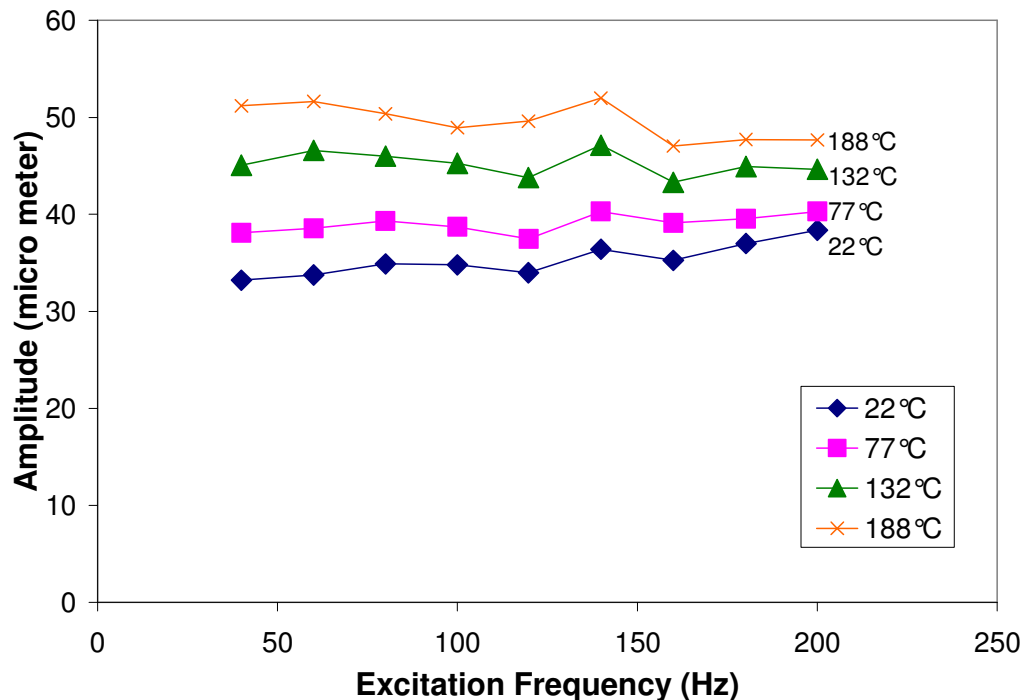
Figure 54 FB amplitude of motion versus excitation frequency for 31.1-N load case at all test shaft temperatures (38.125 mm shaft, C_{nom} = 22.9 µm).

Figure 55 shows the average of the displacement motion amplitudes over the frequency range for each load case versus shaft temperature. The figure illustrates the amplitude increase at increasing test shaft temperatures. The percentage increase in motion with temperature (from ambient to 188°C) for each dynamic load case is presented near its respective curve. Observe the markedly higher percentage increase in the average FB displacement for the 13.3 N load case (+ 156%) compared to the other load cases. This may indicate a region of distinct FB stiffness behavior for low magnitudes of dynamic load at room temperature. Recall that dynamic load amplitudes of $F_O \leq 8.9$ N (≤ 2 lbs) were deliberately avoided due to the distinct static deflection behavior within this low-load amplitude range. Evidently, as the shaft temperature increases, the FB stiffness due to the 13.3 N dynamic load experiences the most significant decrease compare to the other loads.
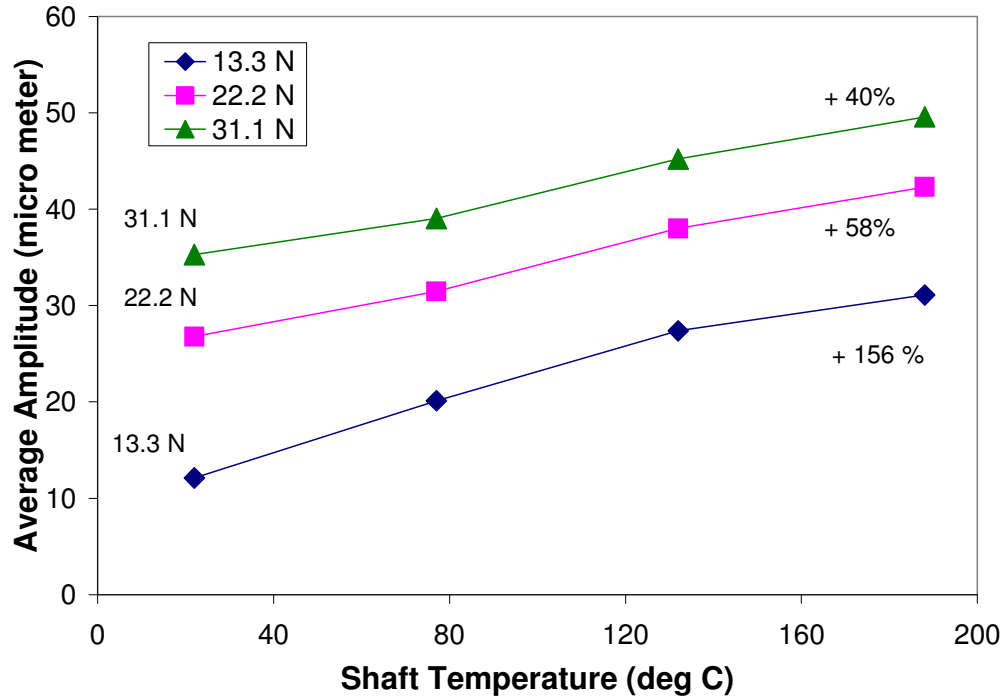
Figure 55 Average FB amplitude of motion versus shaft temperature for all loads (38.125 mm shaft, C_{nom} = 22.9 μm).

Parameter Identification

The above experimental data is imported into the analysis program forwarded by Rubio and San Andrés [19]. The program provides estimated FB structural coefficients.

FB Structural Stiffness

Analysis of the structural stiffness data indicates that the dynamic stiffness does not remain constant with excitation frequency. The stiffness data reported in this section are the average values of the three trials (see Appendix F) for the respective load cases.

Figure 56 shows $K(\omega) = \mathrm{Re}[(F - M\ddot{x})/x]$, i.e., stiffness, versus excitation frequency for all the load cases at T_S = 22°C (ambient conditions). Here, M is the FB mass and $K(\omega)$ is the frequency-dependent FB stiffness. Assuming the same system mass (M) allows quick estimation of the stiffness for each dynamic load case.

Observation of these curves indicates the bearing is stiffest for the 13.3 N load case at room temperature. However, a change occurs as the temperature increases. Figure 57 through Figure 59 show the FB structural stiffness for the load cases with the shaft temperature at 77°C, 132°C and 188°C, respectively. In these latter figures, the results show a clear trend that the FB stiffness increases as the amplitude of dynamic load increases. All of these figures indicate that FB stiffness is frequency dependent. The stiffness stays relatively constant up to 100 Hz and begins to increase throughout the range of excitation frequency.

The apparent shift from the lightly loaded region to the moderately loaded region with shaft temperature, as described in the experimental displacement results above, causes the different stiffness trend at room temperature than the other temperatures. The investigator premises that if dynamic load amplitudes $F_O \leq 8.9$ N had been tested that the resulting stiffness magnitudes would have been exceedingly larger than that of the 13.3 N case.
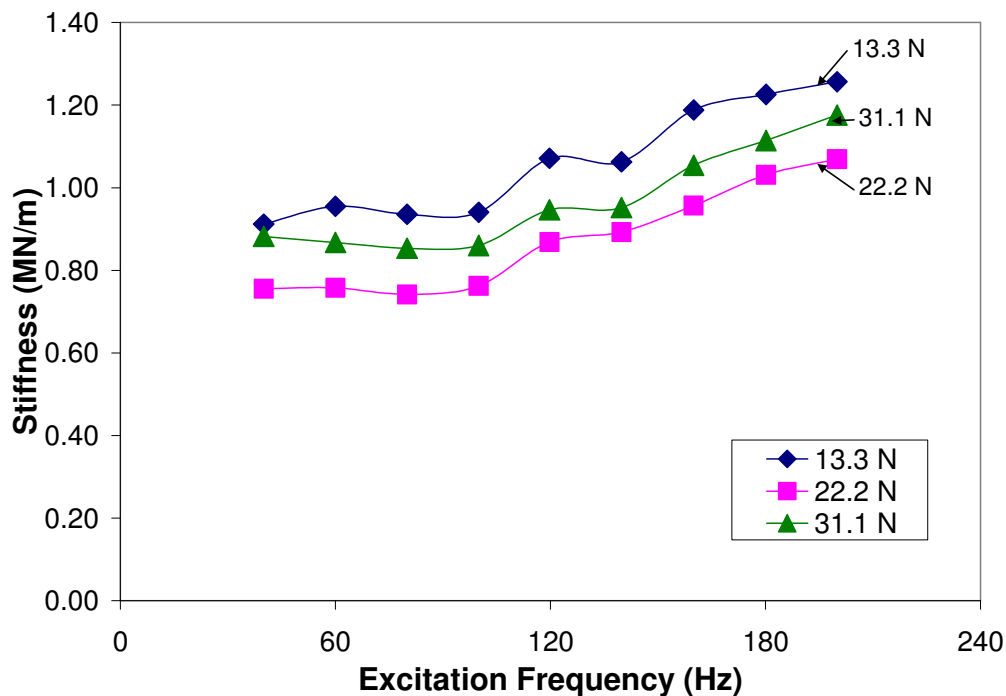
Figure 56 FB stiffness versus excitation frequency for all test loads at T_S = 22°C (38.125 mm shaft, C_{nom} = 22.9 μm).
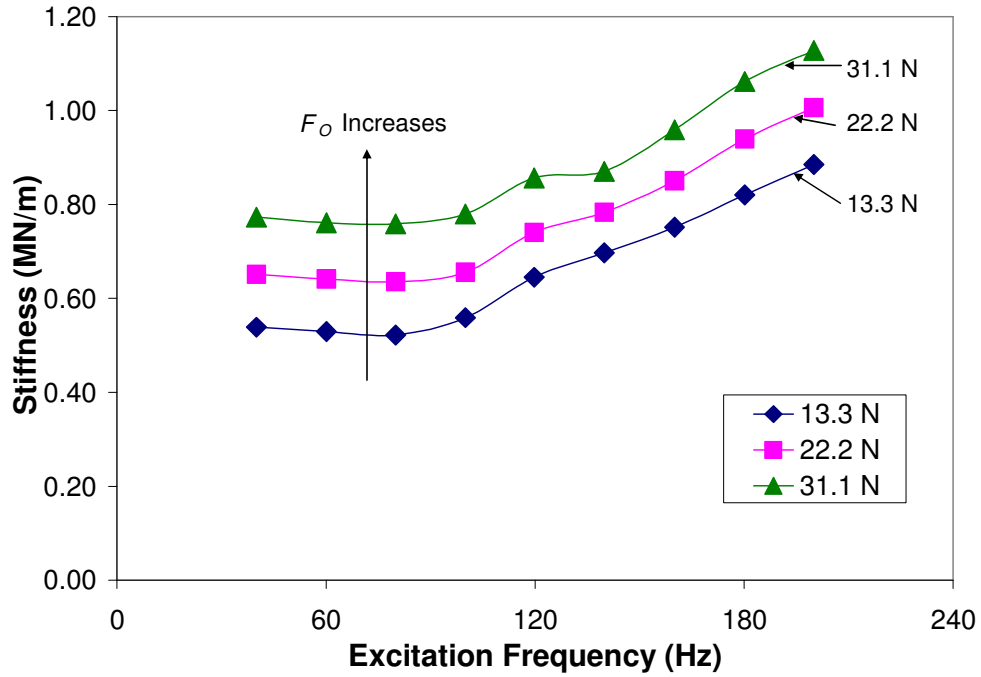
Figure 57 FB stiffness versus excitation frequency for all test loads at T$_S$ = 77 °C (38.125 mm shaft, *C$_{nom}$* = 22.9 μm).
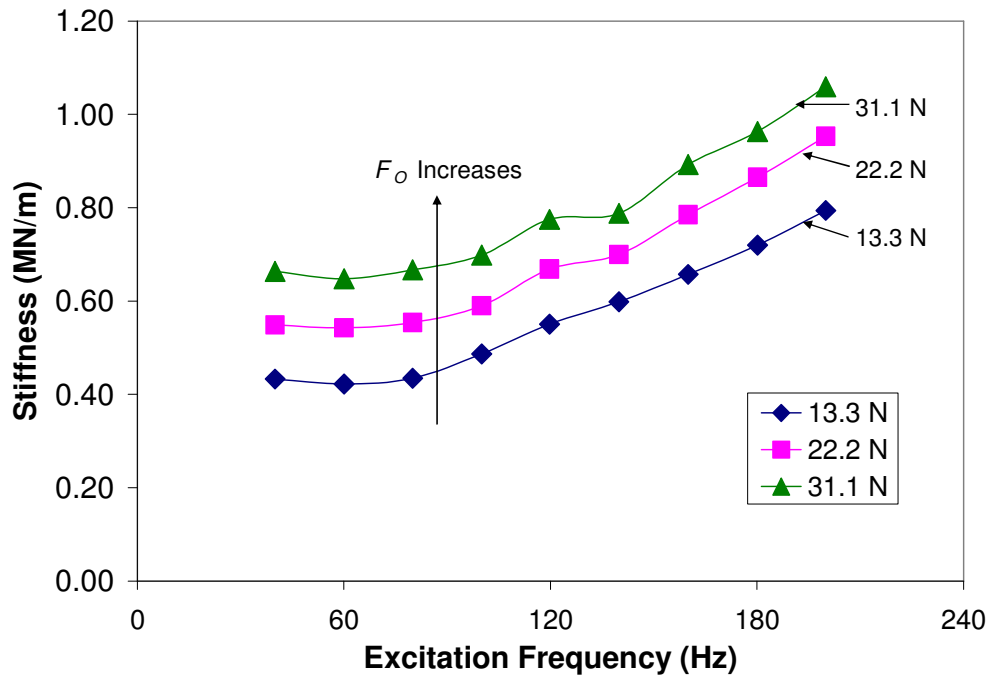
Figure 58 FB stiffness versus excitation frequency for all test loads at T$_S$ = 132 °C (38.125 mm shaft, *C$_{nom}$* = 22.9 μm).
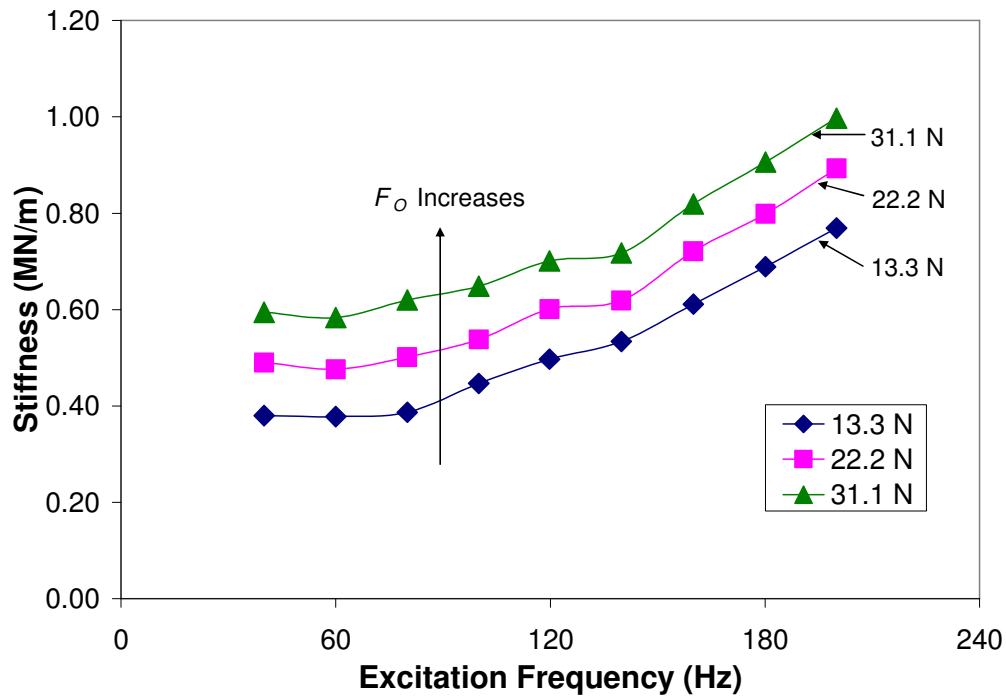
Figure 59 FB stiffness versus excitation frequency for all test loads at T_S = 188°C (38.125 mm shaft, C_{nom} = 22.9 μm).

By separating the stiffness data with respect to amplitude of dynamic load, a clear relationship between stiffness and shaft temperature becomes evident. Figure 60 shows the FB stiffness versus excitation frequency for the 13.3 N load case with the shaft at the four test temperatures. The stiffness magnitudes indeed decrease as shaft temperature increases. Figure 61 and Figure 62 show that the same behavior occurs for the 22.2 N and 31.1 N amplitudes of dynamic load cases, respectively. Note, however, the large decrease in stiffness between the 22°C and 77°C curves for the 13.3 N load case. This large decrease is not evident for the other load cases.
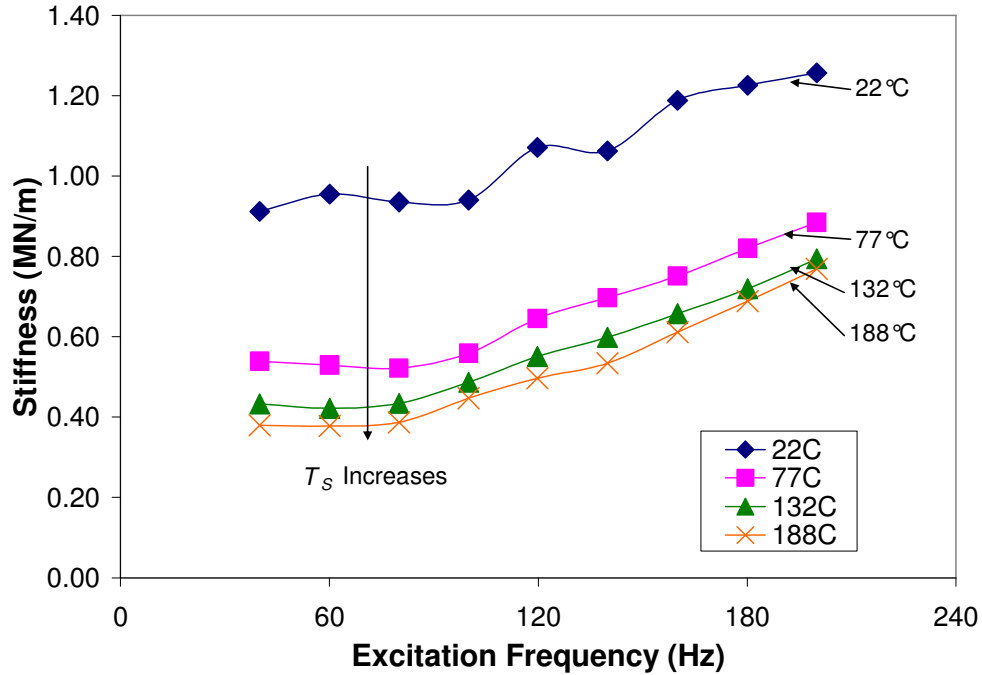
Figure 60 FB stiffness versus excitation frequency for the F_O = 13.3 N load case with test shaft at increasing temperature (38.125 mm shaft, C_{nom} = 22.9 µm).
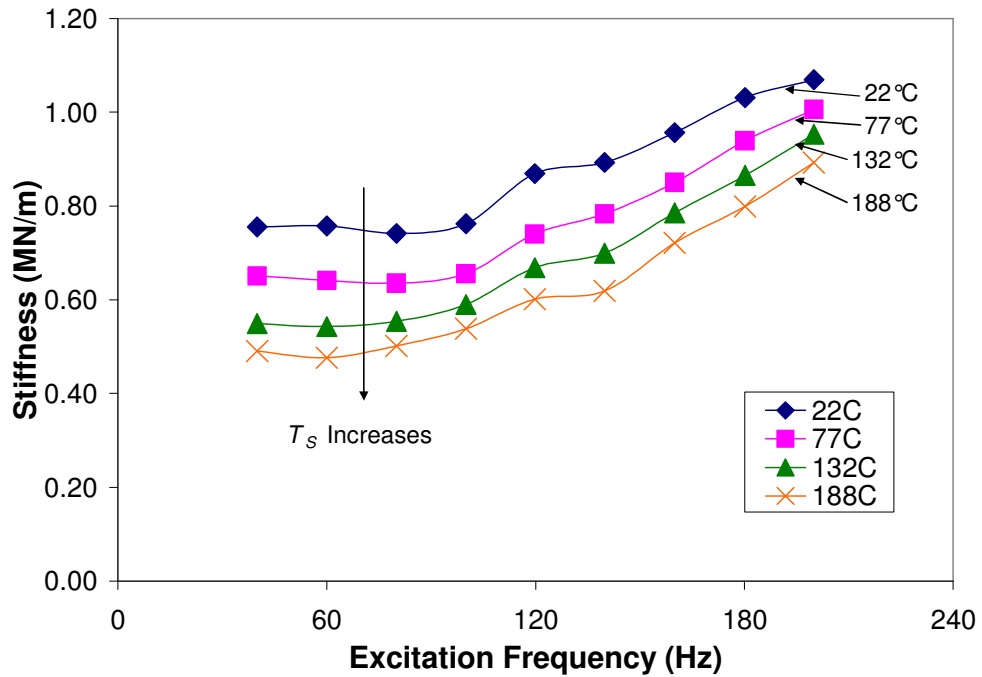
Figure 61 FB stiffness versus excitation frequency for the F_O = 22.2 N load case with test shaft at increasing temperature (38.125 mm shaft, C_{nom} = 22.9 µm).
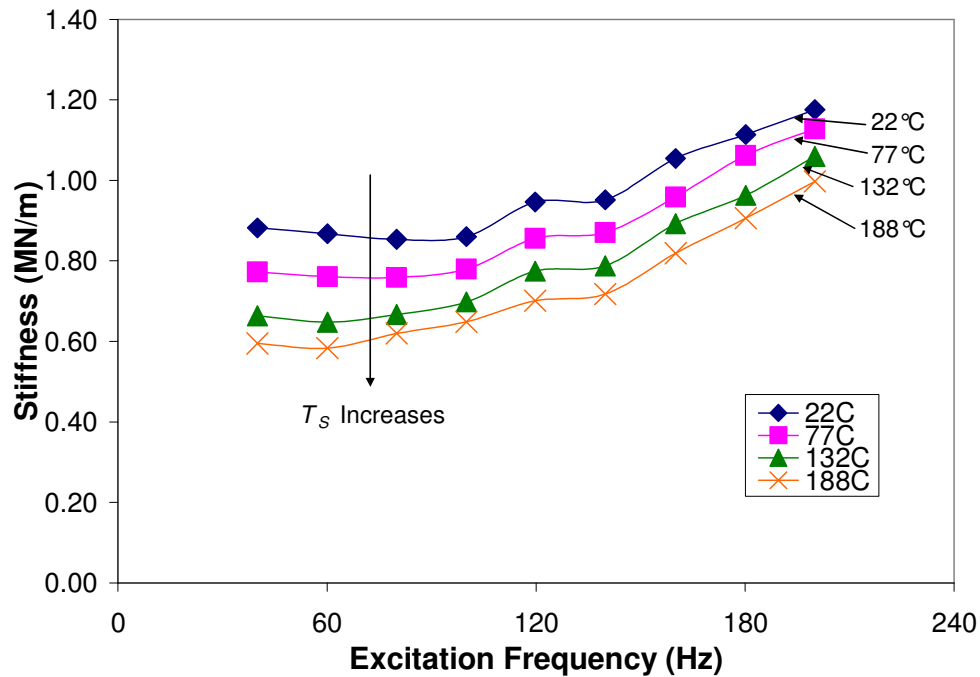
Figure 62 FB stiffness versus excitation frequency for the F_O = 31.1 N load case with test shaft at increasing temperature (38.125 mm shaft, C_{nom} = 22.9 μm).

This section showed, from the real part of the mechanical impedance, results of the FB dynamic structural stiffness as a function of the amplitude of dynamic load, excitation frequency, and test shaft temperature. The results indicate that FB stiffness increases by as much as 57% with amplitude of dynamic load from F_O = 13.3 N to F_O = 31.1 N (at ω = 40 Hz). The one exception is for the case when T_S = 22°C where the stiffness for 13.3 N load is the highest (see Figure 56). Experimental results show that as the test shaft temperature increases, the FB stiffness decreases by 58% for the range of test temperatures from T_S = 22°C to T_S = 188°C (at ω = 40 Hz). Finally, bearing stiffness experiences an increase with excitation frequency above 100 Hz. Table 17 summarizes the percent increases experienced in bearing stiffness for the test conditions for the range of excitation frequencies from ω = 40 Hz to ω = 200 Hz.

Table 17 Percentage increase in experimental FB structural stiffness with excitation frequency from ω = 40 Hz to ω = 200 Hz for all load amplitudes and shaft temperatures

Dynamic Load Amplitude, F_O (N)	Bearing Stiffness Percent Increase (%) with Excitation Frequency			
	$T_S = 22°C$	$T_S = 77°C$	$T_S = 132°C$	$T_S = 188°C$
13.3	38	64	83	103
22.2	42	54	74	82
31.1	33	46	60	68

FB Dynamic Structural Stiffness Compared to Static Structural Stiffness

The FB static stiffness is generally higher than the dynamic stiffness due to the friction interaction between contacting surfaces in the former case. In fact, in [14] the authors show that introducing a dynamic excitation in the direction of an applied static load reduces the FB stiffness as compared to static loading without excitation. The experimentally derived static stiffness results from Section V are compared to the dynamic stiffnesses obtained at 40 Hz excitation frequency. The static stiffness data are for the 45° bearing orientation only.

Figure 63 shows the experimental FB stiffness derived from static load measurements and the dynamic stiffness from shaker experiments versus FB deflection. The dashed and dotted lines represent the static stiffnesses for 22°C and 188°C, respectively. The other four lines correspond to dynamic stiffness data taken at the four test shaft temperatures, respectively. Each of the three data points of a line corresponds to the deflection due to 13.3 N, 22.2 N, and 31.1 N of dynamic load at 40 Hz excitation frequency. At 12.45 μm FB deflection, the static and dynamic stiffnesses match closely for the 13.3 N dynamic load at room temperature. At larger deflections, however, the static stiffness is larger than the dynamic stiffness.

Table 18 shows the static and dynamic deflections and the corresponding bearing stiffnesses for the tests at 22°C and 188°C. Also, the ratio of the static stiffness to the dynamic stiffness for the respective conditions is presented for each pair. This ratio

increases with temperature and amplitude of motion (dynamic load amplitude), signifying that the static stiffness is consistently larger in magnitude than the dynamic stiffness for test conditions.
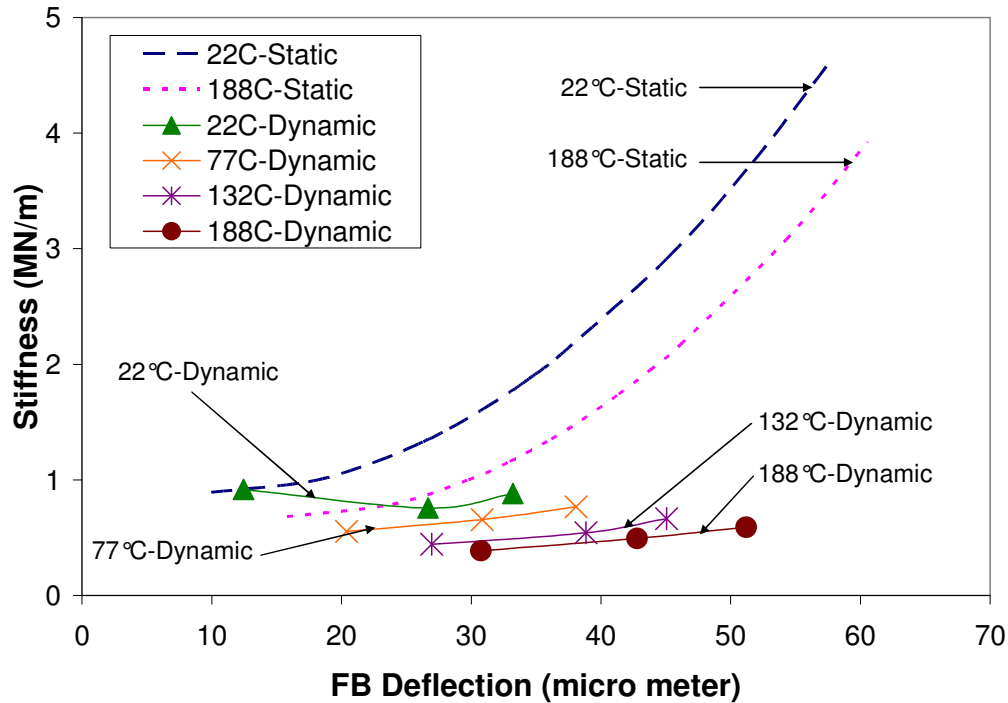
Figure 63 Static (22°C and 188°C) and dynamic (at increasing T_S) FB stiffness versus deflection for all loads (38.125 mm shaft, C_{nom} = 22.9 μm).

Table 18 Static and dynamic stiffnesses for corresponding FB deflections with shaft at 22°C and 188°C (38.125 mm shaft, C_{nom} = 22.9 μm)

T_S (°C)	Static		Dynamic		Ratio
	Deflection (μm)	Stiffness (MN/m)	Deflection (μm)	Stiffness (MN/m)	
	9.56	0.893	12.45	0.917	0.97
22	26.31	1.33	26.68	0.757	1.8
	33.26	1.78	33.21	0.882	2.0
	30.70	1.60	30.76	0.387	4.1
188	43.00	2.70	42.79	0.494	5.5
	51.71	3.75	51.20	0.591	6.3

Figure 64 shows the same static and dynamic FB stiffness data as a function of load amplitude. The dynamic stiffness curves for the 77°C, 132°C, and 188°C shaft

temperatures increase linearly with amplitude of dynamic load. The dynamic stiffness of the 13.3 N load at 22°C lies close to the static stiffness curve at the same shaft temperature. Increasing the amplitude of the dynamic load to 22.2 N decreases the stiffness, and increasing it further to 31.1 N increases the stiffness. The dynamic stiffness curve for 22°C is the only data that displays this peculiar behavior. This reported stiffness is the average stiffness of three experimental trials. This behavior consistently occurs in three independent (non-sequential) tests with a standard deviation of 0.52% of the reported value (See Appendix F). This repeated behavior may either be due to the regional low- and moderate-load amplitude FB performance or related to the test setup.
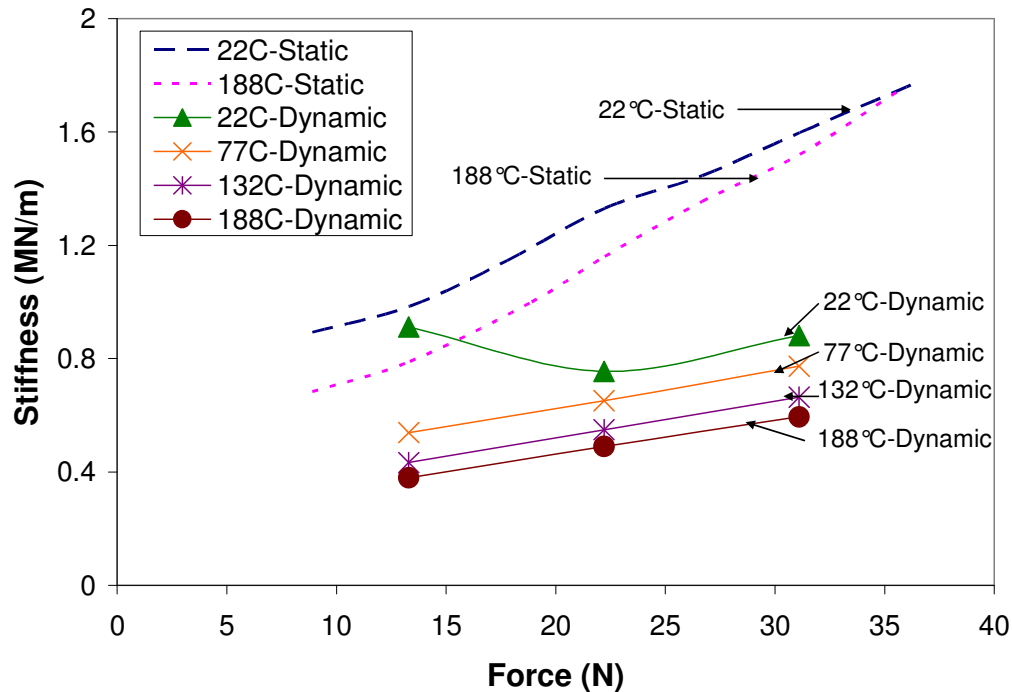
Figure 64 Static (22°C and 188°C) and dynamic (at increasing T_S) FB stiffness versus applied force amplitude (38.125 mm shaft, C_{nom} = 22.9 μm).

Mechanism that Leads to Increasing Structural Stiffness with Excitation Frequency

The frequency dependent structural stiffness differs from results in [19] and agrees with findings in [14,18]. Observation of time domain data provides an

explanation of this result. Figure 65 shows the load versus FB displacement loop for the 22.2 N load at 40 Hz excitation frequency. Note the circled regions where the FB changes direction of motion with the change in load direction. At 40 Hz these regions of the curve seem sharp, which indicates a quick reversal of motion with change of force direction.
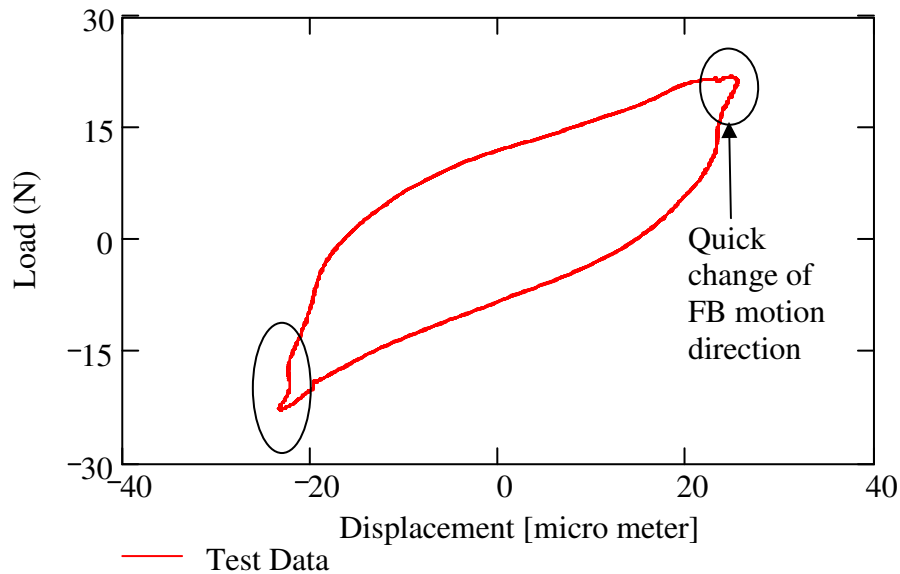
Figure 65 Time domain dynamic load versus FB displacement with shaft at 22°C (F_O = 22.2 N, 40 Hz) showing no stick-slip (38.125 mm shaft, C_{nom} = 22.9 μm).

Figure 66 shows the load versus FB displacement loop for the 22.2 N load at 100 Hz excitation frequency. The circled regions of the curve appear less sharp (more vertical) than those of the 40 Hz case, which indicates an increase in stiffness. Recall that the stiffness remains nearly constant up to 100 Hz and begins to increase. Finally, Figure 67 shows the loop at 200 Hz excitation frequency, which evidences a marked increase in the length of the vertical portion of the circled regions.

This vertical region denotes nearly infinite stiffness, i.e., continued loading or unloading with little displacement (sticking). The vertical regions become progressively larger at frequencies above 100 Hz. This region is where the stick-slip phenomenon occurs (as indicated by the arrows in Figure 67).
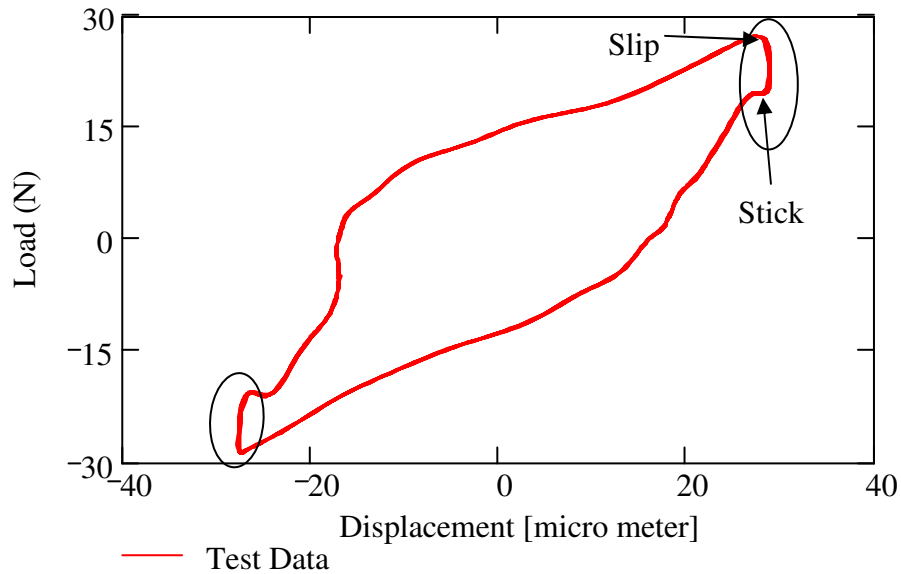
Figure 66 Time domain dynamic load versus FB displacement with shaft at 22 °C (F_O = 22.2 N, 100 Hz) showing increased amount of stick-slip compared to 40 Hz case (38.125 mm shaft, C_{nom} = 22.9 µm).
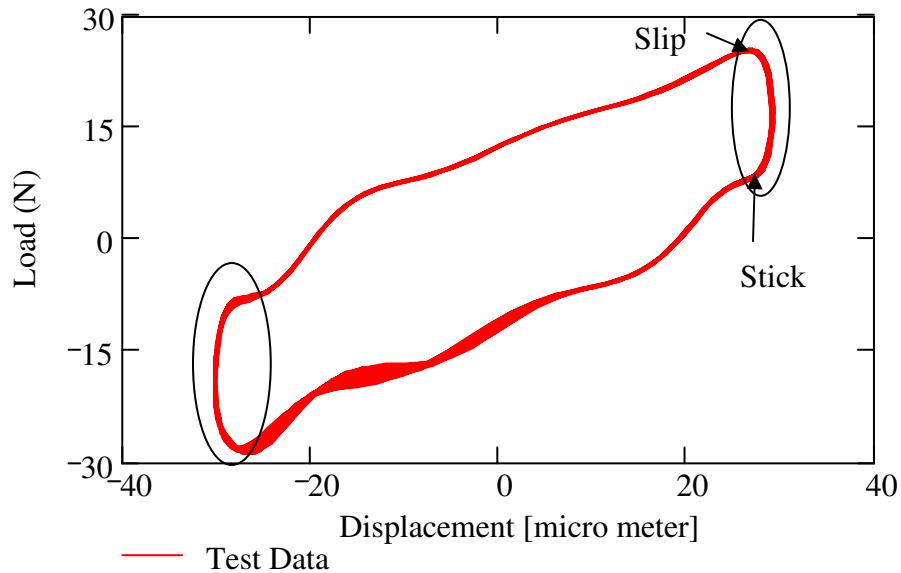
Figure 67 Time domain dynamic load versus FB displacement with shaft at 22 °C (F_O = 22.2 N, 200 Hz) showing further increase in amount of stick-slip compared to lower excitation frequencies (38.125 mm shaft, C_{nom} = 22.9 µm).

Equivalent Viscous Damping

The imaginary part of the mechanical impedance, presented in Equation (37), provides a means by which to determine the FB equivalent viscous damping (C_{eq}). Given the FB mass (M), the measured amplitude of dynamic load and the resultant FB displacement are used to calculate the viscous damping (C_{eq}) as

$$C_{eq} = \frac{\text{Im}[(F_O - M\ddot{x})/x]}{\omega} \tag{38}$$

Figure 68 shows that C_{eq} decreases with excitation frequency. As indicated in the figure, C_{eq} decreases with increasing loads for this testing. Recall from Equation (30) that $C_{eq} \propto 1/X$ and $C_{eq} \propto 1/\omega$. Since the test frequencies are sufficiently below any system natural frequency at 260 Hz (see Appendix G), the phase angle $\theta << 90°$, and the numerator in Equation (30) remains a fraction of F_O. Also, the displacement magnitudes for the nominal dynamic loads are large enough such that the denominator is large enough to reduce C_{eq} for each successive load.

Since the displacement magnitudes increase with temperature, C_{eq} must also decrease with temperature. Figure 69 shows C_{eq} versus excitation frequency for increasing shaft temperatures for the 13.3 N load case. Indeed, the expected trend is clearly shown in the figure. Figure 70 and Figure 71 show that this trend is also evident for the 22.2 N and 31.1 N load cases, respectively.
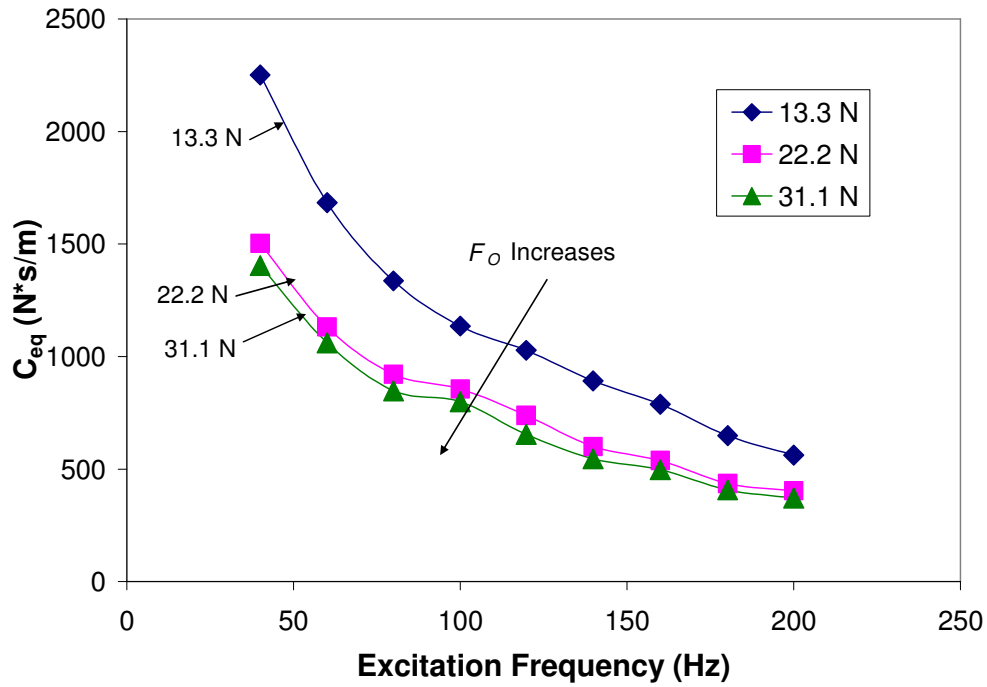
Figure 68 Equivalent viscous damping versus excitation frequency at T_S = 22°C decreasing as F_O increases (38.125 mm shaft, C_{nom} = 22.9 μm).
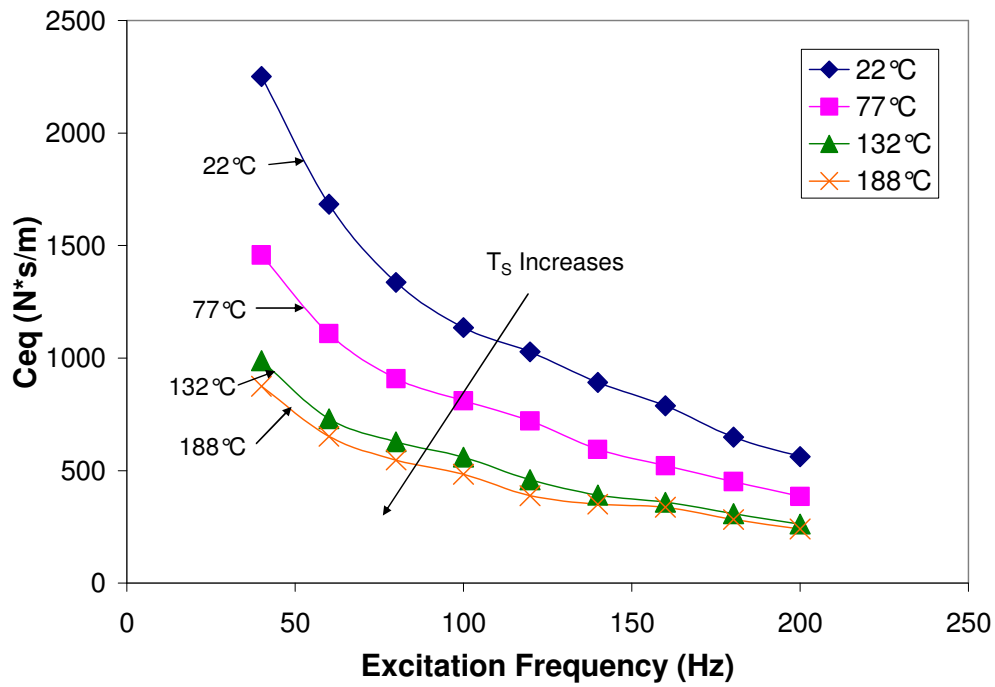
Figure 69 Equivalent viscous damping versus excitation frequency for the 13.3 N load case decreasing with increasing shaft temperature (38.125 mm shaft, C_{nom} = 22.9 μm).
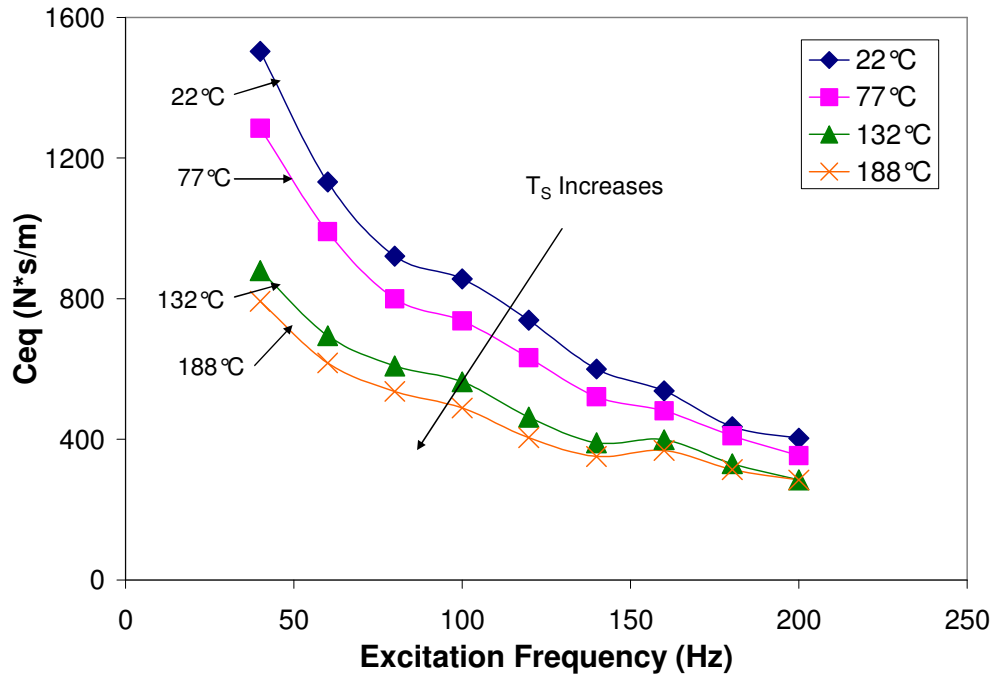
Figure 70 Equivalent viscous damping versus excitation frequency for the 22.2 N load case decreasing with increasing shaft temperature (38.125 mm shaft, C_{nom} = 22.9 μm).
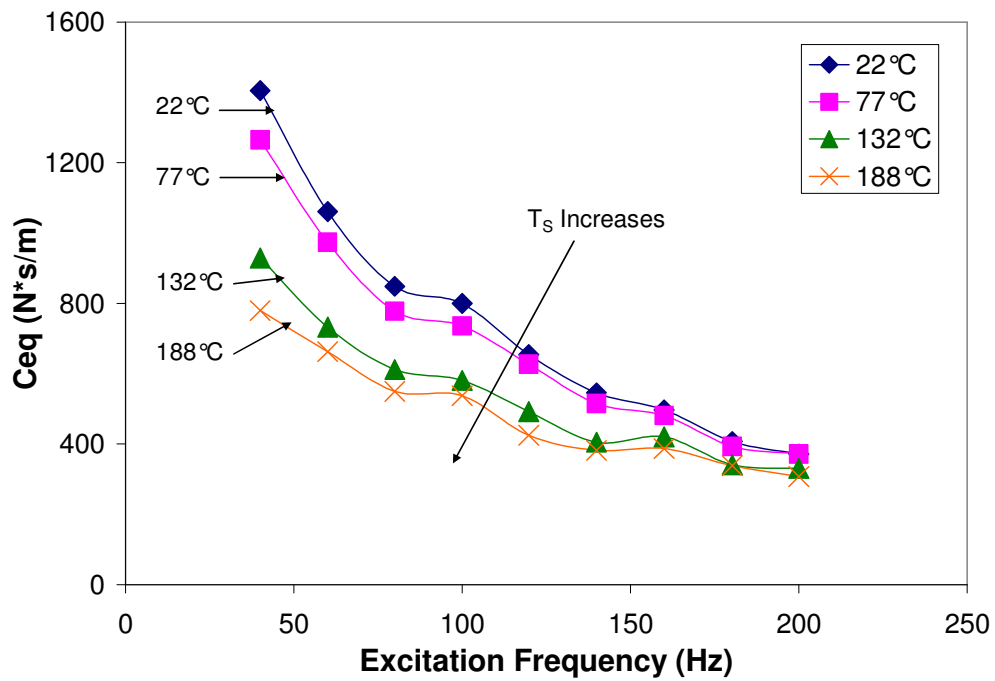
Figure 71 Equivalent viscous damping versus excitation frequency for the 31.1 N load case decreasing with increasing shaft temperature (38.125 mm shaft, C_{nom} = 22.9 μm).

Dry Friction Force

Rubio and San Andrés [19] also provide the derivation for the dry-friction force F_{dry} from the dissipated energy = external work approach. The final equation given is

$$F_{dry} = \frac{F_O \pi \sin\theta}{4} .$$
(31)

Figure 72 shows the calculated frictional force versus frequency for all loads at 22°C. As expected, the larger the amplitude of applied dynamic load, the larger the frictional force. The same trends and magnitudes of friction force occur for the FB at the other test temperatures.
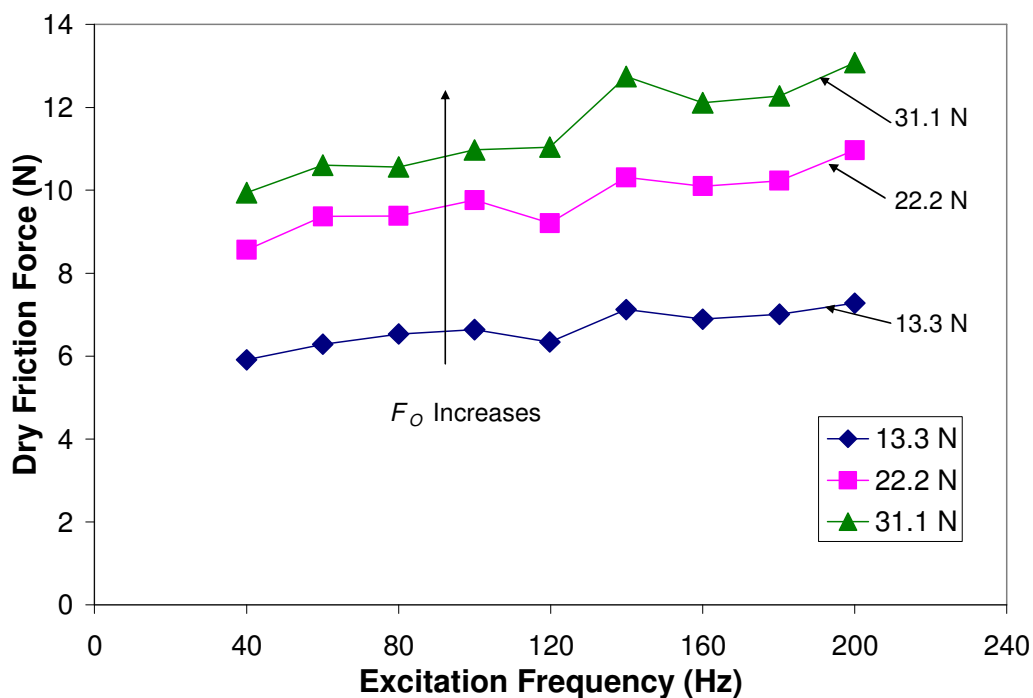
Figure 72 Dry friction force versus excitation frequency for all loads at 22°C (38.125 mm shaft, C_{nom} = 22.9 µm).

Figure 73 shows the average F_{dry} for each load through the frequency range versus the test temperature. Note that the frictional force varies little (+/- 1 N) with shaft temperature for each load case.
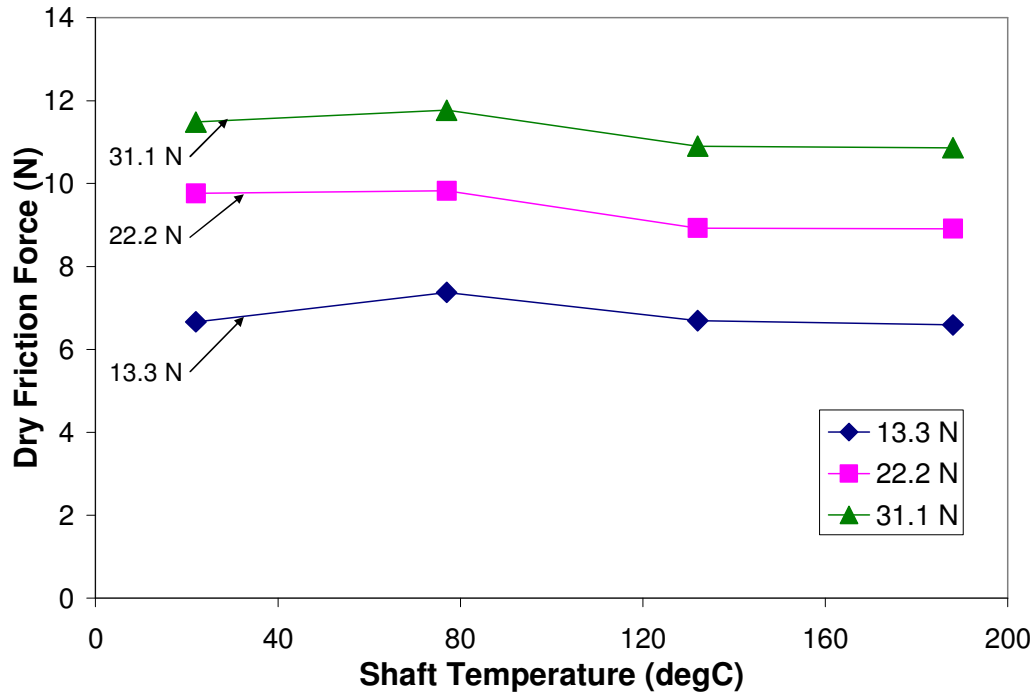
Figure 73 Average dry friction force versus shaft temperature for all load cases (38.125 mm shaft, C_{nom} = 22.9 µm).

Dry Friction Coefficient

Finally, the calculated dry friction coefficient is simply

$$\mu_f = \frac{F_{dry}}{F_O}. \tag{32}$$

Figure 74 shows the friction coefficient versus excitation frequency for all loads at 22°C. The friction coefficient decreases while increasing the amplitude of dynamic load for this test condition. The friction coefficient for the 13.3-N load varies from 0.45 to 0.55 (22% increase), from 0.39 to 0.50 (28% increase) for the 22.2-N load, and from 0.32 to 0.42 (31% increase) for the 31.1-N load over the excitation frequency range.

This result is opposite of the findings Rubio and San Andrés reported in [19], where μ_f increased with amplitude of dynamic load. Also, the magnitudes of the coefficient of friction from the respective investigations differ. That is, in [19] the coefficient ranged from μ_f = 0.05 (at F_O = 4 N) to μ_f = 0.2 (at F_O = 20 N), whereas in the

current investigation, the coefficient ranges from 0.36 (at F_O = 31.1 N) to 0.50 (at F_O = 13.3 N).
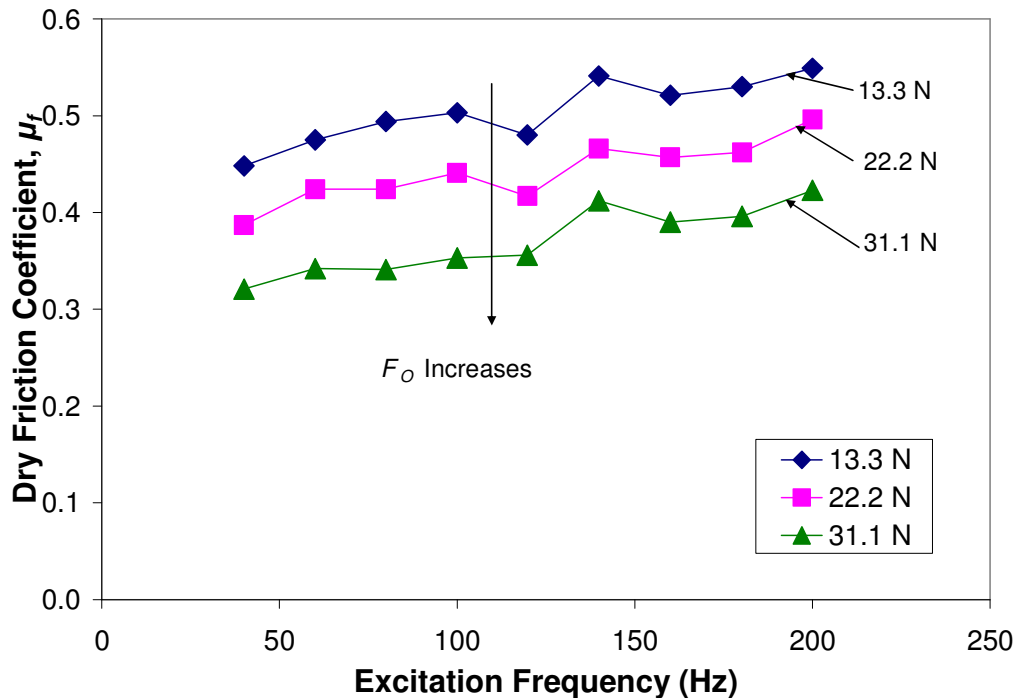
Figure 74 Dry friction coefficient versus excitation frequency for all load cases at 22°C decreasing with amplitude of F_O (38.125 mm shaft, C_{nom} = 22.9 μm).

Figure 75 through Figure 77 show the dry friction coefficient (μ_f) versus excitation frequency for the 13.3 N, 22.2 N and 31.1 N load cases, respectively. The three plots show a steady dry-friction coefficient for the amplitudes of dynamic load and increasing with frequency. The curves for each temperature at each load seem to increase at the same rate.

The μ_f data for F_O = 13.3 N, for example, are arranged according to shaft temperature. An average is taken over the range of excitation frequencies to provide an average μ_f at a certain shaft temperature. Subsequently, these averages at discrete shaft temperatures are averaged to provide an average μ_f for particular amplitude of dynamic load over the shaft temperature range. This method for obtaining the average μ_f is performed for all load cases.
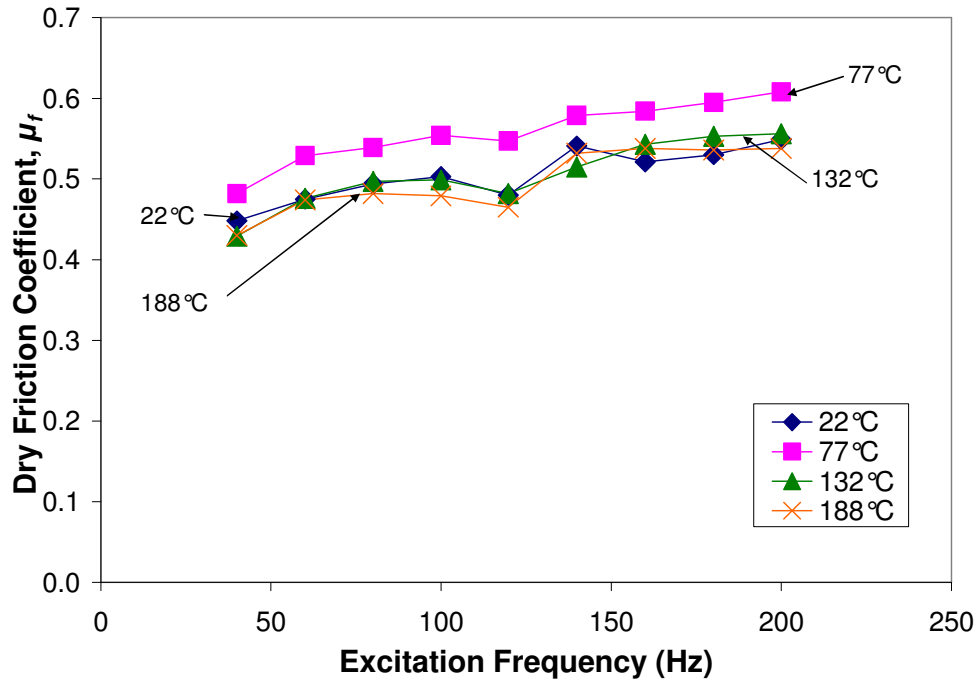
Figure 75 Dry friction coefficient versus frequency for 13.3 N load case at all T_S (38.125 mm shaft, C_{nom} = 22.9 µm).
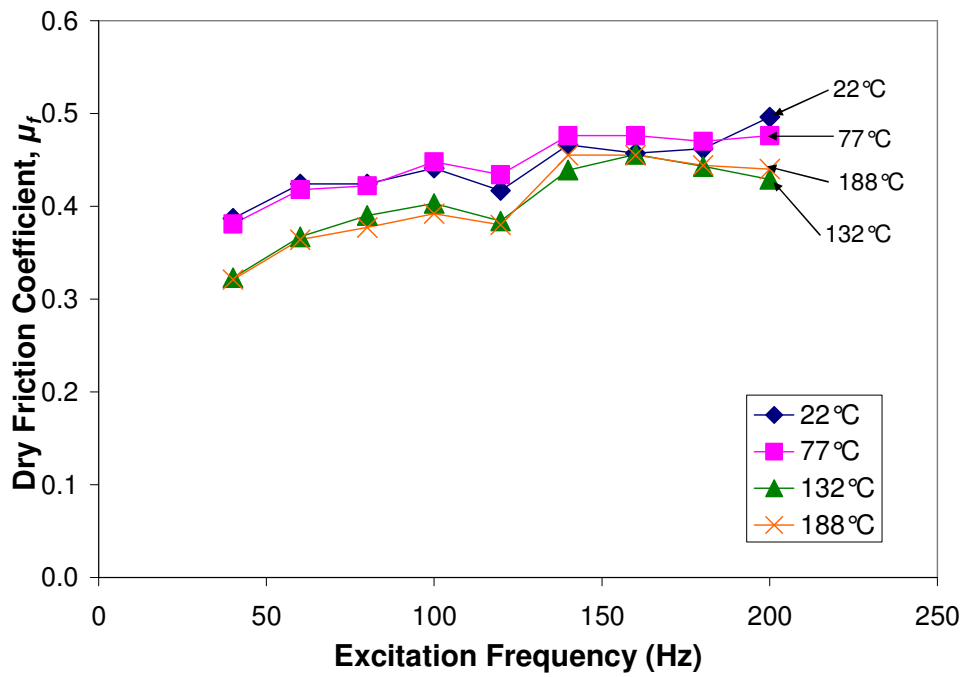
Figure 76 Dry Friction coefficient versus frequency for 22.2 N load case at all T_S (38.125 mm shaft, C_{nom} = 22.9 µm).
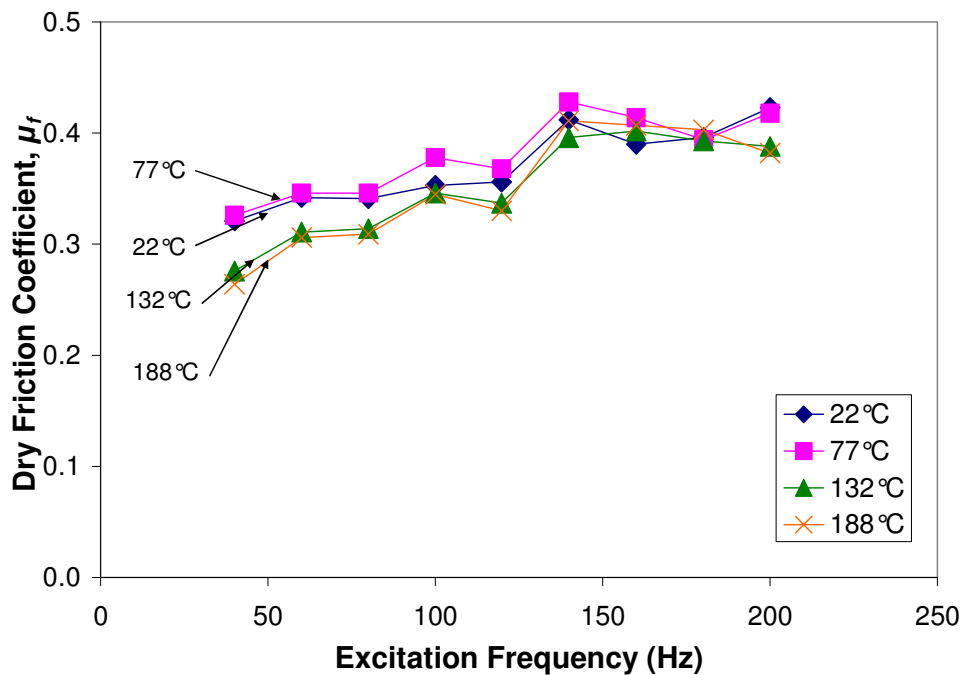
Figure 77 Dry Friction coefficient versus frequency for 31.1 N load case at all T_S (38.125 mm shaft, C_{nom} = 22.9 μm).

The averages of the dry friction coefficient (μ_f) for the frequency range at all test conditions show distinctive trends. Table 19 shows the results of these calculations. For instance, the average μ_f for the 13.3 N load over the frequency range for T_S = 22°C is 0.50 with a standard deviation of 0.034 (6.74% deviation error). The other values of μ_f for the respective shaft temperatures are given in Table 19.

Figure 78 shows the average dry friction coefficients versus T_S for all load cases. It is clear that the friction coefficient decreases with increasing load. Also, the friction coefficients appear to stay relatively constant for each load case as temperature increases. For instance, the average μ_f over the T_S range for F_O = 13.3 N is 0.52 with a standard deviation of 0.028 (5.4% deviation error). The results for the 22.2 N and 31.1 N load cases are found in the same manner, and the tabulated data are found in Appendix H.

Table 19 Average and standard deviation estimation for dry friction coefficient as a function of excitation frequency and shaft temperature (F_O=13.3N, 38.125 mm shaft, C_{nom} = 22.9 μm)

Excitation Frequency (Hz)	Dry Friction Coefficient, μ_f				
	22°C	77°C	132°C	188°C	
40	0.448	0.482	0.429	0.430	
60	0.475	0.529	0.476	0.474	
80	0.494	0.539	0.497	0.482	
100	0.503	0.554	0.499	0.479	
120	0.480	0.547	0.482	0.465	
140	0.541	0.579	0.515	0.532	
160	0.521	0.584	0.543	0.538	
180	0.530	0.595	0.553	0.536	Average μ_f over the
200	0.549	0.608	0.556	0.538	T_S Range
Average μ_f	0.50	0.56	0.51	0.50	0.52
Standard Deviation	0.034	0.039	0.041	0.040	0.028
Percent Error	6.7%	7.0%	8.2%	8.0%	5.4%
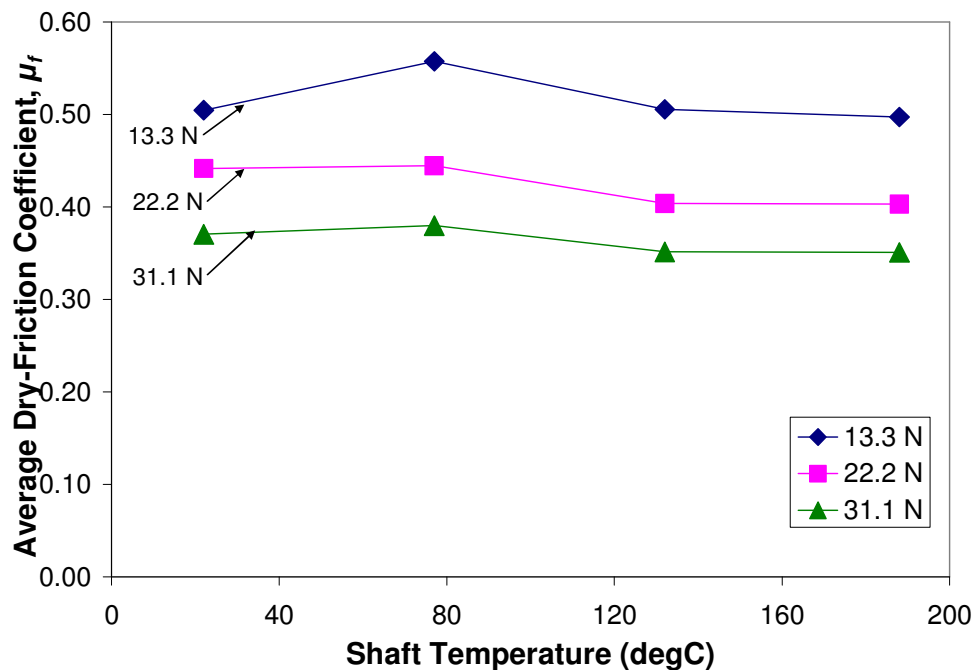
Figure 78 Average dry-friction coefficient versus shaft temperature for all test loads (38.125 mm shaft, C_{nom} = 22.9 μm).

VIII CONCLUSIONS

Oil-free bearing technology is to replace oil-lubricated systems, which are more expensive and more difficult to maintain. Elimination of oil pumps, filters and reservoirs offers benefits such as reduction in size and weight. Recent developments in solid lubricants may make GFB operation and application limited only by the physical capabilities of the rotor [1]. The compliant structure provides resistance to rotor excursions through structural stiffness and Coulomb damping among its contacting members. It is paramount to characterize the FB structural stiffness and damping through experiments and to subsequently provide predictive tools that accurately model FB behavior.

Static load tests conducted for four bearing angular orientations on two shafts of differing diameter provide force versus deflection data. A data reduction scheme divides a force versus deflection data into three regions and uses a cubic polynomial to fit the outer portions of the force curve. The derivative of this curve fit provides an anti-symmetric stiffness versus deflection curve with respect to bearing orientation. Results indicate that a load directed towards the welded end of a bump strip (at 270° bearing orientation, for instance) experiences more stiffness than a load towards the free end (90° bearing orientation), thus the anti-symmetric stiffness about the bearing center. As the shaft temperature increases the FB static stiffness reduces as much as 70%, depending on load application direction, for a certain amount of deflection indicating an increase in radial clearance.

Static deflection and stiffness results are compared to results obtained using an existing model forwarded in [17]. The investigation introduces two changes to the model. A cubic polynomial fits predicted force versus deflection curves used to derive an estimated stiffness. Also, a deflection adjustment, x_o, is introduced to improve the direction-dependent structural stiffness agreement between experiments and predictions. The current model does not properly indicate null stiffness for FB deflections within the

clearance. This deficiency is not corrected at the time of this written thesis. Nevertheless, the predicted and experimental results show excellent agreement.

The current research yields a method to predict the behavior of the initial clearance between the shaft and the FB as the system temperature increases. Experiments determine the coefficients of thermal expansion (CTEs) of the AISI 4140 steel shaft ($\alpha_{S,E}$ = 6.98 µm/m°C) and the AISI 304 stainless steel FB housing ($\alpha_{B,E}$ = 17.28 µm/m°C). The result for the stainless steel FB housing match the theoretical value ($\alpha_{B,T}$ = 17.3 µm/m°C); however, experiments under predict the theoretical CTE for the steel shaft ($\alpha_{S,T}$ = 12.2 µm/m°C). This discrepancy between the experimental and theoretical CTEs for the steel shaft is explained by an axial thermal gradient within the shaft during tests. The axial thermal gradient along the shaft length is confirmed by an FEA analysis, as well as physical measurements. Both the theoretical and experimental CTEs indicate that the radial clearance increases over the temperature range. To ensure uniform heating of the test shaft, future research may involve shaft re-design or using a cartridge heater that is capable of axially heating the remainder of the shaft. Furthermore, using a test shaft material with $\alpha_S \gg \alpha_B$ may provide a decrease in clearance with temperature and, perhaps, even a mechanical preload of the bumps.

Shaker test experiments, while varying the amplitude of dynamic load, excitation frequency, and shaft temperature provide force, displacement and acceleration information for subsequent analysis. Time and frequency domain analysis of single frequency dynamic load test data render insight to the structural support behavior under a number of test conditions. The dynamic structural stiffness results indicate dependence upon all three variables tested. The real part of the mechanical impedance indicates that stiffness increases with excitation frequency. The increase in FB stiffness with excitation frequency is by a factor of two or less. Load versus deflection data in the time domain show that the effect of a stick-slip phenomenon increases the FB stiffness as the excitation frequency increases. For a given amplitude of dynamic load, as the shaft temperature increases, the FB stiffness decreases. The dynamic FB structural stiffness decrease by more than half for the F_O = 13.3 N dynamic load as the shaft

temperature increased from $T_S = 22°C$ to $T_S = 188°C$. For all tests, with the exception of the case for the smallest amplitude of dynamic load at ambient shaft temperature, the FB stiffness increased with amplitude of dynamic load. The largest increase in FB stiffness magnitude (57% increase) occurs for the $T_S = 188°C$ case as the amplitude of dynamic load increases from $F_O = 13.3$ N to $F_O = 31.1$ N.

The FB equivalent viscous damping decreases with amplitude of dynamic load and shaft temperature. Damping is also strongly dependent upon excitation frequency. However, tests at frequencies up to 420 Hz show two resonance peaks around 260 Hz, related to the FB mass, and 380 Hz (the shaft natural frequency), respectively, and damping remains evident throughout the frequency range. This indicates that the FB damping mechanism is not solely due to dry friction.

Results show that the dry friction coefficient increases slightly as a function of frequency and decreases as load increases. When the friction coefficient is averaged over a frequency range, results show that its magnitude is relatively constant with respect to shaft temperature. The reported average friction coefficients are 0.52, 0.42, and 0.36 for the increasing amplitudes of dynamic load, respectively. In [19] the friction coefficient increased with amplitude of dynamic load; also, the reported values were considerably lower, from 0.05 (at $F_O = 4$ N) to 0.2 (at $F_O = 20$ N).

This investigation yields a revamped test rig comprising a massive, rigid shaft support structure and a shaker that is mounted to the test facility ceiling. The current test set up provides repeatable data as presented herein. A modified DAQ program accurately and automatically saves test data within an operator-specified dynamic load tolerance.   The current test setup yields differing experimental results from those forwarded in [19]. The influences of the soft shaker mount and the more structurally rigid shaft support are hereby evident.

Future testing might include further modifications to the DAQ program that allows another input signal to act as the acquisition trigger, perhaps bearing displacement. The high temperature cartridge heater addition performs well and is only limited by the operating temperature limits of the top foil coating and the accelerometer

and load cell instrumentation in contact with the bearing housing. Finally, the use of a uniform outer diameter hollow test shaft and a longer cartridge heater is recommended to reduce the effects of the axial thermal gradient within the test shaft.

REFERENCES

[1] Valco, M., and Dellacorte, C., 2002, "Emerging Oil-Free Turbomachinery Technology for Military Propulsion and Power Applications," *Proc. 23rd Army Science Conference*, Fort Lauderdale, FL.

[2] Heshmat, H., and Ku, C., 1994, "Structural Damping of Self-Acting Compliant Foil Journal Bearings," ASME J. Tribol., **116**, pp. 76-82.

[3] Agrawal, G., 1997, "Foil Air/Gas Bearing Technology—an Overview," ASME Paper No. 97-GT-347.

[4] Fields, S., 2004, "Foil Air Bearing Technology Takes Flight," Tribol. Lubr. Technol., **60**(4), pp. 28-33.

[5] Peng, J., and Carpino, M., 1993, "Calculation of Stiffness and Damping Coefficients for Elastically Supported Gas Foil Bearings," ASME J. Tribol., **115**, pp. 20-27.

[6] Heshmat, H., Walowit, J., and Pinkus, O., 1983, "Analysis of Gas-Lubricated Foil Journal Bearings," ASME J. Lubr. Technol., **105**, pp. 647-655.

[7] Ku, C., and Heshmat, H., 1992, "Compliant Foil Bearing Structural Stiffness Analysis: Part I--Theoretical Model Including Strip and Variable Bump Foil Geometry," ASME J. Tribol., **113**(2), pp. 364-369.

[8] Ku, C., and Heshmat, H., 1992, "Compliant Foil Bearing Structural Stiffness Analysis: Part II--Experimental Investigation," ASME J. Tribol., **115**(2), pp. 364-369.

[9] Peng, J., and Carpino, M., 1994, "Coulomb Friction Damping Effects in Elastically Supported Gas Foil Bearings," STLE Tribol. Trans., **37**, pp. 91-98.

[10] Ku, C., and Heshmat, H., 1994, "Structural Stiffness and Coulomb Damping in Compliant Foil Journal Bearings: Theoretical Considerations," STLE Tribol. Trans., **37**(3), 525-533.

[11] Swanson, E., and Heshmat, H., 1999, "The Integration of Structural and Fluid Film Dynamic Elements in Foil Bearings Part II: A New Approach to the Problem," ASME Paper No. DETC99/VIB-8270.

[12] Ku, C., and Heshmat, H., 1994, "Structural Stiffness and Coulomb Damping in Compliant Foil Journal Bearings: Parametric Studies," STLE Tribol. Trans., **37**, 455-462.

[13] Ku, C., and Heshmat, H., 1994, "Effects of Static Load on Dynamic Structural Properties in a Flexible Supported Foil Journal Bearing," ASME J. Vib. Acoust., **116**(3), pp. 257-262.

[14] Ku, C., and Heshmat, H., 1994, "Effects of Frequency on Structural Stiffness and Damping in a Self-Acting Compliant Foil Journal Bearing," ASME Paper No. 94-GT-100.

[15] Dellacorte, C., and Valco, M., 2000, "Load Capacity Estimation of Foil Air Journal Bearings for Oil-Free Turbomachinery Applications," STLE Tribol. Trans., **43**(4), pp. 795-801.

[16] Radil, K., Howard, and S., Dykas, B., 2002, "The Role of Radial Clearance on the Performance of Foil Air Bearings," STLE Tribol. Trans., **45**(4), pp. 485-490.

[17] Rubio, D., and San Andrés, L., 2006, "Bump-Type Foil Bearing Structural Stiffness: Experiments and Predictions," ASME J. Eng. Gas Turbines Power, **128**(3), pp. 653-660.

[18] Salehi, M., Heshmat, H., and Walton II, J., 2007, "Advancements in the Structural Stiffness and Damping of a Large Compliant Foil Journal Bearing: an Experimental Study," ASME J. Eng. Gas Turbines Power, **129**, pp. 154-161.

[19] Rubio, D., and San Andrés, L., 2005, "Structural Stiffness, Dry-Friction and Equivalent Viscous Damping in a Bump-Type Foil Bearing," *Proc. ASME Turbo Expo*, **4**, Reno-Tahoe, NV, pp.737-746.

[20] Dellacorte, C., 1998, "A New Foil Air Bearing Test Rig for Use to 700°C and 70,000 rpm," STLE Tribol. Trans., **41**, pp. 335-340.

[21] Dellacorte, C., Lukaszewicz, V., Valco, M., Radil, K., and Heshmat, H., 2000, "Performance and Durability of High Temperature Foil Air Bearings for Oil-Free Turbomachinery," STLE Tribol. Trans., **43**(4), 744-780.

[22] Dellacorte, Christopher. Personal Communication. 10 July 2006.

[23] Howard, S., Dellacorte, C., Valco, M., Prahl, J., and Heshmat, H., 2001 "Dynamic Stiffness and Damping Characteristics of a High-Temperature Air Foil Journal Bearing," STLE Tribol. Trans., **44**(4), pp. 657-663.

[24] "Coefficient of Thermal Expansion," MatWeb - Online Material Data Sheet, (updated 01 February 2007), (accessed 31 July 2006), available from World Wide Web: <http://www.matweb.com>

[25] "Thermal Expansion Calculator," Expansion Joint Systems, Inc., (accessed 22 July 2006), available from World Wide Web: <http://206.71.175.206/ejs/thermal_expansion_data.htm>

[26] Incropera, F., and Dewitt, D., 2002, *Fundamentals of Heat and Mass Transfer*, Fifth Edition, Wiley, New York, pp. 243-247, 554-556, 917.

[27] "Thermal Conductivity," MatWeb - Online Material Data Sheet, (updated 01 February 2007), (accessed 04 February 2006), available from World Wide Web: <http://www.matweb.com>

[28] Iordanoff, I., 1999, "Analysis of an Aerodynamic Compliant Foil Thrust Bearing: Method for a Rapid Design," ASME J. Tribol., **121**(4), pp. 816-822.

[29] "Young Modulus of Elasticity for Metals," The Engineering ToolBox, 2005, (accessed 31 July 2006), available from World Wide Web: <http://www.engineeringtoolbox.com/young-modulus-d_773.html >

[30] Ginsberg, J., 2001, *Mechanical and Structural Vibrations-Theory and Applications*, Wiley, New York, pp. 137-139.

APPENDIX A

EDDY CURRENT SENSOR CALIBRATION FOR TEST COMPONENTS AS TARGETS

Test Shaft (AISI 4140 Steel)

Figure A1 shows the calibration plot for the eddy current sensor (ECS) with the test shaft (AISI 4140 Steel) as the target material. The calibration displacement was measured using 1) a digital readout on a machine shop lathe and 2) a contact dial gauge (both plots are presented in the figure). The equations in the figure are the equations of the linear fit of the voltage versus displacement data, complete with the slope of the line (gain) plus the ordinate intercept. The R^2 term reports the goodness of fit between the line fit and the measured data.
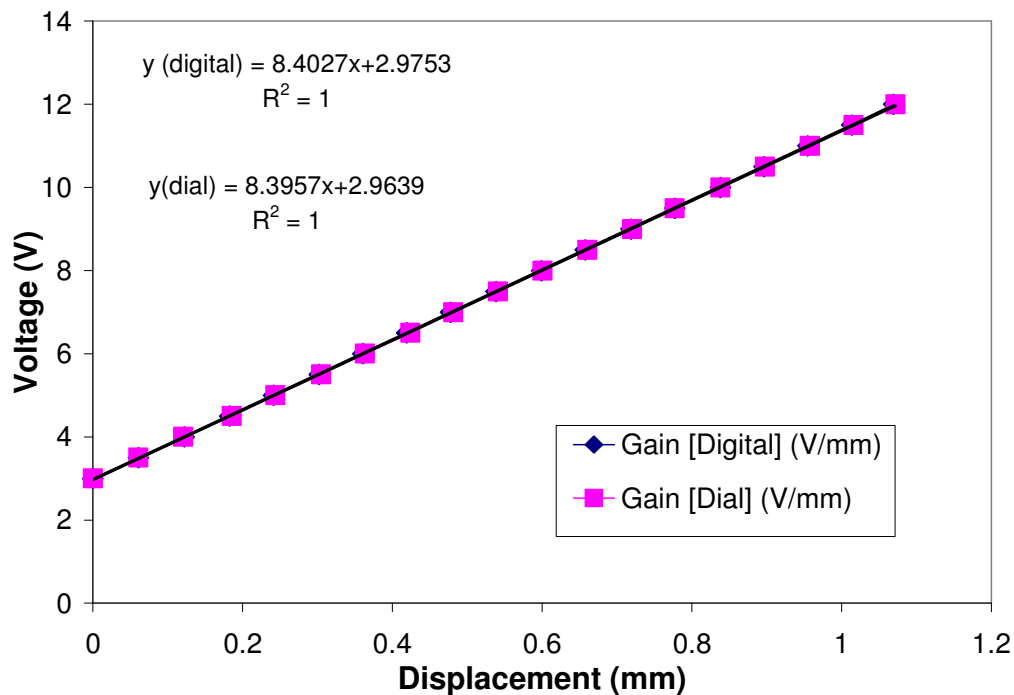
Figure A1 Eddy current sensor gain for the AISI 4140 Steel test shaft as the target at room temperature (21°C).

The ECS gains yielded by the two instruments are nearly identical (0.08% error). Thus, the gain provided by the measurements of the digital display on the lathe, 8.40 V/mm (213.36 mV/mil), is designated for experimental purposes, namely determination of the CTE of steel test shaft. The uncertainty of the gain is given with respect to the test shaft is given in Appendix B as $U_{G,S} = 0.016$ V/mm (0.41 mV/mil).

FB Housing (AISI 304 Stainless Steel)

Figure A2 shows the calibration plot for the ECS with the test FB housing (a non-magnetic AISI 304 Stainless Steel) as the target material for five increasing temperatures (from 22°C up to 121°C). The equations in the figure specify the linear fit, including slope and ordinate intercept, of each temperature data set. The slope of each line fit is the gain (V/mm) of the ECS for the respective bearing housing test temperature.   The R^2 term reports the goodness of fit between the line fit and the measured data. The five line equations correspond to the linear fit of the five data sets that appear nearly coincident, which indicates minimal change in ECS gain with target temperature.
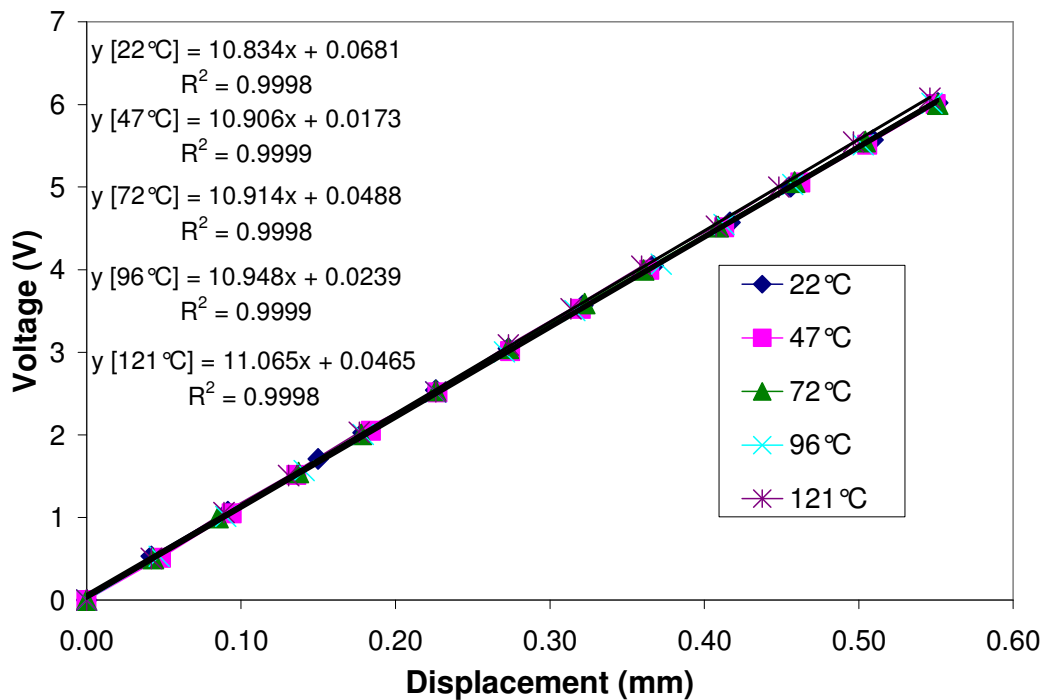
Figure A2 Eddy current sensor gain for the AISI 304 Stainless Steel FB housing as the target at increasing surface temperature (up to 121 °C).

Table A1 presents the average and standard deviation of the ECS gains at five target temperatures. This average, 10.93 V/mm (277.71 mV/mil), is the value of the gain provided to the computer code designated to determine the FB force coefficients, in addition to the calculation of the measured CTE of the bearing material. The uncertainty of the gain with respect to the bearing housing is given in Appendix B as $U_{G,B}$ = 0.036 V/mm (0.91 mV/mil). The standard deviation (or drift) with respect to the change in temperature of the target material proves to be negligible.

It is important to point out that the gains are different for the respective target materials. Table A2 gives the ECS gains and the associated uncertainties in SI units for both target materials.

Table A1 Summary of eddy current sensor calibration and corresponding average and standard deviation (FB Housing-AISI 304 Stainless Steel as the target)

Bearing Housing Temperature	Gain-SI Units (V/mm)	Gain-English Units (mV/mil)	Goodness of Linear Fit, R^2
22°C	10.834	275.18	0.9998
47°C	10.906	277.01	0.9999
72°C	10.914	277.22	0.9998
96°C	10.948	278.08	0.9999
121°C	11.065	281.05	0.9998
Average	10.93	277.71	
Standard Deviation	0.08	2.15	
Percent	0.77%	0.77%	

Table A2 The measured eddy current sensor gains and uncertainties for the AISI 4140 steel test shaft and AISI 304 stainless steel bearing housing

Target Material	Gain (V/mm)	Uncertainty (V/mm)
Test Shaft (AISI 4140 Steel)	8.40	0.016
Bearing Housing (AISI 304 Stainless Steel)	10.93	0.036

APPENDIX B

UNCERTAINTY ANALYSES

Uncertainty in Eddy Current Sensor Gains for the AISI 4140 Steel Test Shaft and the AISI 304 Stainless Steel Bearing Housing

The equation for the eddy current sensor (ECS) gain is given as:

$$Gain = G = \frac{\Delta V}{\Delta X} \tag{B.1}$$

where ΔV is the change in ECS voltage for the change in displacement, ΔX, of the ECS probe with respect to the either the test shaft (S) or bearing housing (B) target material.

The uncertainty associated with ECS gain is calculated as:

$$U_G = \sqrt{\left(\frac{\partial G}{\partial V_1} * u_{V_1}\right)^2 + \left(\frac{\partial G}{\partial V_2} * u_{V_2}\right)^2 + \left(\frac{\partial G}{\partial X_1} * u_{X_1}\right)^2 + \left(\frac{\partial G}{\partial X_2} * u_{X_2}\right)^2} \tag{B.2}$$

where $u_{\Delta VS} = 0.005$ V and $u_{\Delta VB} = 0.0005$ V are the uncertainties of the respective voltage readings and $u_{\Delta X} = 0.00127$ mm is the uncertainty of the digital displacement reading.

The resulting uncertainties for the ECS gains for the test shaft and the bearing housing, respectively, are as follows:

$U_{G,S} = 0.016$ V/mm (0.41 mV/mil)

$U_{G,B} = 0.036$ V/mm (0.91 mV/mil)

Uncertainty in Coefficient of Thermal Expansion Calculations for AISI 4140 Steel Test Shaft and the AISI 304 Stainless Steel Bearing Housing

The following analysis is carried out for both the test shaft (subscript S) and the bearing housing; however, the equations and explanation corresponding to the bearing housing data and are omitted here for brevity. The final uncertainties for both material coefficient of thermal expansion (CTEs) are noted.

The equation for the CTE of the test shaft is given as

$$\alpha_S = \frac{\delta R_S}{R_{S,i}\Delta T_S} \tag{B.3}$$

where δR_S is the change in the outer radius of the shaft, $R_{S,I}$ is the initial outer radius of the shaft, and ΔT_S is the change in surface temperature of the shaft.

The uncertainty in the CTE calculation becomes

$$U_{\alpha_S} = \sqrt{\left(\frac{\partial \alpha_S}{\partial \delta R_S} * U_{\delta R_S}\right)^2 + \left(\frac{\partial \alpha_S}{\partial R_{S,i}} * u_{R_{S,i}}\right)^2 + \left(\frac{\partial \alpha_S}{\partial \Delta T_S} * u_{\Delta T_S}\right)^2} \tag{B.4}$$

where $U_{\delta RS}$ is the uncertainty associated with the experimental measurement of δR_S, $u_{RS,I}$ = 3.175 μm is the uncertainty of the measured initial outer radius of the shaft, and $u_{\Delta TS}$ = 0.5°C is the uncertainty of the shaft temperature change measurement.

Experiments were performed using the change in ECS voltage to detect the change in test shaft radius over a range of temperature. The equation for this change is

$$\delta R_S = \frac{\Delta V}{G_S} = \frac{V_2 - V_1}{G_S} \tag{B.5}$$

where G_S = 8.40 V/mm is the calibrated ECS gain when the shaft is the target.

The uncertainty associated with the measurement of δR_S is given as

$$U_{\delta R_S} = \sqrt{\left(\frac{\partial \delta R_S}{\partial V_1} * u_{V_1}\right)^2 + \left(\frac{\partial \delta R_S}{\partial V_2} * u_{V_2}\right)^2 + \left(\frac{\partial \delta R_S}{\partial G_S} * U_{G_S}\right)^2} \tag{B.6}$$

where $u_{\Delta V}$ = 0.00005 V is the uncertainty of the voltmeter used during the experiment, and $U_{G,S}$ = 0.016 V/mm is the uncertainty of the ECS gain for the test shaft as the target. The resulting uncertainties for the experimental measurements of the change of the shaft outer radius, and bearing housing outer radius, respectively, are as follows:

$U_{\delta RS}$ = 0.044 μm (1.7 * 10⁻³ mil)

$U_{\delta RB}$ = 0.18 μm (7.1 * 10⁻³ mil).

Now, returning to Equation (B.4), the uncertainties for the CTE calculation from experimental data for the shaft and bearing housing, respectively, are as follows:

$U_{\alpha,S}$ = 0.071 μm/(m*°C) ~ 0.07 μm/(m*°C)

$U_{\alpha,B}$ = 0.026 μm/(m*°C) ~ 0.03 μm/(m*°C).

Uncertainty in the Estimated Radial Clearance Calculations

The equation for the estimation of bearing radial clearance based on the geometry of the test components is $C_g = R_B - Q - R_S$, where R_B is the inner radius of the bearing housing, Q is the foil layer height, and R_S is the measured outer radius of the shaft. The inner radius of the bearing housing is $R_B = R - W_B$, where R is the outer radius of the bearing housing and W_B is the measured bearing housing wall thickness.

The uncertainty equation is

$$U_{C_g} = \sqrt{\left(\frac{\partial C_g}{\partial R_B} * u_{R_B}\right)^2 + \left(\frac{\partial C_g}{\partial Q} * u_Q\right)^2 + \left(\frac{\partial C_g}{\partial R_S} * u_{R_S}\right)^2} \tag{B.7}$$

Two uncertainties exist from measurements in the clearance estimation since the dimensions comprising Q are given. Note that $u_{R,B} = 6.35$ μm is the uncertainty of the bearing housing wall thickness measurement, and $u_{R,S} = 3.175$ μm is the uncertainty of the outer radius of the shaft measurement. The resulting uncertainty in the estimation of bearing radial clearance based on the geometry of the test components is $U_{Cg} = 7.1$ μm (0.28 mil).

APPENDIX C
STATIC LOAD VERSUS FB DEFLECTION EXPERIMENTAL
DATA FOR +/- 8.9 N LOAD RANGE

Figure C1 through Figure C3 show the measured static load versus FB deflection data for the load interval -8.9 N $\leq F \leq$ 8.9 N, which is the region of low repeatability. Figure C1 shows the experimental load versus FB deflection data for the 45°-225° and the 90°-270° bearing orientations on the 38.075 mm shaft at room temperature.
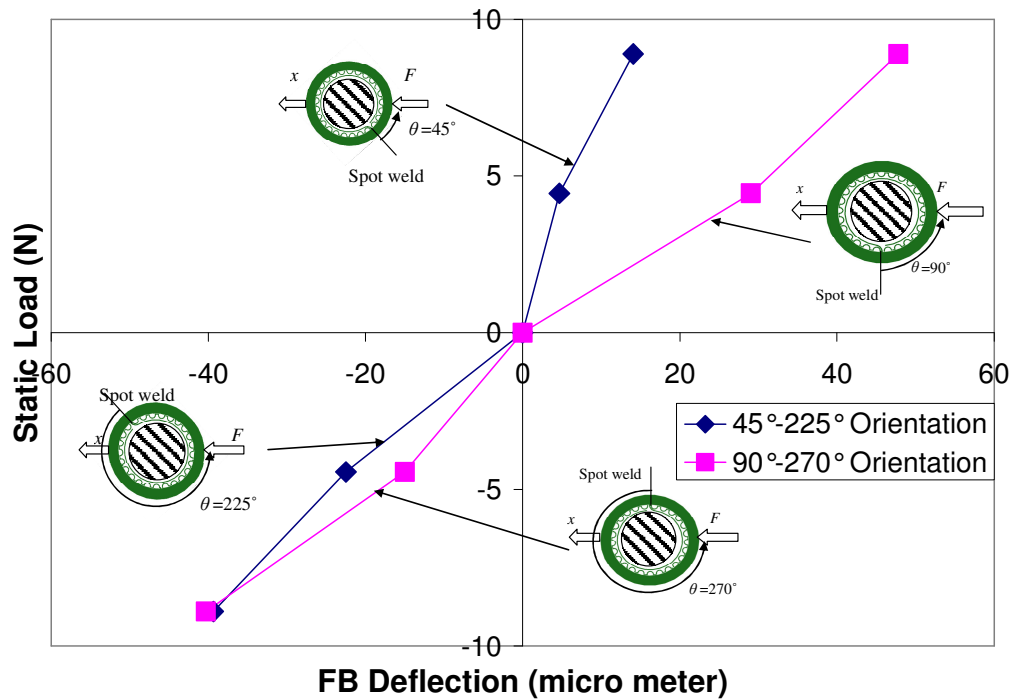
Figure C1 FB deflection due to +/-8.9 N (2 lb) for two bearing orientations (45°-225° and 90°-270°) for the 38.075 mm shaft at room temperature (C_{nom} = 48.3 μm).

Figure C2 and Figure C3 show the load versus FB deflection data with the 38.125 mm shaft at increasing temperature for the 45°-225° and the 90°-270° bearing orientations, respectively. Along the 45° and 90° directions, on its respective plot, the 4.4 N data point taken with the test shaft at 188°C fails to follow a trend.
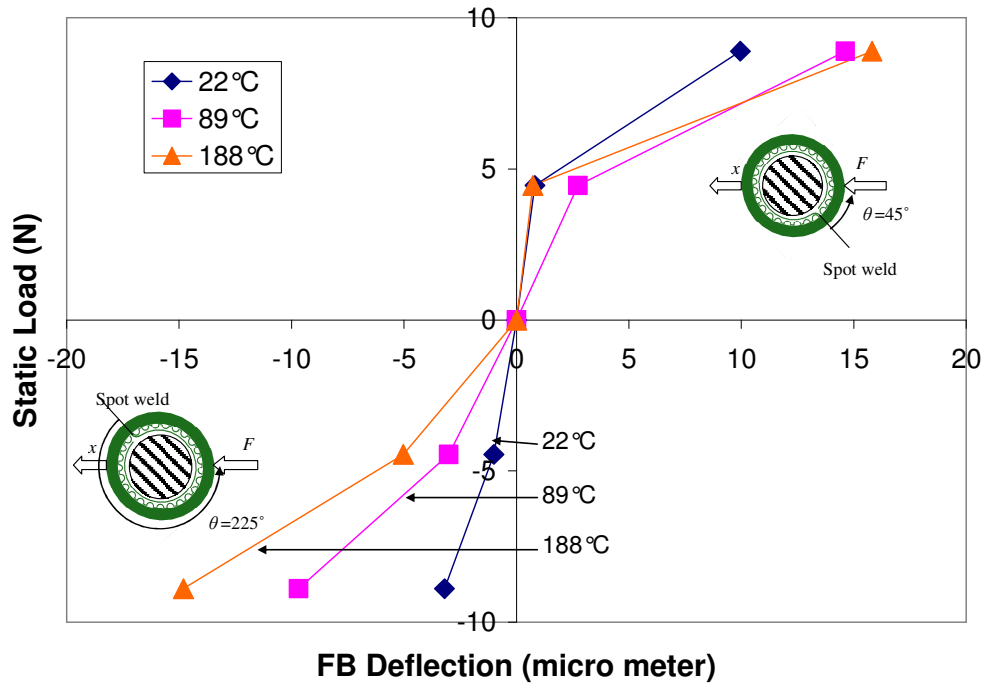
Figure C2 FB deflection for +/-8.9 N for the 45°-225° bearing orientation at increasing shaft temperatures (38.125 mm shaft, C_{nom} = 22.9 μm).
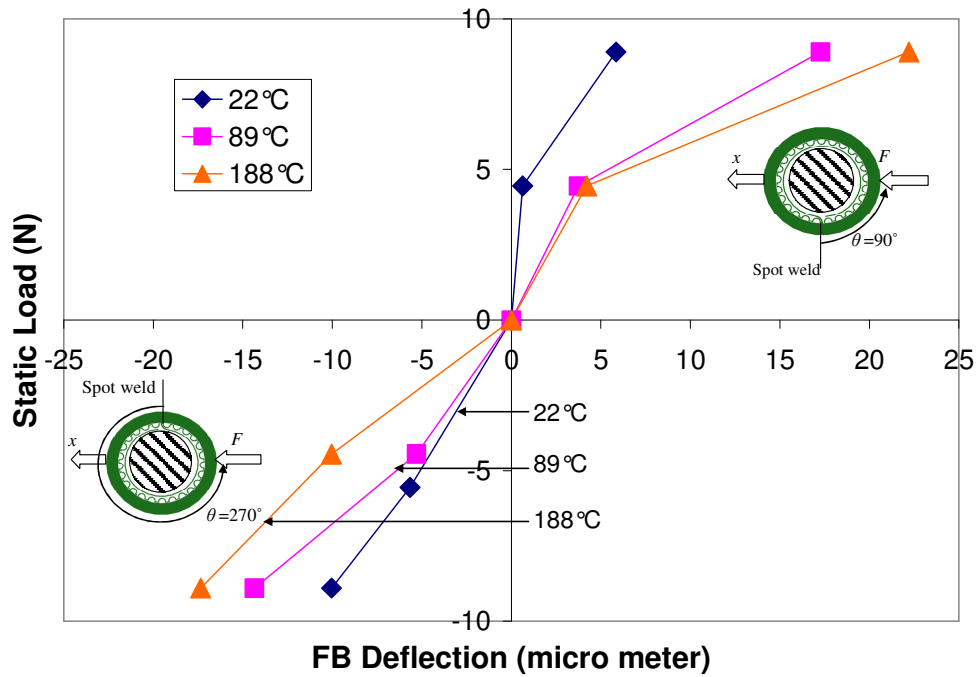
Figure C3 FB deflection for +/-8.9 N for the 90°-270° bearing orientation at increasing shaft temperature (38.125 mm shaft, C_{nom} = 22.9 μm).

APPENDIX D

COEFFICIENTS FOR STATIC STRUCTURAL STIFFNESS CURVE FIT

Table D1 gives a summary of the curve fit coefficients for Equations (14) and (15), hereby reproduced for convenience. For $x \leq x_a$,

$$F(x) = -8.9N + A_{n1}(x - x_a) + A_{n2}(x - x_a)^3 \qquad (D.1)$$

where A_n are the coefficients for the pull (negative) displacement cases. For $x \geq x_b$,

$$F(x) = 8.9N + A_{p1}(x - x_b) + A_{p2}(x - x_b)^3 \qquad (D.2)$$

where A_p are the coefficients for the push (positive) displacement cases. Also, the goodness of fit for the curve fit to the experimental data, R^2, is also included.

Table D1 Summary of derived force curve fit coefficients for corresponding FB deflection intervals and goodness of fit for all test cases

| D_S (mm) | Bearing Orientation | T_S (°C) | $x \leq x_a$ | | $x \geq x_b$ | | Fit (R^2) |
			A_{n1} (N/m)	A_{n2} (N/m³)	A_{p1} (N/m)	A_{p2} (N/m³)	
38.075	45°-225°	22	0.879	$4.117*10^{-4}$	1.436	$4.613*10^{-4}$	0.998
	90°-270°	22	0.011	$3.373*10^{-4}$	0.667	$3.499*10^{-4}$	0.998
38.125	45°-225°	22	1.386	$8.493*10^{-4}$	0.893	$5.457*10^{-4}$	0.999
		89	1.200	$9.906*10^{-4}$	0.816	$6.297*10^{-4}$	0.999
		188	1.151	$1.021*10^{-3}$	0.683	$5.939*10^{-4}$	0.999
	90°-270°	22	1.609	$1.073*10^{-3}$	0.445	$1.573*10^{-4}$	0.998
		89	1.413	$4.473*10^{-3}$	0.228	$1.970*10^{-4}$	0.999
		188	1.669	$1.414*10^{-3}$	0.128	$1.801*10^{-4}$	0.998

APPENDIX E

VARIATION OF MATERIAL YOUNG MODULUS WITH TEMPERATURE

Table E1 Variation of bearing and shaft material Young Modulus with temperature [29]

Temperature (°C)	Test Shaft Carbon Steel, C=>0.3%	Bearing Housing Austenitic Steel, (TP304)	Top and Bump Foils Cr-Mo Steels, Cr 5% - 9%
21	202	195	213
93	197	190	208
149	194	186	205
204	190	183	200

Table E2 Linear interpolation of bump foil material Modulus of Elasticity from data in reference [29]

Cr-Mo Steels, Cr 5% - 9%	
Temperature (deg C)	Young Modulus (GPa)
21	213
55	210.6
89	208.3
122	206.5
155	204.5
188	201.5
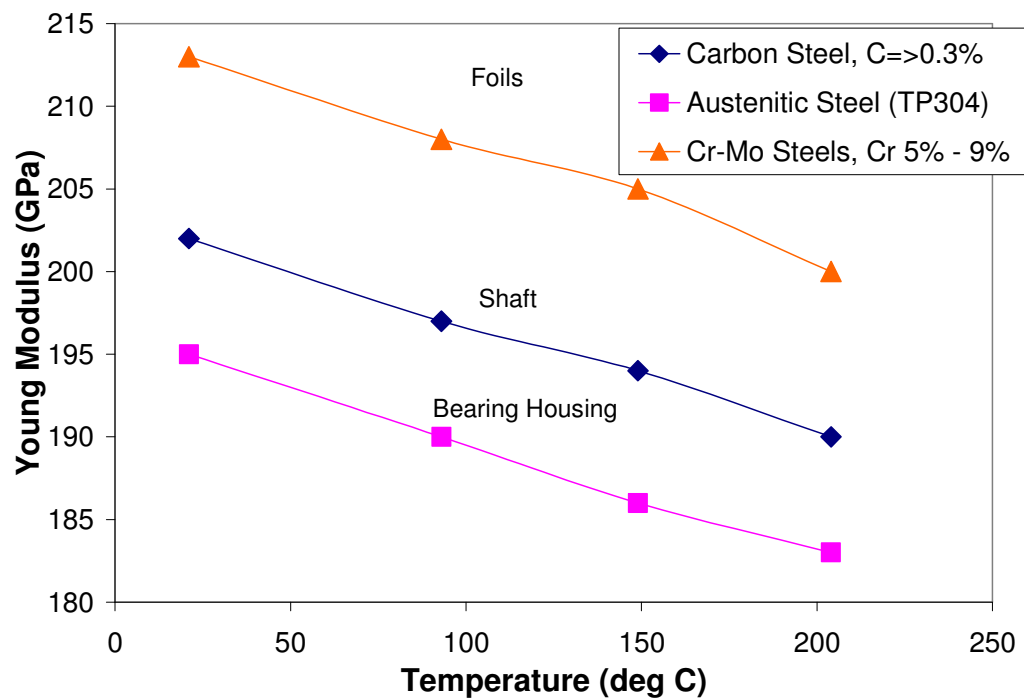
Figure E1 Variation of bearing housing, foil and shaft material Young Modulus with temperature.

APPENDIX F

EXPERIMENTAL DYNAMIC FB SRUCTURAL STIFFNESS DATA COMPILED FOR CALCULATION OF AVERAGES AND ERROR FOR THE 45°-225° BEARING ORIENTATION ON THE 38.125 mm SHAFT (C_{nom} = 22.9 μm)

Table F1 FB dynamic stiffness average and standard deviation (F_O = 13.3 N, T_S = 22℃)

	$K = \text{Re}[(F_O - M\ddot{x})/x]$ (MN/m)			Average K (MN/m)	Standard Deviation K (MN/m)	Percent Error
Freq (Hz)	Trial 1	Trial 2	Trial 3			
40	0.92	0.91	0.91	0.91	4.72E-03	0.52
60	0.96	0.96	0.95	0.95	8.96E-04	0.09
80	0.93	0.94	0.94	0.94	5.75E-03	0.61
100	0.93	0.95	0.94	0.94	5.67E-03	0.60
120	1.07	1.07	1.07	1.07	2.65E-03	0.25
140	1.06	1.06	1.07	1.06	4.16E-03	0.39
160	1.18	1.19	1.19	1.19	3.46E-03	0.29
180	1.23	1.22	1.23	1.23	3.61E-03	0.29
200	1.25	1.25	1.27	1.26	7.23E-03	0.58

Table F2 FB dynamic stiffness average and standard deviation (F_O = 22.2 N, T_S = 22℃)

	$K = \text{Re}[(F_O - M\ddot{x})/x]$ (MN/m)			Average K (MN/m)	Standard Deviation K (MN/m)	Percent Error
Freq (Hz)	Trial 1	Trial 2	Trial 3			
40	0.76	0.76	0.75	0.76	3.17E-03	0.42
60	0.76	0.76	0.75	0.76	5.01E-03	0.66
80	0.75	0.74	0.74	0.74	5.48E-03	0.74
100	0.78	0.76	0.75	0.76	1.28E-02	1.68
120	0.91	0.85	0.85	0.87	3.23E-02	3.71
140	0.91	0.89	0.88	0.89	1.45E-02	1.63
160	0.97	0.96	0.94	0.96	1.51E-02	1.58
180	1.03	1.04	1.03	1.03	3.51E-03	0.34
200	1.07	1.07	1.07	1.07	3.06E-03	0.29

Table F3 FB dynamic stiffness average and standard deviation (F_O = 31.1 N, T_S = 22 °C)

Freq (Hz)	$K = \mathrm{Re}[(F_O - M\ddot{x})/x]$ (MN/m)			Average K (MN/m)	Standard Deviation K (MN/m)	Percent Error
	Trial 1	Trial 2	Trial 3			
40	0.88	0.88	0.88	0.88	6.11E-04	0.07
60	0.87	0.87	0.86	0.87	6.09E-03	0.70
80	0.86	0.85	0.85	0.85	4.81E-03	0.56
100	0.86	0.86	0.86	0.86	4.60E-03	0.53
120	0.95	0.94	0.94	0.95	5.71E-03	0.60
140	0.95	0.95	0.95	0.95	2.35E-03	0.25
160	1.06	1.06	1.05	1.05	4.73E-03	0.45
180	1.12	1.11	1.11	1.11	8.00E-03	0.72
200	1.18	1.17	1.18	1.18	5.13E-03	0.44

Table F4 FB dynamic stiffness average and standard deviation (F_O = 13.3 N, T_S = 77 °C)

Freq (Hz)	$K = \mathrm{Re}[(F_O - M\ddot{x})/x]$ (MN/m)			Average K (MN/m)	Standard Deviation K (MN/m)	Percent Error
	Trial 1	Trial 2	Trial 3			
40	0.55	0.53	0.53	0.54	1.37E-02	2.53
60	0.55	0.53	0.52	0.53	1.54E-02	2.92
80	0.53	0.52	0.52	0.52	1.11E-02	2.12
100	0.56	0.56	0.55	0.56	5.54E-03	0.99
120	0.66	0.64	0.64	0.64	8.94E-03	1.39
140	0.71	0.69	0.69	0.70	7.99E-03	1.15
160	0.76	0.75	0.74	0.75	8.27E-03	1.10
180	0.83	0.81	0.82	0.82	7.89E-03	0.96
200	0.88	0.88	0.89	0.88	2.05E-03	0.23

Table F5 FB dynamic stiffness average and standard deviation (F_O = 22.2 N, T_S = 77 ℃)

Freq (Hz)	$K = \mathrm{Re}[(F_O - M\ddot{x})/x]$ (MN/m)			Average K (MN/m)	Standard Deviation K (MN/m)	Percent Error
	Trial 1	Trial 2	Trial 3			
40	0.66	0.65	0.65	0.65	5.60E-03	0.86
60	0.65	0.64	0.64	0.64	5.19E-03	0.81
80	0.64	0.63	0.63	0.64	6.37E-03	1.00
100	0.66	0.65	0.66	0.66	9.87E-04	0.15
120	0.75	0.74	0.74	0.74	7.59E-03	1.03
140	0.79	0.78	0.78	0.78	6.24E-03	0.80
160	0.85	0.85	0.85	0.85	3.61E-03	0.42
180	0.94	0.94	0.94	0.94	2.86E-03	0.30
200	1.01	1.00	1.01	1.01	5.00E-03	0.50

Table F6 FB dynamic stiffness average and standard deviation (F_O = 31.1 N, T_S = 77 ℃)

Freq (Hz)	$K = \mathrm{Re}[(F_O - M\ddot{x})/x]$ (MN/m)			Average K (MN/m)	Standard Deviation K (MN/m)	Percent Error
	Trial 1	Trial 2	Trial 3			
40	0.77	0.77	0.78	0.77	4.31E-03	0.56
60	0.76	0.76	0.76	0.76	1.22E-03	0.16
80	0.76	0.76	0.76	0.76	3.12E-03	0.41
100	0.78	0.78	0.78	0.78	2.32E-03	0.30
120	0.86	0.85	0.85	0.86	5.47E-03	0.64
140	0.87	0.87	0.88	0.87	5.20E-03	0.60
160	0.96	0.96	0.96	0.96	4.34E-03	0.45
180	1.07	1.07	1.05	1.06	8.72E-03	0.82
200	1.12	1.12	1.14	1.13	1.06E-02	0.94

Table F7 FB dynamic stiffness average and standard deviation (F_O = 13.3 N, T_S = 132 ℃)

	$K = \mathrm{Re}[(F_O - M\ddot{x})/x]$ (MN/m)			Average K (MN/m)	Standard Deviation K (MN/m)	Percent Error
Freq (Hz)	Trial 1	Trial 2	Trial 3			
40	0.44	0.43	0.43	0.43	7.97E-03	1.84
60	0.43	0.42	0.42	0.42	9.05E-03	2.14
80	0.44	0.43	0.43	0.43	9.26E-03	2.13
100	0.49	0.49	0.49	0.49	7.51E-04	0.15
120	0.56	0.55	0.54	0.55	5.30E-03	0.96
140	0.61	0.59	0.59	0.60	7.55E-03	1.26
160	0.66	0.66	0.66	0.66	1.36E-03	0.21
180	0.72	0.72	0.72	0.72	2.11E-03	0.29
200	0.79	0.80	0.79	0.79	2.44E-03	0.31

Table F8 FB dynamic stiffness average and standard deviation (F_O = 22.2 N, T_S = 132 ℃)

	$K = \mathrm{Re}[(F_O - M\ddot{x})/x]$ (MN/m)			Average K (MN/m)	Standard Deviation K (MN/m)	Percent Error
Freq (Hz)	Trial 1	Trial 2	Trial 3			
40	0.54	0.56	0.55	0.55	6.37E-03	1.16
60	0.54	0.54	0.54	0.54	1.61E-03	0.30
80	0.55	0.56	0.55	0.55	1.51E-03	0.27
100	0.59	0.59	0.59	0.59	1.18E-03	0.20
120	0.67	0.67	0.67	0.67	3.24E-03	0.49
140	0.70	0.70	0.69	0.70	5.52E-03	0.79
160	0.79	0.78	0.78	0.79	5.19E-03	0.66
180	0.86	0.87	0.87	0.87	7.85E-03	0.91
200	0.95	0.95	0.96	0.95	4.21E-03	0.44

Table F9 FB dynamic stiffness average and standard deviation (F_O = 31.1 N, T_S = 132 ℃)

	$K = \text{Re}[(F_O - M\ddot{x})/x]$ (MN/m)			Average	Standard Deviation	Percent
Freq (Hz)	Trial 1	Trial 2	Trial 3	K (MN/m)	K (MN/m)	Error
40	0.67	0.66	0.66	0.66	2.39E-03	0.36
60	0.65	0.65	0.65	0.65	1.27E-03	0.20
80	0.67	0.67	0.66	0.67	6.05E-03	0.91
100	0.70	0.70	0.70	0.70	2.69E-03	0.38
120	0.78	0.78	0.77	0.77	6.92E-03	0.89
140	0.79	0.78	0.79	0.79	5.18E-03	0.66
160	0.89	0.90	0.89	0.89	6.54E-03	0.73
180	0.96	0.96	0.96	0.96	1.14E-03	0.12
200	1.06	1.07	1.06	1.06	5.86E-03	0.55

Table F10 FB dynamic stiffness average and standard deviation (F_O = 13.3 N, T_S = 188 ℃)

	$K = \text{Re}[(F_O - M\ddot{x})/x]$ (MN/m)			Average	Standard Deviation	Percent
Freq (Hz)	Trial 1	Trial 2	Trial 3	K (MN/m)	K (MN/m)	Error
40	0.39	0.37	0.38	0.38	6.54E-03	1.72
60	0.39	0.37	0.38	0.38	7.46E-03	1.97
80	0.39	0.39	0.38	0.39	3.71E-03	0.96
100	0.45	0.45	0.45	0.45	8.50E-04	0.19
120	0.50	0.50	0.49	0.50	4.11E-03	0.83
140	0.54	0.54	0.53	0.53	5.09E-03	0.95
160	0.61	0.61	0.61	0.61	3.57E-03	0.58
180	0.69	0.69	0.68	0.69	5.02E-03	0.73
200	0.77	0.77	0.76	0.77	6.90E-03	0.90

Table F11 FB dynamic stiffness average and standard deviation (F_O = 22.2 N, T_S = 188 ℃)

Freq (Hz)	$K = \mathrm{Re}[(F_O - M\ddot{x})/x]$ (MN/m)			Average K (MN/m)	Standard Deviation K (MN/m)	Percent Error
	Trial 1	Trial 2	Trial 3			
40	0.49	0.49	0.49	0.49	3.67E-03	0.75
60	0.48	0.48	0.47	0.48	2.21E-03	0.46
80	0.50	0.50	0.50	0.50	2.50E-03	0.50
100	0.54	0.54	0.54	0.54	1.73E-03	0.32
120	0.61	0.60	0.59	0.60	8.00E-03	1.33
140	0.62	0.62	0.62	0.62	3.32E-03	0.54
160	0.73	0.72	0.71	0.72	1.08E-02	1.49
180	0.80	0.80	0.79	0.80	3.73E-03	0.47
200	0.90	0.89	0.89	0.89	4.20E-03	0.47

Table F12 FB dynamic stiffness average and standard deviation (F_O = 31.1 N, T_S = 188 ℃)

Freq (Hz)	$K = \mathrm{Re}[(F_O - M\ddot{x})/x]$ (MN/m)			Average K (MN/m)	Standard Deviation K (MN/m)	Percent Error
	Trial 1	Trial 2	Trial 3			
40	0.59	0.60	0.60	0.59	3.81E-03	0.64
60	0.59	0.58	0.58	0.58	3.97E-03	0.68
80	0.62	0.62	0.62	0.62	2.14E-03	0.34
100	0.65	0.65	0.65	0.65	4.75E-03	0.73
120	0.71	0.70	0.69	0.70	6.78E-03	0.97
140	0.72	0.72	0.71	0.72	3.41E-03	0.48
160	0.82	0.82	0.81	0.82	5.41E-03	0.66
180	0.91	0.91	0.91	0.91	1.27E-03	0.14
200	1.00	1.00	0.99	1.00	5.75E-03	0.58

APPENDIX G

DYNAMIC TEST BEHAVIOR OF TEST FOIL BEARING FOR EXCITATION AT FREQUENCIES UP TO 420 HZ

This appendix details shaker testing performed prior to the testing detailed in the thesis. The natural frequency, identified by a rap test, of the shaft and indexing fixture assembly is approximately 380 Hz. Accordingly, shaker tests were conducted to determine the FB behavior through the known shaft resonance. This report provides data of FB testing behavior up to 420 Hz. Table G1 provides the test parameters for the experiments.

Table G1 Shaker test (up to 420 Hz) parameters

Dynamic Load, N [lb]	8, 12, 16, 20 [1.8, 2.7, 3.6, 4.5]
Load Tolerance, N [lb]	+/- 0.445 [0.1]
Frequency Range, Hz	40 - 420
Shaft Temperature, °C	21, 77, 132, 188
Bearing Orientation	45°

Figure G1 shows steady load behavior for the entire test frequency range for the first three amplitudes of dynamic load. However, for the fourth load case (20 N) the dynamic load spikes up to 25 N at 370 Hz (near the test shaft natural frequency). Note that the test operator manually saved this data point because its load magnitude is outside of the acceptable tolerance of the DAQ system. To clarify, the DAQ system automatically adjusts the voltage supplied to the electromagnetic shaker such that the load cell signal attains the target amplitude of dynamic load of 20 N (± 0.4 N). In this case, however, as the load amplitude approached its target, the forced excitation was sufficient to excite the shaft natural frequency. When this resonance occurs, the load cell signal spikes to values above the target value, and the DAQ system automatically resets the shaker voltage so the load cell signal returns below the target value. At this

point, the shaft resonance is not being excited. Then, the DAQ system begins to automatically adjust the shaker voltage, as before, to approach the target load signal voltage. As the shaker amplitude increases, the operator arbitrarily initiates data saving process before the onset of shaft resonance and system instability. Sometimes the onset occurs so rapidly that, once the process to save the data commences, the amplitude of dynamic load has already become uncontrolled. In this case, the saved load cell signal spiked up to 25 N, while the target dynamic load amplitude was only 20 N.
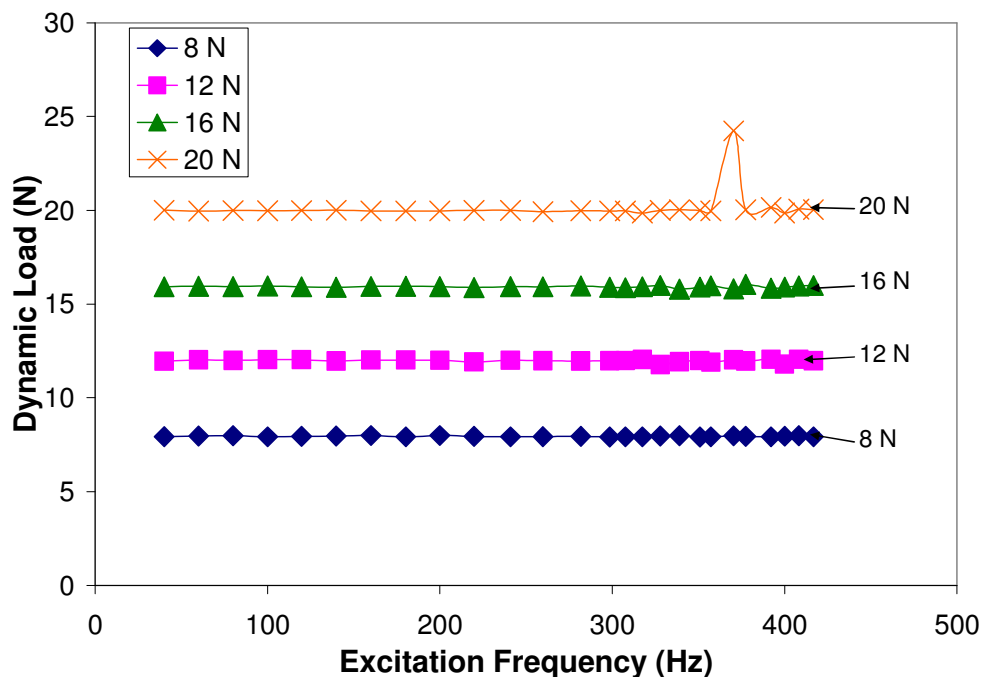
Figure G1 Amplitude of dynamic load versus excitation frequency (up to 420 Hz) with T_S = 25°C (ambient).

Figure G2 shows the acceleration magnitude of the FB housing as a function of excitation frequency for the four dynamic load cases. Note the distinct peaks of response. For the 8 N and 12 N load cases the peaks occur at 260 Hz and 377 Hz. For the 16 N and 20 N load cases the peaks occur at 240 Hz and 370 Hz. This is a clear indication that the natural frequency of the FB mass is approximately 260 Hz.

Figure G2 Amplitude of FB acceleration versus excitation frequency (up to 420 Hz) showing visible peak responses with T$_S$ = 25°C (ambient).

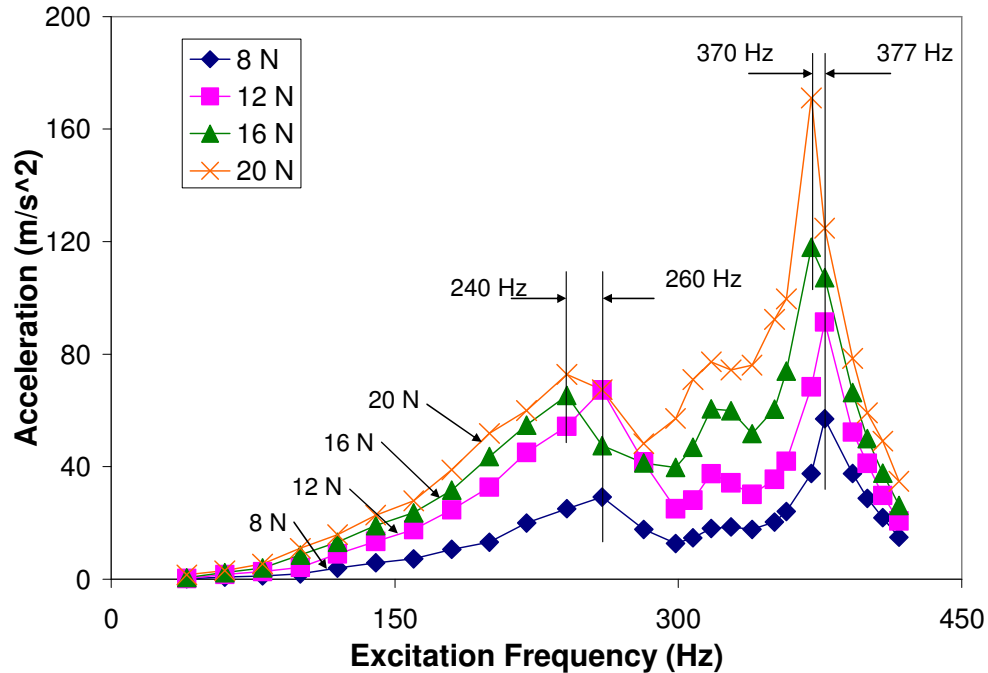Note that the two higher loads have resonance peaks at slightly lower frequencies than the two lower loads. Obviously, for a given mass, if the natural frequency decreases, then a decrease in stiffness occurs. Therefore, Figure G2 indicates that the FB dynamic stiffness decreases with amplitude of dynamic load between the 12 N and 16 N load cases. Table G2 provides the estimated FB stiffness at the resonance frequency associated with the FB mass ($M = 0.295$ kg) given by $K = \omega^2 M$.

Table G2 Stiffness estimation based on resonance peak frequencies and given FB mass (M = 0.295 kg)

Resonant Frequency	240 Hz	260 Hz
Dynamic Load (N)	16 and 20	8 and 12
Estimated K (MN/m)	0.671	0.787

Figure G3 shows the equivalent viscous damping of the FB versus excitation frequency for the test data shown in Figure G1. In [19] the authors find that at the system resonance that the system experiences null damping, which may have been a result of the former test setup. However, equivalent viscous damping is evident throughout the tested frequency range using the revamped test setup. Table G3 summarizes the C_{eq} values evidenced at the resonant frequency for its respective load case. Damping seems to increase slightly before decreasing again between the two resonant frequencies.
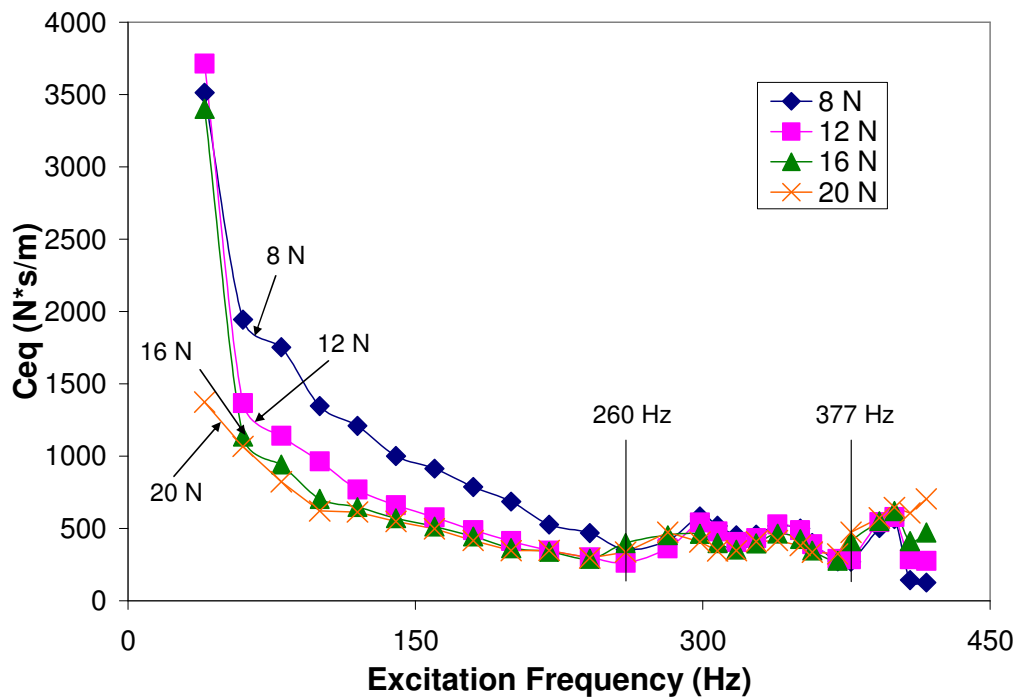
Figure G3 Equivalent viscous damping versus excitation frequency (up to 420 Hz) showing damping values at resonance with T_S = 25 °C (ambient).

Table G3 Equivalent viscous damping evidenced at system resonance (at T_S = 25 °C)

	C_{eq} (Ns/m) at Resonant Frequency			
Dynamic Load	240 Hz	260 Hz	370 Hz	377 Hz
8 N		354		270
12 N		261		287
16 N	290		411	
20 N	295		472	

Recall from Figure G1 the small spike that occurred for the 20 N load case with the shaft at room temperature. Figure G4 shows the dynamic load amplitude versus excitation frequency behavior at $T_S = 188°C$. As can be seen, the problem of controlling the dynamic load amplitude near either resonance frequency is magnified with increasing shaft temperature. The DAQ system is not capable of automatically saving the data within this "resonance band" of excitation frequencies (from 230 Hz to 380 Hz). Thus, the data is subject to arbitrary manual saves by the operator. During testing for the 16 N load case, for example, the dynamic load magnitude reaches over 42 N (~ 9.4 lbs) at 308 Hz and as low as 8 N (1.8 lbs) within this unstable resonance band. Similar system behavior as that shown in Figure G4 occurs for all testing above ambient conditions.
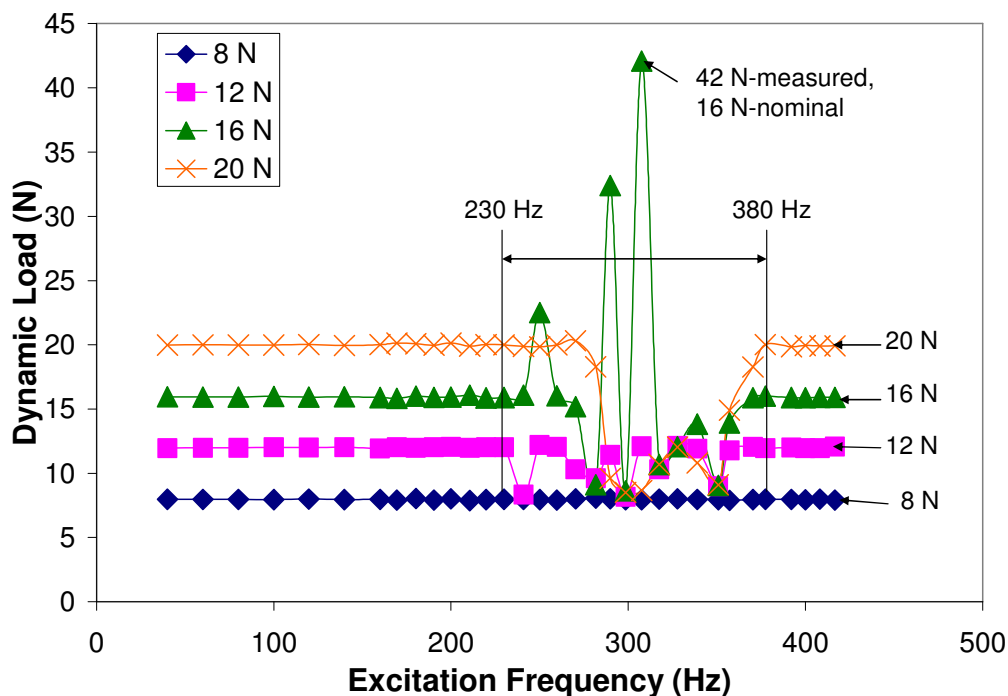

Figure G4 Amplitude of dynamic load versus excitation frequency (up to 420 Hz) with $T_S = 188°C$ showing erratic load behavior.

Figure G5 shows the waterfall plot of the 20 N load cell signals with the test shaft at 188°C. The figure indicates the detection of odd harmonic (3X, 5X, 7X, etc.)

vibration components of the fundamental (1X) excitation frequency. The peak amplitudes for the 5X and 7X components are larger than those of the 3X component. Further, for certain frequencies (between 260 Hz and 400 Hz) the response amplitudes within the 5X and 7X components are of equal magnitude as the 1X component. The detected components result from the vibration of the test shaft against the foil structure of the FB. The presence of odd harmonics of the fundamental frequency is characteristic of a system with friction; i.e., a system where a friction force acts in the direction opposite periodic motion.
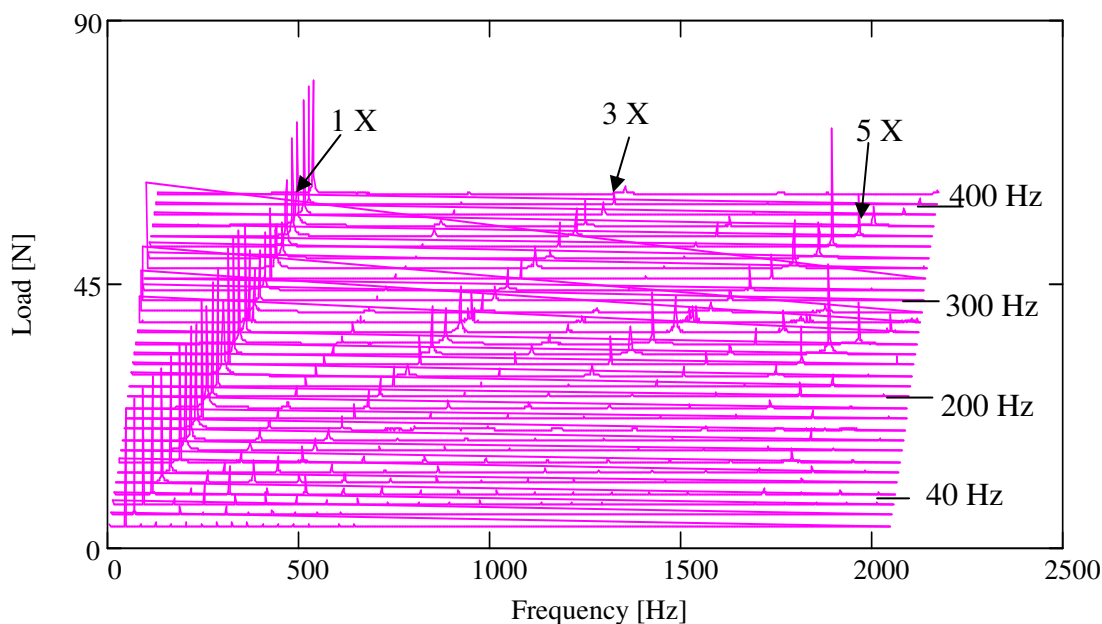

Figure G5 Waterfall plot of dynamic load cell signal showing 3X vibration component for excitation frequency 40 Hz to 420 Hz (T_S = 188 °C and F_O = 20 N).

Figure G6 shows the corresponding FB acceleration versus excitation frequency at T_S = 188°C for the erratic dynamic loads presented in Figure G4. Accelerometer signals within the resonance band are nearly as erratic as the dynamic loading. The FB mass response peak is evident at 250 Hz for the first three loads, but it does not appear clearly for the 20 N load case. The shaft and fixture response peak seems to shift closer towards 355 Hz for the 8N and 12 N load cases and 370 Hz for the 16 N and 20 N load cases, respectively.

Figure G7 shows the resulting C_{eq} for tests at $T_S = 188°C$. The FB does not seem to evidence null damping at either of the system resonant frequencies for all shaft temperature conditions. Table G4 summarizes the resulting C_{eq} values for the $T_S = 188°C$ at the room temperature resonant frequencies.
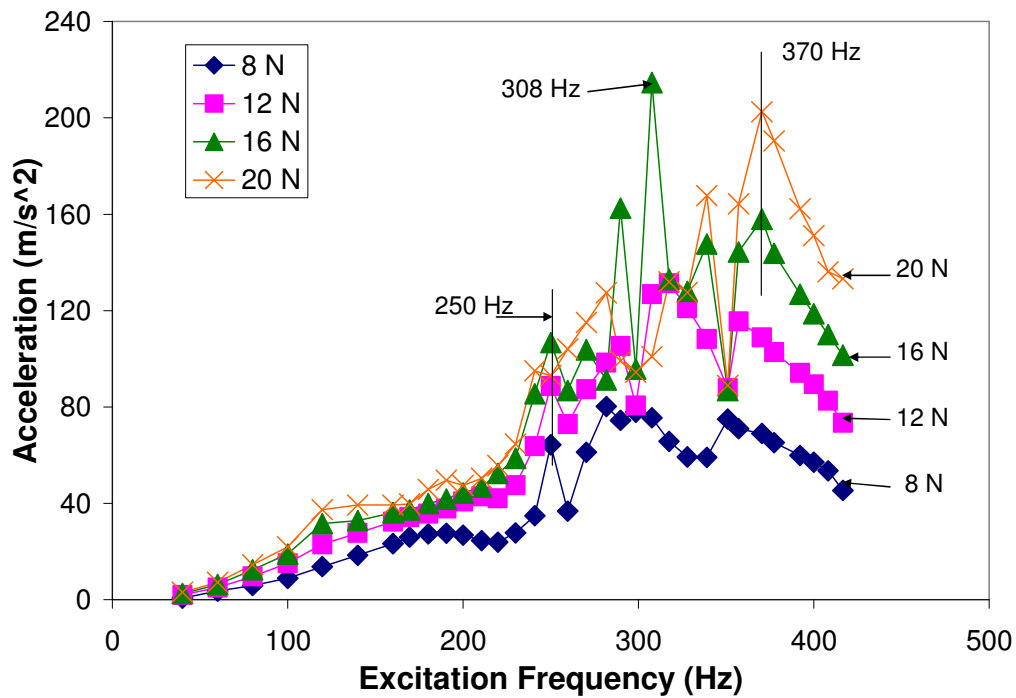

Figure G6 Amplitude of FB acceleration versus excitation frequency (up to 420 Hz) with T$_S$ = 188°C showing the FB response to erratic load behavior within resonance band.
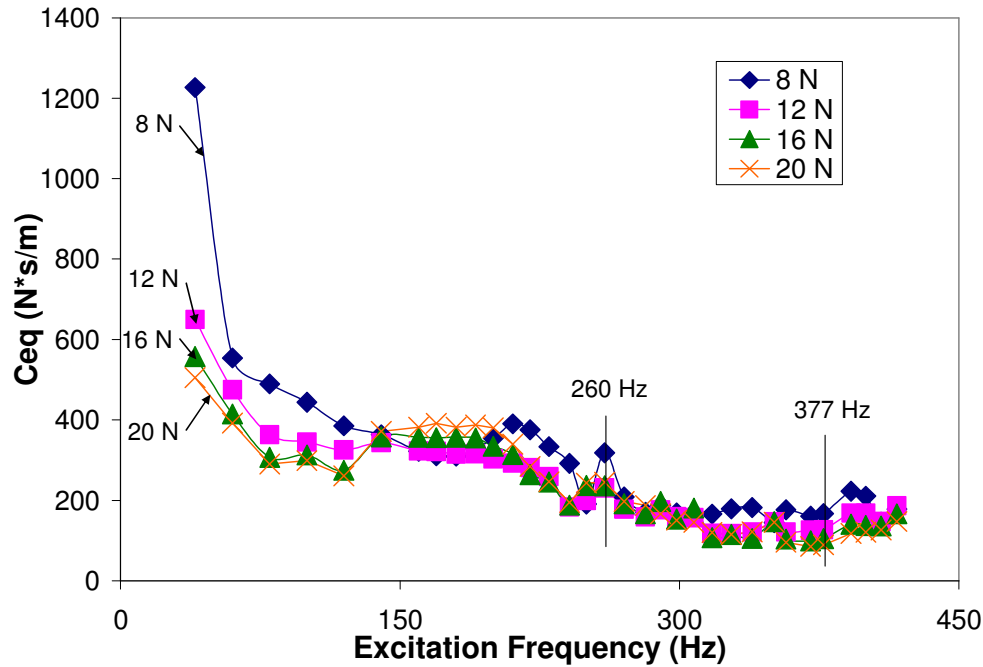
Figure G7 Equivalent viscous damping versus excitation frequency (up to 420 Hz) showing damping values at resonance with T_S = 188°C (ambient).

Table G4 Equivalent viscous damping evidenced at approximate resonance (at T_S = 188°C)

	C_{eq} (Ns/m) at Resonant Frequency			
Dynamic Load	240 Hz	260 Hz	370 Hz	377 Hz
8 N		318		167
12 N		231		127
16 N	237		99	
20 N	243		85	

The results show that the response of the bearing (with sufficient input force amplitude and shaft temperature) becomes uncontrollable at excitation frequencies above 230 Hz. Ultimately, the data presented within this appendix shows that it is not possible to detect clear trends from data within the resonance band of the test setup, between 230 Hz and 380 Hz. Therefore, testing and analysis in this thesis is restricted to frequencies below this resonance band ($\leq$ 200 Hz). Any analysis above this frequency is unrepeatable due to the randomness of saving the data manually.

APPENDIX H

EXPERIMENTALLY DERIVED DRY FRICTION COEFFICIENT

DATA COMPILED FOR CALCULATION OF AVERAGE AND

ERROR FOR 22.2 N AND 31.1 N AMPLITUDE LOADS

Table H 1 Average and standard deviation calculation for dry friction coefficient (μ_f) over test frequency range for all T_S (F_O=22.2 N)

Excitation Frequency (Hz)	Dry Friction Coefficient, μ_f				
	22°C	77°C	132°C	188°C	
40	0.387	0.381	0.323	0.321	
60	0.424	0.418	0.367	0.364	
80	0.424	0.422	0.390	0.377	
100	0.441	0.448	0.403	0.392	
120	0.417	0.434	0.384	0.380	
140	0.466	0.476	0.439	0.455	
160	0.457	0.476	0.456	0.455	
180	0.462	0.470	0.443	0.444	Average μ_f over the
200	0.496	0.476	0.429	0.440	T_S Range
Average μ_f	0.44	0.44	0.40	0.40	0.42
Standard Deviation	0.032	0.034	0.043	0.047	0.023
Percent Error	7.3%	7.5%	10.6%	11.8%	5.4%

Table H 2 Average and standard deviation calculation for dry friction coefficient over test frequency range for all T_S (F_O=31.1 N)

Excitation Frequency (Hz)	Dry Friction Coefficient, μ_f				
	22°C	77°C	132°C	188°C	
40	0.321	0.326	0.276	0.264	
60	0.342	0.346	0.311	0.306	
80	0.341	0.346	0.314	0.309	
100	0.353	0.378	0.346	0.345	
120	0.356	0.368	0.337	0.330	
140	0.412	0.428	0.396	0.411	
160	0.390	0.414	0.402	0.407	
180	0.396	0.394	0.393	0.403	Average μ_f over the
200	0.423	0.418	0.388	0.382	T_S Range
Average μ_f	0.37	0.38	0.35	0.35	0.36
Standard Deviation	0.036	0.036	0.046	0.053	0.014
Percent Error	9.6%	9.5%	13.0%	15.0%	4.0%

VITA

Name:	Anthony Wayne Breedlove
Address:	Department of Mechanical Engineering, 3123 TAMU, College Station, TX 77843, USA
Email:	<u>awbreed@hotmail.com</u>
Education:	B.A., Mathematics, University of Saint Thomas, Houston, TX, 2000 B.S., Mechanical Engineering, Texas A&M University, College Station, TX, 2004 M.S., Mechanical Engineering, Texas A&M University, College Station, TX, 2007
Permanent Address:	1715 East Archer Rd #2 Baytown, TX 77521, USA